Spatio-temporal Characterization of Geothermal Fields by Inverse Modeling

by

Elena C. Reinisch

A dissertation submitted in partial fulfillment of

the requirements for the degree of

Doctor of Philosophy

(Geoscience)

at the

UNIVERSITY OF WISCONSIN-MADISON

2019

Date of final oral examination: 05/08/2019

The dissertation is approved by the following members of the Final Oral Committee:

Kurt L. Feigl, Professor, Geoscience
Michael Cardiff, Associate Professor, Geoscience
Clifford H. Thurber, Vilas Distinguished Professor, Geoscience
Dante Fratta, Associate Professor, Geological Engineering
Christelle Wauthier, Assistant Professor, Department of Geosciences - Institute for CyberScience, Pennsylvania State University

Acknowledgements

I would first like to thank my advisor, Kurt Feigl, without whom this research would not have been possible. You have taught me so many invaluable lessons over these past five years, all of which I am grateful for. I would especially like to thank you for helping me develop my scientific intuition. Thank you also for not only teaching me how to be successful as a scientist but also the responsibilities we have as researchers. You have always believed in my capabilities, even when I doubted myself. I am honored to have been a student of yours. Thank you!

I would also like to thank my other committee members for their continued guidance throughout my graduate studies. Mike and Cliff, your inverse theory class inspired much of the work in this dissertation. Also, thank you, Mike, for deepening my understanding of statistical analysis. Dante, thank you for challenging me to think of my research in new and creative ways. Christelle, thank you for your willingness to serve as a mentor and committee member and for sharing your advice and expertise with me despite such short notice. I look forward to many insightful discussions in the future!

I am grateful to the Graduate School and the Department of Geoscience for all of the opportunities they have given me as a graduate student. I am especially grateful to have been a member of the PoroTomo team. This project gave me the experience of working and learning from members of various fields and institutions and taught me how to collaborate amongst a large team.

Navigating graduate studies and research would not have been possible without the advice and help of my office mates along the way, Hélène le Mével, Tabrez Ali, and Sam Batzli, and all of my colleagues at Weeks. Special thanks to Jeremy Patterson, Beatriz Cosenza, Federica Lanza, and of course Lesley Parker for being such amazing, supportive friends! I am also grateful to all of my friends outside of graduate studies who have made Madison feel like home, and to my long-time friends Shiragi Patel and Jacob Jewulski for their continued support over the years.

I would not have made it this far without the love and support that my family has given me as well. Thank you to my dad for sharing his love of science with me throughout my childhood (all of those school science fair experiments paid off!). Thank you to my mom for her continued encouragement and for teaching me that my aspirations, even in the face of adversity, are achievable through hard work and determination. Thank you to my sister, Anamaria, for always being an amazing role model and someone I can still go to for advice. I would also like to thank my grandparents, my parents-in-law Monica and Bryan Reinisch, and my Aunts Toni and Shari. Your encouragement and support over the years have meant the world to me and have kept me going through difficult times.

I am especially grateful to my husband, Alex, who has been instrumental to my success in graduate studies. Our discussions over my research have sparked some of the most creative ideas I have had throughout these five years. Thank you for putting up with all of the sleepless nights I spent finishing research and the times when I had to work instead of socialize. You have been there through all of the highs and lows of graduate school and were always by my side to lend a hand, selflessly putting me and my schooling above all else. I am truly blessed to have such a supportive husband as you.

Last but not least, I would like to thank Mrs. Winnie Baum for being an incredible eighth grade math teacher and role model. You showed me what it means to be a strong, successful woman in the STEM field and inspired a love of algebra that still drives my work today. I will be forever grateful that I was on Team 8-2 of Fort Zumwalt South Middle School!

Contents

Chapter Publication Status

1. Characterizing Volumetric Strain at Brady Hot Springs, Nevada, USA Using Geodetic Data, Numerical Models, and Prior Information

    - coauthors: Michael Cardiff and Kurt L. Feigl
    - status: published on August 23, 2018
    - journal: *Geophysical Journal International*

2. Time-series Analysis of Volume Change at Brady Hot Springs, Nevada, USA Using Geodetic Data from 2004 - 2018

    - coauthors: Michael Cardiff, Corné Kreemer, John Akerley, and Kurt L. Feigl
    - status: submitted on April 15, 2019
    - journal: *Journal of Geophysical Research - Solid Earth*

3. Geodetic Measurements and Numerical Models of Deformation at Coso Geothermal Field, California, USA, 2004 - 2016

    - coauthors: S. Tabrez Ali, Michael Cardiff, J. Ole Kaven, and Kurt L. Feigl
    - status: to be submitted in Fall 2019
    - journal: *Remote Sensing of Environment*

4. Spatio-temporal Analysis of Deformation at San Emidio Geothermal Field, Nevada, USA Between 1992 and 2010

    - suggested coauthors: Michael Cardiff, Mariana Eneva, John Akerley, Ian Warren, and Kurt L. Feigl
    - status: submitted on June 28, 2019
    - journal: *Remote Sensing*, special issue “InSAR for Earth Observation”

ABSTRACT

Interferometric synthetic aperture radar (InSAR) is a powerful geodetic technique capable of measuring deformation at fine resolution. Radar data's two-dimensional structure along with the pair-wise nature of interferometry allow InSAR to capture both the spatial and temporal extent of deformation. This dissertation focuses on improving spatio-temporal modeling techniques for InSAR data to better describe the observed subsidence at several geothermal fields in the Western U.S. The first chapter focuses on refining the spatial analysis of deformation observed at Brady Hot Springs, Nevada by introducing a parameterization which directly relates displacement at the Earth's surface to subsurface reservoir volume change. Geostatistical inversion in a Bayesian framework identifies thermal contraction of the rock matrix as the dominant driving mechanism of the observed subsidence. The second chapter extends this modeling to multiple interferometric pairs to explore the deformation's temporal nature. Joint time-series analysis of volume change rates estimated from InSAR and Global Positioning System (GPS) data determines the dependence of deformation on well operations. The third chapter measures transient deformation at Coso geothermal field, California using InSAR and GPS data acquired between 2004 and 2016 to quantify relationships between deformation, pumping, and seismicity. Changes in subsidence rate, reservoir contraction, and estimated sink depth after 2010 found from spatial and temporal deformation modeling are attributed to changes in injection protocol corresponding to sustainability efforts implemented in late 2009. The last chapter quantifies the spatio-temporal dependence of the subsiding region at San Emidio geothermal field, Nevada by modeling InSAR data from 1992 to 2010.

Introduction

Geothermal power production is a sustainable process by which the hot fluid in subsurface reservoirs is utilized to produce electricity. This fluid, which is heated naturally by a geothermal gradient or magma body, is extracted by a geothermal power plant via production wells. Steam from the produced fluids is used to drive turbines at the plant and produce electricity. The cooled fluid is then reinjected at shallow depths and travels via faults and fractures back down to the heated reservoir. Geothermal fields are an excellent example of a rheological experiment because impulses are known (i.e., the amount of fluid injected and produced) and can be altered to measure subsequent responses (e.g., seismicity, deformation).

This dissertation focuses on measuring deformation at geothermal fields using a geodetic monitoring technique named interferometric synthetic aperture radar (InSAR). InSAR is a powerful geodetic technique capable of detecting deformation with uncertainty on the order of millimeters to centimeters. Radar data's two-dimensional structure along with the pair-wise nature of interferometry allow InSAR to capture both the spatial pattern and temporal extent of deformation. The goal of this dissertation is to improve spatio-temporal modeling techniques for InSAR data to better characterize observed subsidence at several geothermal fields in the Western U.S. This goal is accomplished by:

- testing hypotheses for geophysical mechanisms driving subsidence
- identifying subsurface processes, and
- quantifying relationships between deformation and well operations.

These techniques are applied to three geothermal sites in the Western U.S.:

- Brady Hot Springs geothermal field, Nevada, USA (Chapters 1 and 2)
- Coso geothermal field, California, USA (Chapter 3), and
- San Emidio geothermal field, Nevada, USA (Chapter 4).

1 Characterizing Volumetric Strain at Brady Hot Springs, Nevada, USA Using Geodetic Data, Numerical Models, and Prior Information

---

Published as: Elena C Reinisch, Michael Cardiff, Kurt L Feigl, Characterizing volumetric strain at Brady Hot Springs, Nevada, USA using geodetic data, numerical models and prior information, *Geophysical Journal International*, Volume 215, Issue 2, November 2018, Pages 1501–1513, https://doi.org/10.1093/gji/ggy347.

Abstract

The geothermal field at Brady Hot Springs, Nevada has subsided over the past decade. Between 2004 and 2014, the rate of downward vertical displacement was on the order of 10 millimeters per year, as measured by two independent geodetic techniques: Interferometric synthetic aperture radar (InSAR) and Global Positioning System (GPS). The observed deformation field forms an approximately elliptical bowl that is 4 kilometers long and aligned with the trace of the NNE striking normal fault system. We use modeling to estimate the plausibility of pressure changes or thermal contraction as the cause of the observed subsidence. As a result, Bayesian inference favors with "very strong evidence" thermal contraction over other hypotheses as the dominant driving mechanism for the observed subsidence. Using InSAR data spanning from 22 July 2016 and 22 August 2017, we estimate the volume change rate in the significantly deforming volume to be (-29 +/- 3) thousand cubic meters per year and the total rate of change in thermal energy between -53 and -79 Megawatt. We infer the total volume of cubes where the estimated volumetric strain rate is significantly different from zero with 95 percent confidence to be 119 million cubic meters. We find that the main region of significant cooling occurs between the injection and production well locations. This result supports the idea that highly permeable conduits along faults channel fluids from shallow aquifers to the deep reservoir

tapped by the production wells.

1.1 Introduction

The geothermal field at Brady Hot Springs is situated in the Great Basin region of the northern Basin and Range Province, near the western boundary of the North American tectonic plate. There, numerous northeast-striking faults accommodate a combination of mostly extensional motion with some dextral shear, as inferred from studies of geodetic and neotectonic observations (e.g. Minster & Jordan, 1987) and other observations, as recently reviewed by Pérouse & Wernicke (2017). Located ~ 80 km northeast of Reno, Nevada, the study area lies in a basin between the Truckee Range and Northern Hot Springs Mountains and is aligned with one of the three major, NNE-striking normal fault systems comprising the Great Basin region (Benoit et al., 1982; Faulds et al., 2010b; Jolie et al., 2015). This major fault dips WNW (Faulds et al., 2003, 2010a; Jolie et al., 2015; Siler et al., 2016). Although fault scarps are visible, none of them is associated with the minor seismic events that have been recorded in the area. Since the installation of a monitoring network in 2010, the largest earthquake to occur within a 10-km radius of Brady had a (local) magnitude of 2.2 (Nathwani et al., 2011; Foxall, 2014, 2016; Cardiff et al., 2017).

At Brady Hot Springs, the fault trace steps left in a bend approximately 4 km in length. There, the geothermal system comprises fumaroles, sinter, warm ground, and mud pots, which collectively reflect hydrothermal activity (Faulds et al., 2010b). Between 1841 and 1861, the site was a stopping point on the historic California Trail (BLM, 2014):

> To pioneers on the Truckee River branch of the California Trail, Brady's Hot Springs, then known as Tenderfoot Station, were always a blessing and occasionally a curse. The springs were located near the middle of the dreaded Forty-Mile Desert and the water was potable when cooled. However, thirst-crazed oxen were commonly scalded when they rushed into the boiling water. (Benoit et al., 1982)

The fractures associated with the mature fault system dominate the distribution and flow of hydrothermal fluids at Brady Hot Springs (e.g. Laboso & Davatzes, 2016). These fluids are extracted to produce electricity at a geothermal power plant that was constructed in 1991 and has been operating since 1992 (Ettinger & Brugman, 1992). The production wells are situated in the SSW portion of the geothermal field, where they extract hot brine at depths between 400 and 1770 meters from a steeply-plunging projection of a left step in the Brady fault zone (Faulds et al., 2010b; Davatzes et al., 2013; Jolie et al., 2015). Located NNE of the production wells are the injection wells with depths of roughly 200 meters. The operators of the geothermal plant have reported high transmissivity that has been attributed to fluids flowing through faults (Faulds et al., 2010b). Numerous faults cut through the geothermal resource, as inferred from detailed, three-dimensional models based on drilling records, field observations, seismic profiling and gravimetric measurements (Jolie et al., 2015; Siler et al., 2016; Witter et al., 2016).

These geologic structures also appear to control the deformation field observed by satellite geodesy. As shown in Fig. 1.1, the spatial distribution of subsidence forms an approximately elliptical bowl that is 4 km long and aligned with the trace of the normal fault system that strikes NNE (Ali et al., 2016a). The deformation field can be described by models of "sinks" that decrease in volume. The rate of downward vertical displacement was on the order of 10 mm $\cdot$ yr^{-1}, as measured by interferometric synthetic aperture radar (InSAR) data acquired between 2004 and 2014 (Ali et al., 2016a).

Here, we consider the spatial variations in the deformation field between July 2016 and August 2017. The maximum rate of range change is 34 mm $\cdot$ yr^{-1} (Fig. 1.1b). If we neglect horizontal motion, then the rate of (downward) vertical displacement estimated from InSAR is similar to that estimated from the Global Positioning System (GPS) for a station (BRD1) located at Brady with respect to a station (BRDY) located some 5 km to the SW, outside the geothermal field (Fig. 1.1).

Looking at the observed deformation field in Fig. 1.1, one notes that the fastest rate of deformation occurs at a distance of more than 1 km (along strike) from the nearest injection well and more than 1 km from the nearest production well. We infer that the faults act as highly permeable conduits to channel fluids from shallow aquifers (fed by the injection wells) to the deep geothermal reservoir (tapped by the production wells), as suggested by Ali et al. (2016a).

How does such flow cause the observed subsidence? To answer this question, we consider two possible mechanisms: (1) decreasing pore-fluid pressure and (2) thermal contraction. Either mechanism could occur as hot fluids are extracted from the production wells at the southwest end of the field, cooled in the heat-exchanger at the power plant and then injected at the northeast end of the field. Under the first mechanism, a decrease in pore fluid pressure shrinks the pores. Under the second mechanism, the decrease in temperature contracts the rock.

1.2 Data

1.2.1 InSAR

We use synthetic aperture radar data acquired with a wavelength of approximately 30 mm by the TerraSAR-X satellite mission operated by the German Space Agency, DLR (Pitz & Miller, 2010). We work with a pair from track 53 spanning July 22, 2016 to August 22, 2017 (Fig. 1.1). This pair spans 396 days and has an orbital separation of -89 m. We produce the interferograms using GMTSAR, which utilizes Generic Mapping Tools (GMT) to create and visualize interferometric pairs (Sandwell et al., 2011a,b). We remove noise by applying an adaptive Goldstein filter that depends on spatial coherence (Goldstein & Werner, 1997; Baran et al., 2003; Sandwell et al., 2011b). Unwrapping is performed using the "statistical-cost, network-flow phase-unwrapping algorithm" (Snaphu) (Chen & Zebker, 2000). This interferogram is available publicly (Reinisch & Feigl, 2018).

The data set includes values of range change $\Delta\rho$ [mm] over an area of 3.5 km by 4.5 km.

Range change is related to the displacement vector $\mathbf{u}$ in the direction of the satellite by

$$\boldsymbol{\Delta\rho} = -\hat{\mathbf{s}} \cdot \mathbf{u} \tag{1.1}$$

where $\hat{\mathbf{s}}$ is the unit vector pointing from a pixel on the ground to the sensor aboard the satellite with components (x), (y), and (z) corresponding to the eastward, northward, and upward directions, respectively (Massonnet & Feigl, 1998). For our dataset, $\hat{\mathbf{s}} = [-0.55, 0.10, -0.82]$. Note that increasing range change corresponds to motion away from the sensor onboard the satellite, thus subsidence. In other words, range change is the negative of the "line of sight" (LOS) displacement used elsewhere (e.g., Zebker & Goldstein, 1986). We convert values of range change $\Delta\rho$ to range change rates $\dot{\boldsymbol{\rho}}$ by dividing by the 396-day time interval $\Delta t = 1.0842$ years. The far-field effects are removed by averaging the observed data in the NW portion of the interferogram, where we expect no deformation, and subtracting the result from all the observed range change rates. There are two regions where phase discontinuities are known to occur in interferograms at Brady Hot Springs. These discontinuities have not been unwrapped accurately, so we exclude them from the analysis.

1.2.2 GPS

We also analyze data from two GPS stations in the MAGNET network whose time series of relative position are available publicly (Kreemer, 2018). These data have been analyzed using standard procedures (Blewitt et al., 2013). GPS station BRD1 was installed within the subsiding bowl on March 10, 2016 as part of the PoroTomo project (Feigl & PoroTomo Team, 2017a). We use GPS measurements of displacement at BRD1 with respect to BRDY converted to range change estimates to validate the range change found from InSAR. We use BRDY to estimate the far-field range change for the GPS measurements. From the interferogram, we select a subregion of pixels nearest to the location of BRD1 for comparison. For an estimate of far-field deformation corresponding to BRDY, we select a region southeast of the subsiding

bowl where little deformation is observed, take the mean range change, and subtract it from the range change of the selected pixels at BRD1.

1.2.3 Accuracy

We use GPS to analyze the accuracy of the InSAR measurements. We difference the corresponding GPS daily estimates of position in time and then compute the scalar product with the unit pointing vector of the satellite using equation (1.1). The uncertainty for the range change estimated from GPS is derived from measurement uncertainty at each station. We use the standard error of the mean as an estimate of uncertainty for the range changes observed using InSAR. We find the difference between the mean range change from InSAR and the range change measured from GPS to be 3.58 mm (Table 1.1). We calculate a standard deviation of 4.37 mm using the established relation for the variance of the difference of two random variables (e.g., Wackerly et al., 2007). The maximum difference was 3.60 mm. This suggests that the realistic 1σ uncertainty is less than 5 mm in range change for the InSAR data set.

1.2.4 Data error covariance

We define a spatial covariance function for the InSAR data using semivariogram analysis with an exponential model (e.g. Hohn, 1998, p. 28). We sampled a subregion in the NNW corner of the study area, which is known to contain little to no deformation. We use an exponential model to describe the semivariogram

$$\gamma(h) = c\left(1 - \exp\left(-3\frac{h}{a}\right)\right) \tag{1.2}$$

where h is the distance between two pixels, c is the threshold value at which $\gamma(h)$ levels off, and a is the characteristic distance, or the value of h where this leveling first occurs (e.g., Hohn, 1998). Using the exponential portion of equation (1.2) to define the spatial correlation between

observations, we arrive at a data covariance function of

$$R(h) = \sigma^2_{GPS} \exp\left(-3\frac{h}{a}\right) \tag{1.3}$$

where the characteristic distance $a = 230$ m and σ^2_{GPS} is a factor corresponding to the uncertainty in InSAR measurements derived from comparison to GPS.

1.3 Methods

To describe the deformation field observed by InSAR, we perform inverse modeling. We have implemented a nonlinear inversion approach (Feigl & Thurber, 2009) in an open-source software package called the General Inversion of Phase Technique (GIPhT). Given a deformation model with initial estimates and bounds for its parameters, GIPhT uses simulated annealing to invert on the grid of pixels comprising each interferogram. The resulting output is a refined estimate of the model parameters. We also adopt a methodology that allows us to perform linear inverse modeling with governing equations in terms of volume change rates. As opposed to the nonlinear approach, which solves a physically informed but sparsely parameterized inverse problem, the new methodology introduces a more highly parameterized inversion by applying a gridded formation to the data and modeling the deformation within each cube. This formulation is advantageous in that it allows for a direct physical interpretation related to the geophysical processes at Brady Hot Springs.

1.3.1 Parameterization Using Nonlinear Inversion

To simulate the deformation field observed by InSAR and GPS using nonlinear inversion, we extend previous studies using a parameterization in terms of dislocations embedded in a homogeneous half space with uniform elastic properties (Okada, 1985). In this formulation, the vector displacement at the ground surface depends only on a single material property such that

the leading coefficient is:

$$\frac{\lambda}{\lambda + \mu} = 2\nu \tag{1.4}$$

where λ and μ are Lamé's constants and ν is Poisson's ratio (e.g. Stein & Wysession, 2003). The formulation from Okada (1985) assumes that the value of this coefficient is spatially uniform in an isotropic, linearly elastic half-space. In addition, we assume that it is also constant in time. Following Ali et al. (2016a), we assume the value of Poisson's ratio $\nu = \frac{1}{4}$.

A previous study (Ali et al., 2016a) parameterized the contracting shallow reservoir in terms of four Okada (1985) dislocations, each described by nine parameters, including three positional coordinates (easting, northing, and elevation), two dimensions (length and width) of the rectangular slip patches, two angles (strike and dip), and three components of the slip vector. The slip vector quantifies the relative displacement of one side of the patch with respect to the other. The three components of the slip vector are: dip-slip U_1 and strike-slip U_2 in the plane of the patch and tensile opening U_3 normal to it. The previous study (Ali et al., 2016a) allowed dip-slip U_1 and strike-slip U_2 to vary as model parameters to be estimated in the inversion. At Brady, we expect negative values of opening $U_3 < 0$, representing the tensile closing of "sinks" in the shallow aquifers.

1.3.2 Parameterization Using Linear Inversion

Although the previous parameterization of four Okada sinks (Ali et al., 2016a) fits the InSAR data well, it does not have a straightforward interpretation in terms of the fluids flowing in the geothermal system at Brady. To address this issue, we define a "multi-cube" parameterization to include many cubic sinks which comprise a single grid layer at a given depth. In this model of the subsurface aquifer, each cube represents a volume element with sides of length $W = 100$ m. Each such cube is divided into eight smaller cubes by three square, planar surfaces ("patches"), each with surface area A, that intersect orthogonally at their centroid, as sketched in Fig. 1.2. Each square patch defines a dislocation with slip vector $\mathbf{U} = [0, 0, -U_3]$ as

defined by Okada (1985), described by Segall (2010), and implemented in Matlab by Beauducel (2014). In other words, each square patch experiences uniform contraction in the plane-normal direction where $\Delta V < 0$ corresponds to contraction in our notation. Thus, one cube has an initial volume of $V_0 = W^3$, a volume change of $\Delta V = -3W^2U_3$, and a volumetric strain of $\epsilon_V = -3U_3/W$. Where our nonlinear approach assigned 4 sinks in total, this "multi-cube" parameterization characterizes volume change within each cubic element of the grid.

This "cubic" parameterization simulates a surface displacement field which is numerically equivalent to the one simulated by the formulation of Mogi (Mogi, 1958), after scaling by a factor of $9/5$. This equivalence has been mentioned in the literature (Aki & Richards, 1980) and derived analytically (Bonafede & Ferrari, 2009).

To validate our numerical implementation of the multi-cube model, we consider a single cube with side width $W = 100$ m, volume change $\Delta V_{multi} = -60$ m^3, and centroid depth of $d = 100$ m. We compare the resulting displacement field to that calculated analytically from the "Mogi" solution presented in equation (7.14) of Segall (2010) with a volume change of $\Delta V_{Mogi} = -33$ m^3. The root-mean-square (RMS) difference of the resulting displacement vectors is less than 60 μm in each of the three components (eastward, northward, and upward).

We also compare the resulting displacement field of the multi-cube model to the analytical half-space solution for displacement caused by a single force at a point, given traction-free boundary conditions, as described by Mindlin & Cheng (1950) and reprinted as Equation 4.39 in Wang (2000). Again comparing to the multi-cube parameterization, we find the root-mean-square (RMS) difference of resulting displacement vectors is less than 40 μm in each of the three components (eastward, northward, and upward).

Lastly, we compare the resulting displacement field of the multi-cube model to the half-space solution for surface deformation due to an internal volume strain introduced by Okada (1992) and restated by Mossop & Segall (1999), their Equation 1. We find the root-mean-square (RMS) difference of resulting displacement vectors is less than 30 μm in each of the

three components (eastward, northward, and upward).

Adopting the multi-cube model allows us to interpret volumetric strain in terms of two conceptual models: a decrease in pore fluid pressure and thermal contraction. For simplicity, we assume:

1. The medium is a purely elastic solid.

2. The Poisson ratio $\nu = 1/4$ throughout the modeled medium.

3. The compressibility of the fluid is negligible.

Interpreting the volume change rate in terms of a rate of change in pore fluid pressure $\dot{P}$ leads to the relationship:

$$\dot{V}^{(P)} = \left(\frac{1}{H}\dot{P}\right) V_0 \tag{1.5}$$

where $1/H$ [Pa^{-1}] is the poroelastic expansion coefficient (Wang, 2000). Since the initial volume is constant, we interpret the term in parentheses as a poroelastic volumetric strain rate

$$\dot{\epsilon}^{(P)} = \frac{1}{H}\dot{P}. \tag{1.6}$$

Alternatively, we can interpret the same volume change rate in terms of thermal contraction, leading to the relationship:

$$\dot{V}^{(T)} = (\alpha_T \dot{T}) V_0 \tag{1.7}$$

where α_T is the thermal expansion coefficient and $\dot{T}$ is the rate of temperature change (Wang, 2000). Since the initial volume is constant, we can interpret the first term as a thermal volumetric strain rate

$$\dot{\epsilon}^{(T)} = \alpha_T \dot{T}. \tag{1.8}$$

We may also interpret the modeled volume change rate in terms of a linear combination of

these two conceptual models:

$$\dot{V}^{(P+T)} = \left(\frac{1}{H}\dot{P}\right) V_0 + (\alpha_T \dot{T}) V_0 \tag{1.9}$$

In this case, estimated volumetric strain rates contain contributions from thermal contraction and a decrease in pore fluid pressure

$$\dot{\epsilon}^{(P+T)} = \frac{1}{H}\dot{P} + \alpha_T \dot{T}. \tag{1.10}$$

1.3.3 Nonlinear Inversion Modeling with GIPhT

We improve our inverse modeling by using nonlinear inversion by introducing a sequential inversion process, which allows us to use both unwrapped range change and wrapped phase change observables (Reinisch et al., 2016). Starting with an initial set of estimates for parameters of a deformation model with loose bounds on their uncertainties, we use the estimates from this inversion using unwrapped range change observables as prior information for a second inversion using wrapped phase change observables. This 2-step inversion allows us to narrow the uncertainties on the resulting estimates of the model parameters.

We derive our initial estimate of the model parameters from the results of Ali et al. (2016a) using a combination of four sinks representing surface displacements from faults in a halfspace (i.e. Okada sources, Okada, 1985; Segall, 2010). After applying our sequential inversion method to the TSX track 53 pair spanning December 24, 2011 to October 27, 2012 shown in Ali et al. (2016a), we use the refined model parameter estimates as an initial set of estimates for the sequential inversion of our InSAR data set.

1.3.4 Linear Geostatistical Inversion

We write the modeled values of the range rates using the linear governing equations from the "multi-cube" parameterization

$$\dot{\boldsymbol{\rho}}^{(mod)} = \mathbf{Gm} \tag{1.11}$$

where $\dot{\boldsymbol{\rho}}^{(mod)}$ is a vector of modeled values of range change rate, $\mathbf{G}$ is the matrix representing the forward model, and $\mathbf{m}$ is a m-by-1 estimated vector of best-fitting parameters. Each element of $\mathbf{G}$ is represented by

$$G_{i,j} = u_{i,j}^{(x)}\hat{s}^{(x)} + u_{i,j}^{(y)}\hat{s}^{(y)} + u_{i,j}^{(z)}\hat{s}^{(z)} \tag{1.12}$$

where $\mathbf{u}$ is a vector of component displacements from the cubic model for the j^{th} cube and the i^{th} observed range change rate $\dot{\rho}_i$. We again assume Poisson's ratio to be $\nu = 1/4$. We explain $\mathbf{m}$ by defining prior models for the variable components of $\dot{V}^{(P)}$, $\dot{V}^{(T)}$, and $\dot{V}^{(P+T)}$ using the model parameter covariance matrices specific to each model's *a priori* uncertainty. In order to incorporate prior information on $\dot{V}^{(P)}$, $\dot{V}^{(T)}$, and $\dot{V}^{(P+T)}$, we solve these equations in a Bayesian framework.

Interpreting the volume change rate in terms of thermal contraction (equation 1.7), we define the model parameters as thermal volumetric strain rates $m_i^{(T)} = \alpha_T \dot{T}_i$. From the literature, we find a suitable (68% confidence) range for $\alpha_T \in (3.5 \pm 1.5) \times 10^{-5}$ K^{-1} (e.g. Cooper & Simmons, 1977; Roy et al., 1989; Rutqvist et al., 2002). We define a 68% confidence range for $\dot{T} \in (-1.2 \pm 0.6)$ K $\cdot$ yr^{-1} based on balancing of thermal energy in the system with fluid flow (e.g., Temple University, 2017; University of Wisconsin, 2016). Assuming that each of these random variables is drawn from a Gaussian distribution, we calculate the resulting 68% confidence range of the product to be

$$\alpha_T \dot{T} \in (-42 \pm 29) \text{ [microstrain} \cdot \text{yr}^{-1}] \tag{1.13}$$

using definitions for the mean and standard deviation of the product of two Gaussian random variables (e.g., Wackerly et al., 2007).

Alternatively, we interpret the modeled volume change rate in terms of a decrease in pore fluid pressure (Equation 1.5) and our model parameters as poroelastic volumetric strain rates $m_i^{(P)} = \frac{1}{H}\dot{P}_i$. From the literature, we find a suitable (68% confidence) range for $\frac{1}{H} \in (2.8 \pm 0.4) \times 10^{-10}$ Pa^{-1} (e.g., Nur & Byerlee, 1971; Wang, 2000; Ingraham et al., 2017). We define a 68% confidence range for $\dot{P} \in (-0.3 \pm 0.2) \times 10^5$ Pa $\cdot$ yr^{-1} based on the rate of pressure decrease corresponding to a $\sim$100-meter change in groundwater level at Brady within the last thirty years and data from the site (e.g., Temple University, 2017; Ormat Techmologies Inc., 2017). We again assume Gaussian distributions for the variables and calculate the resulting 68% confidence range of the product to be

$$\frac{1}{H}\dot{P} \in (-9.2 \pm 4.8) \text{ [microstrain} \cdot \text{yr}^{-1}]. \tag{1.14}$$

To interpret the modeled volume change rate in terms of both thermal contraction and a decrease in pore fluid pressure (Equation 1.9), we define a 68% confidence range for $\dot{\epsilon}^{(P+T)} = \frac{1}{H}\dot{P} + \alpha_T\dot{T}$. Using the prior models stated in Equations 1.13 and 1.14 as well as the standard equations for the linear combination of two Gaussian random variables (e.g., Wackerly et al., 2007), we find a 68% confidence range of

$$\frac{1}{H}\dot{P} + \alpha_T\dot{T} \in (-51 \pm 29) \text{ [microstrain} \cdot \text{yr}^{-1}]. \tag{1.15}$$

We represent these prior models using an exponential covariance structure function and characteristic distance scales to be $l_y = 1000$ m along the strike of the major fault (roughly 36° NE) and $l_x = 200$ m across its strike. We assume that the mean $\mu_{\mathbf{m}}$ of the parameters is

spatially uniform and define the posterior probability distribution according to Bayes' rule:

$$f_{\mathbf{m},\mu_\mathbf{m}|\dot{\boldsymbol{\rho}}}(\mathbf{m},\mu_\mathbf{m}) \sim f_{\dot{\boldsymbol{\rho}}|\mathbf{m},\mu_\mathbf{m}}(\dot{\boldsymbol{\rho}}) f_{\mathbf{m},\mu_\mathbf{m}}(\mathbf{m},\mu_\mathbf{m}). \tag{1.16}$$

The likelihood function equates to

$$f_{\dot{\boldsymbol{\rho}}|\mathbf{m},\mu}(\dot{\boldsymbol{\rho}}) = (2\pi)^{-n/2}|\mathbf{R}|^{-1/2} \cdot \exp\left(-\frac{1}{2}(\dot{\boldsymbol{\rho}} - \mathbf{G}\mathbf{m})^{\mathrm{T}}\mathbf{R}^{-1}(\dot{\boldsymbol{\rho}} - \mathbf{G}\mathbf{m})\right) \tag{1.17}$$

where the sample size $n = 159,597$ (Aster et al. 2013, p. 260; Gelman et al. 2013, p. 71). Similarly, the prior distribution equates to

$$f_{\mathbf{m},\mu_\mathbf{m}}(\mathbf{m},\mu_\mathbf{m}) = (2\pi)^{-m/2}|\mathbf{Q}|^{-1/2} \cdot \exp\left(-\frac{1}{2}(\mathbf{m} - \mathbf{L}\mu_\mathbf{m})^{\mathrm{T}}\mathbf{Q}^{-1}(\mathbf{m} - \mathbf{L}\mu_\mathbf{m})\right). \tag{1.18}$$

where $m = 1,656$ is the number of parameters (Aster et al. 2013, p. 260; Gelman et al. 2013, p. 71). Here $\mathbf{R}$ is the data covariance matrix defined by Equation 1.3, $\mathbf{L}$ is a vector of ones representing the stationary mean $\mu_\mathbf{m}$, and $\mathbf{Q}$ is the model covariance matrix defined as

$$Q_{i,j} = \sigma_\epsilon^2 \exp\left(-\left(\left(\frac{|x_i - x_j|}{l_x/3}\right)^2 + \left(\frac{|y_i - y_j|}{l_y/3}\right)^2\right)^{\frac{1}{2}}\right) \tag{1.19}$$

where σ_ϵ^2 is defined based on the choice of prior and (x_i, y_i) and (x_j, y_j) are the positions of the i^{th} and j^{th} model parameters. The mean of the parameters $\mu_\mathbf{m}$ is estimated and then compared to what we consider reasonable from our 68% confidence range in each of the prior models.

From Equations 1.16-1.18, we find the negative logarithm of the posterior probability distribution to be governed by

$$\frac{1}{2}(\dot{\boldsymbol{\rho}} - \mathbf{G}\mathbf{m})^{\mathrm{T}}\mathbf{R}^{-1}(\dot{\boldsymbol{\rho}} - \mathbf{G}\mathbf{m}) + \frac{1}{2}(\mathbf{m} - \mathbf{L}\mu_\mathbf{m})^{\mathrm{T}}\mathbf{Q}^{-1}(\mathbf{m} - \mathbf{L}\mu_\mathbf{m}). \tag{1.20}$$

Following Kitanidis (2007), we solve for best-fitting parameters by minimizing Equation 1.20

with respect to $\mathbf{m}$ and $\mu_{\mathbf{m}}$.

1.4 Results

1.4.1 Parameterization using Okada (1985) sources

We apply our 2-step nonlinear inversion scheme using GIPhT (Feigl & Thurber, 2009) to model the deformation field between 22 July 2016 and 22 August 2017 as measured by the InSAR data set described above and shown in Fig. 1.1. Our initial estimates of the parameters are derived from Ali et al. (2016a) (their Table 1) and comprised of four Okada (1985) sinks (i.e., 4-patch model). We also estimate contributions of far-field deformation, atmospheric effects, and orbital error (i.e., nuisance parameters) by considering a gradient with components in the eastward, northward, and upward directions (Feigl & Thurber, 2009). We find an estimate of far-field deformation $\Delta\rho_0 = (4.4 \pm 1.9)$ mm and components of phase gradient $\delta\phi/\delta x = (7.2 \pm 2.6) \times 10^{-7}$, $\delta\phi/\delta y = (0.08 \pm 1.8) \times 10^{-7}$, and $\delta\phi/\delta z = (-2.4 \pm 0.5) \times 10^{-5}$. These values are taken as fixed in all subsequent inversions to account for unmodeled ("nuisance") effects such as tropospheric perturbations or orbital artifacts. We estimate the total volume change rate to be $\dot{V}^{(4-patch)} = (-2.7 \pm .9) \times 10^4$ m$^3 \cdot$ yr^{-1} by summing the volume of the four sinks using the estimated dimensions for each source. We calculate the dimensionless misfit $\sqrt{\chi^2_{\nu,obs}} = 3.1$ of the model to the data by the square root of the reduced χ^2-test statistic (Strang & Borre 1997, p. 334; Aster et al. 2013, p. 29). The resulting deformation fields are shown in both unwrapped range change (Fig. 1.3) and wrapped phase change (Fig. 1.4).

1.4.2 "Multi-cube" parameterization

Using the same interferometric pair, we perform linear, geostatistical inversions using the "multi-cube" parameterization for each of the prior models assuming a single grid layer of $(100\text{ m})^3$ cubes with a centroid depth of 100 m based on the lower bounds for dislocation

source depths estimated by Ali et al. (2016a) and depth of saturation in the region. We assume a Poisson's ratio of $\nu = 0.25$.

To account for effects that are unrelated to the deformation on the ground, we calculate a range rate field using the estimated values of the four nuisance parameters from the 4-patch model and then subtract this field from the observed interferogram. The observed field of range change rates with estimates of nuisance parameters removed is shown in Fig. 1.6 and used for modeling with the "multi-cube" parameterization.

The estimated values of thermal strain rate $\dot{\boldsymbol{\epsilon}}^{(\boldsymbol{T})}$ appear in Fig. 1.5. The posterior mean lies within the range of values that we defined as reasonable *a priori*. The mean of the estimates $\mu_{\mathbf{m}}^{(T)} = \overline{\dot{\epsilon}^{(T)}} = -29$ microstrain $\cdot$ yr^{-1}, which lies within the range we considered reasonable, $\alpha_T \dot{T} \in (-42 \pm 29)$ microstrain $\cdot$ yr^{-1}. The largest value of individual parameter uncertainties is 21 microstrain $\cdot$ yr^{-1}, i.e. smaller than the prior uncertainty of 29 microstrain$\cdot$yr^{-1}. Considering cubes where $\dot{V}^{(T)} < -2\sigma_{\dot{V}|\dot{T}}$, with $\sigma_{\dot{V}|\dot{T}} = 82.7$ m$^3\cdot$yr^{-1}, to be cooling significantly, we calculate the volume of the modeled reservoir to be 1.2×10^8 m^3 and the resulting volume change rate of the cubes in the modeled reservoir to be $\dot{V}^{(T)} = (-2.9 \pm 0.3) \times 10^4$ m$^3\cdot$yr^{-1}. Assuming a thermal expansion coefficient $\alpha_T = 3.5 \times 10^{-5}$ K^{-1}, specific heat of the rock $c_{rock} = 948$ J/K/kg (Rutqvist et al., 2002), and a range of values for uniform rock density $\rho_{rock} \in [1900, 2800]$ kg/m^3 (Witter et al., 2016), we find a range for the values of mean rate of change in thermal energy (per unit volume) of the modeled reservoir to be $\overline{\dot{E}} \in [-0.44, -0.65]$ W/m^3. The misfit of the model is $\sqrt{\chi^2_{\nu,obs}} = 1.5$. Using F tests (Wackerly et al., 2007, pp. 536 & 627), we find that the resulting model provides a significantly better fit to the data than does the 4-patch model with 95% confidence (Tables 1.2 and 1.3).

Alternatively, the inversion with the pressure-defined prior yields estimates of poroelastic strain rate $\dot{\epsilon}^{(P)}$ that are not within the range that we defined as reasonable in our prior model (Fig. 1.5). The mean of the estimates $\mu_{\mathbf{m}}^{(P)} = \overline{\dot{\epsilon}^{(P)}} = -33$ microstrain$\cdot$yr^{-1} lies well outside the range of reasonable values $\frac{1}{H}\dot{P} \in (-9.2 \pm 4.8)$ microstrain $\cdot$ yr^{-1}. We do find that the largest

individual parameter uncertainty is $4.6 \times$ microstrain $\cdot$ yr^{-1}, which is smaller than the prior uncertainty of 4.8 microstrain $\cdot$ yr^{-1}. Given $\sigma_{\dot{V}|\dot{P}} = 27.7$ m$^3 \cdot$ yr^{-1}, the volume of the modeled reservoir is estimated to be 1.3×10^8 m^3. The volume change rate of the modeled reservoir is estimated at $\dot{V}^{(P)} = (-2.3 \pm 0.1) \times 10^4$ m$^3 \cdot$ yr^{-1}. The resulting misfit is $\sqrt{\chi^2_{\nu,obs}} = 3.6$, which is larger than the misfit from the inversion with the prior model defined in terms of thermal contraction. Using F tests (Wackerly et al., 2007, pp. 536 & 627), we find that the pressure-defined prior model provides a significantly worse fit to the data than both the temperature-defined "multi-cube" model and the 4-patch model with 95% confidence (Tables 1.2 and 1.3).

The inversion using a linear combination of the temperature- and pressure-defined prior models results in estimates of volumetric strain rates that are within the range that we defined as reasonable *a priori*. There is overlap between the prior and posterior distributions, as shown in Fig. 1.5. The mean of the estimates $\mu_{\mathbf{m}}^{(P+T)} = \overline{\dot{\epsilon}^{(P+T)}} = -29$ microstrain $\cdot$ yr^{-1} lies within the range we considered reasonable, $\frac{1}{H}\dot{P} + \alpha_T \dot{T} \in (-51 \pm 29)$ microstrain $\cdot$ yr^{-1}. The largest value of individual parameter uncertainties is 23 microstrain $\cdot$ yr^{-1}, i.e. smaller than the prior uncertainty of 29 microstrain $\cdot$ yr^{-1}. Considering cubes where $\dot{V}^{(P+T)} < -2\sigma_{\dot{V}|\dot{T}}$, with $\sigma_{\dot{V}|\dot{T}} = 84.9$ m$^3 \cdot$ yr^{-1}, to be cooling significantly, we calculate the volume of the modeled reservoir to be 1.1×10^8 m^3 and the resulting volume change rate of the cubes in the modeled reservoir to be $\dot{V}^{(P+T)} = (-2.8 \pm 0.2) \times 10^4$ m$^3 \cdot$ yr^{-1}. The misfit of this $(P+T)$ solution is $\sqrt{\chi^2_{\nu,obs}} = 1.6$. Using F tests (Wackerly et al., 2007, pp. 536 & 627), we find that the resulting model provides a significantly better fit to the data than does either the 4-patch model or the pressure-defined prior model with 95% confidence (Tables 1.2 and 1.3).

Fig. 1.6 displays the observed, modeled, and residual deformation fields, respectively, calculated from the results of the inversion using a prior model defined in terms of thermal contraction. We see that most of the significant residuals occur in the southeast portion of the map where the observed deformation field shows scattered values of range change rate. There is still some residual signal in the NE portion of the modeled reservoir area where the model

fails to account for the observed range change rate. However, the residuals in this region under the temperature-defined prior model are within the uncertainties for the data. The volumetric strain rate estimates using the temperature-defined prior model are shown per cube in Fig. 1.7. Also shown are estimates of volumetric thermal power $\dot{E}$ [W/m^3] calculated assuming a specific heat $c_{rock} = 948$ J/K/kg, $\rho_{rock} = 2800$ kg/m^3, and thermal expansion coefficient $\alpha_T = 3.5 \times 10^{-5}$ K^{-1}. The variability of the estimates for the thermal strain rate $\alpha_T \dot{T}$ mapped in Fig. 1.7 suggest local, spatial variations.

1.5 Discussion

We find that both solutions that include the temperature-defined prior model produce estimates of volumetric strain rate within what we consider reasonable *a priori*. In contrast, defining the prior model in terms of pressure alone produces estimates of volumetric strain rates which are larger than what we consider reasonable to attribute to decreasing pore fluid-pressure alone.

We further compare the fits of the three geostatistical solutions using the Bayes Factor F_B, which is the ratio of the likelihood of the model under the alternative hypothesis to the likelihood of the model under the null hypothesis (e.g. Kass & Raftery, 1995; Gelman et al., 2013, p. 183). To interpret the mechanism driving the volume changes at depth, we set the null hypothesis H_0 to be decreasing pore fluid pressure and the alternative hypothesis H_1 to be thermal contraction. We find the value of $F_B = 211.7$ leading to $(2 \ln F_B) = 10.7$. According to the scale by Kass & Raftery (1995), a value of $(2 \ln F_B)$ greater than 10 gives "very strong evidence" against the null hypothesis. Accordingly, we favor the hypothesis of thermal contraction over a decrease in pore fluid pressure, further suggesting that the observed volume change cannot be solely attributed to a decrease in pore fluid pressure. We perform a similar analysis, this time setting the null hypothesis to be thermal contraction and the alternative hypothesis to be a combination of thermal contraction and a decrease in pore fluid pressure. We find the value of $F_B = 0.9$ leading to $(2 \ln F_B) = -0.31$. Using the criterion of Kass & Raftery

(1995), the null hypothesis fails to be rejected. We infer that there is no significant difference between results from interpreting the volumetric strain rates as a linear combination of thermal contraction and a decrease in pore fluid pressure and interpreting the volumetric strain rates as thermal contraction alone. We conclude that thermal contraction of the rock matrix is the dominant mechanism driving the deformation observed by InSAR.

We can use mean values from our temperature-defined and pressure-defined prior models to estimate the relative contributions of thermal and poroelastic strain rates to the estimated volumetric strain rates $\dot{\epsilon}^{(P+T)}$ from the combined model. Following Segall & Fitzgerald (1998), we calculate the relative size of thermoelastic to poroelastic strain rates to be 4.6. Using this ratio, we estimate relative contributions of each strain rate as shown in Fig. 1.8.

We note that our parameterization is dependent on the choice of cube depth and dimensions, as well as the choice of Poisson's ratio. The choice of depth is based on the depth of saturation in the region, where the depth of the phreatic surface is approximately $\sim$100 m based on pressure and temperature surveys of wells (e.g., Patterson et al., 2017), and we choose a cube size of $(100 \text{ m})^3$ accordingly. In a separate series of inversions, we experimented with setting the dimension of each cube to be as large as 500 m, while keeping the depth to the top of the cube constant at 50 m. We found that the misfit of the modeled values of range change rate to the observed values increases with increasing cube dimensions (Table 1.4).

We also varied our choice of Poisson's ratio. Seismic analysis at the study area suggests an average Poisson's ratio of $\nu = 0.35$ for the uppermost 400 m of the subsurface (e.g. Matzel et al., 2017; Feigl & PoroTomo Team, 2017b). Performing an F test similar to that discussed in Section 1.4.2, we find an F statistic value of 1.00, which is less than the critical value of 1.01. Thus, we conclude that results using this choice of Poisson's ratio do not vary significantly from our results using $\nu = 0.25$ at 95% confidence.

Although the map of the parameters is dominated by negative rates of volume change, some cubes along the edges of the field show positive values (Fig. 1.7). We suspect that the

nuisance parameters in the modeling are not able to characterize fully the effects of far-field deformation, atmospheric contributions from the change in refractive index with respect to elevation, and contributions from errors in the orbital trajectory of the satellite, as evidenced by the nonzero range change rates observed far from the production wells (Fig. 1.6). We also see some positive values in the NE portion of the subsiding bowl where inaccurately unwrapped phase values have been excluded from the inverted data set.

We find the region of significant temperature change rate by considering cubes where the estimated rate of temperature decrease $\dot{T} < -2\sigma_{\dot{T}}$. These regions are denoted in Fig. 1.7 by white contour lines. We see that the most apparent region of significant cooling occurs between the locations of the injection and production wells. This result is consistent with the idea that highly permeable conduits along faults channel fluids from shallow aquifers to the deep reservoir tapped by the production wells, as suggested previously by Ali et al. (2016a). Further support for this idea can be found in hydrologic modeling (Patterson, 2018).

We consider the rate of change in thermal energy calculated from our inversion. We assume that the volume of rock that is cooling is the same as the volume of rock that is shrinking (Ali et al., 2016a). Using the estimated rates of cooling and values of c_{rock} and ρ_{rock} above, we calculate the 95% confidence interval for the rate of change of thermal energy for the reservoir to be $\dot{E}_{est} \in [-53, -79]$ Megawatt. The power plant's capacity of $[10, 26]$ $\mathrm{MW_e}$ (e.g., Faulds et al., 2010b; Cardiff et al., 2017) indicates an efficiency on the order of 20 percent.

1.6 Conclusions

We have successfully modeled the observed subsidence at Brady Hot Springs using observed range change rates from an InSAR pair spanning from July 22, 2016 to August 22, 2017 and a "multi-cube" parameterization. In this parameterization, the volume of interest is gridded into a set of $(100\ \mathrm{m})^3$ cubes with each cube representing a combination of three orthogonal rectangular dislocation sources. This formulation allows us to interpret volumetric strain in terms

of pore fluid pressure, thermal expansion, or a combination of the two. When the prior model includes thermal contraction, the "multi-cube" parameterization also provides a significantly better fit at 95% confidence than the 4-patch parameterization.

Geostatistical inversion provides a realistic estimate of the rate of change in thermal energy $\dot{E}_{est}$ that is consistent with an efficiency of the order of 20 percent. We find that solutions which include the temperature-defined prior model best characterize the subsidence signal observed at Brady Hot Springs. Using Bayesian inference, we find "very strong evidence" in favor of thermal contraction as the dominant driving mechanism for the observed deformation.

Our results show that the area of significant temperature change occurs between the injection and production wells, consistent with the idea that faults are channeling fluids from shallow aquifers to the deep reservoir in this geothermal system.

1.7 Acknowledgements

We thank Jeremy Patterson, Lesley Parker, John Akerley, Paul Spielman, Christina Morency, Cliff Thurber, and Herb Wang for helpful discussions. Additionally, we thank Bret Pecoraro, Geoffrey Blewitt, and Corné Kreemer for help with Global Positioning System data collection and analysis. We thank two anonymous reviewers for helpful comments. Several figures were created using the Generic Mapping Tools (Wessel et al., 2013). We gratefully acknowledge support from the Weeks family to the Department of Geoscience at the University of Wisconsin-Madison. Synthetic Aperture Radar data from the TerraSAR-X (Pitz & Miller, 2010) and the TanDEM-X (Krieger et al., 2007) satellite missions operated by the German Space Agency (DLR) were used under the terms and conditions of Research Project RES1236. Research was partially supported by grants from U.S. National Science Foundation (EAR-0810134, EAR-1654649) and by the Geothermal Technologies Office of the U.S. Department of Energy under grants DE-EE0005510 and DE-EE0006760. Elena C. Reinisch was supported by a National Science Foundation Graduate Research Fellowship (DGE-1256259) and an Ad-

vanced Opportunity Fellowship from the Graduate School at UW-Madison.

Table 1.1: Comparison range change values estimated from GPS and observed by InSAR.

	$\overline{\Delta\rho} \pm \sigma$ [mm]
GPS	13.45 ± 2.88
InSAR	9.87 ± 3.29
DIFF	3.58 ± 4.37

Table 1.2: Results from F-tests for model complexity at 95% confidence level (e.g., Wackerly et al., 2007, p. 627).
H_0: no significant difference in fits between 4-patch model and more complex "multi-cube" model
H_a: more complex "multi-cube" model provides a significantly better fit than 4-patch model (i.e., the complexity is justified)

comparison	df_1	df_2	test value	critical value	result
4-patch vs. $\dot{\epsilon}^{(T)}$	159556	157941	319.90	1.01	reject H_0
4-patch vs. $\dot{\epsilon}^{(P)}$	159556	157941	-20.76	1.01	fail to reject H_0
4-patch vs. $\dot{\epsilon}^{(P+T)}$	159556	157941	269.32	1.01	reject H_0

Table 1.3: Results from equality of variance F-tests at 95% confidence level (e.g., Wackerly et al., 2007, p. 536). Model 2 is defined by having a larger variance of residuals than model 1.
H_0: variance of residuals from model 2 is not significantly larger than variance of residuals from model 1
H_a: variance of residuals from model 2 is significantly larger than variance of residuals from model 1

model 1	model 2	test value	critical value	result
$\dot{\epsilon}^{(T)}$	4-patch	3.22	1.01	reject H_0
$\dot{\epsilon}^{(T)}$	$\dot{\epsilon}^{(P)}$	3.51	1.01	reject H_0
4-patch	$\dot{\epsilon}^{(P)}$	1.09	1.01	reject H_0
$\dot{\epsilon}^{(P+T)}$	4-patch	3.24	1.01	reject H_0
$\dot{\epsilon}^{(P+T)}$	$\dot{\epsilon}^{(P)}$	3.54	1.01	reject H_0
$\dot{\epsilon}^{(T)}$	$\dot{\epsilon}^{(P+T)}$	0.99	1.01	fail to reject H_0

Table 1.4: Misfit $\sqrt{\chi^2_{\nu,obs}}$ for varying cube dimensions.

cube width	depth	$\sqrt{\chi^2_{\nu,obs}}^{(T)}$
100 m	100 m	1.5
200 m	150 m	1.7
500 m	300 m	2.4

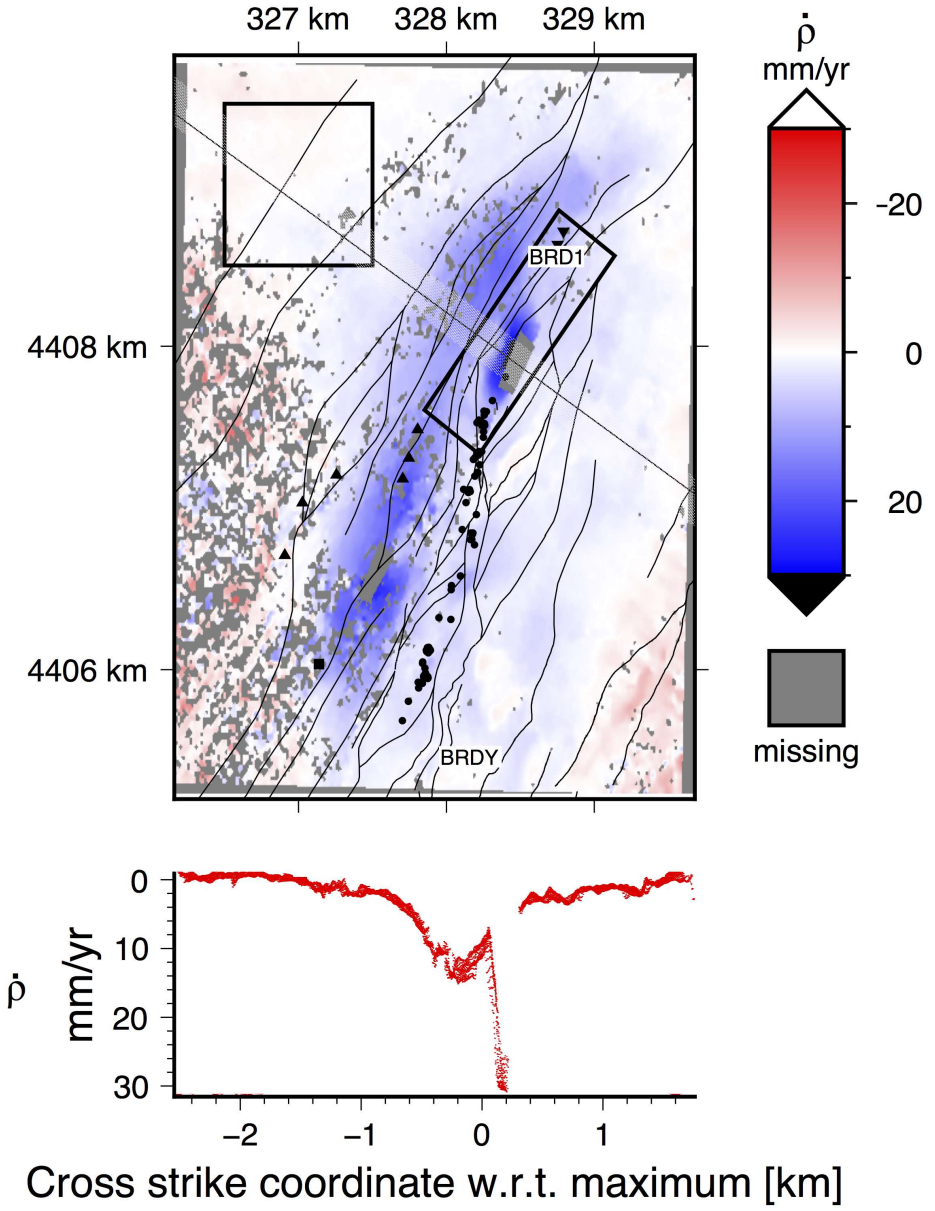

Figure 1.1: a) Deformation field measured by InSAR data, showing observed rates of change in range $\dot{\rho}$ between July 22, 2016 and and August 22, 2017, in map view (a) and profile (b). Blue regions denoting an increase in range indicate subsidence. The two regions of phase discontinuities masked from analysis are shown as gray patches. The rectangle in the NW corner outlines the region used for estimating far-field deformation. The rectangle in the NE outlines the study area for the PoroTomo experiment. GPS stations are labeled in white. Injection wells are shown as inverted triangles, production wells are upright triangles, and the stimulation well 15-12 is denoted as a solid black square. Faults from Jolie et al. (2015) are shown with thick black lines. Fumaroles from Coolbaugh et al. (2004) are shown with filled circles. The black line bisecting the study area shows the profiled region. Coordinates are Easting and Northing in the Universal Transverse Mercator (UTM) projection on the WGS84 ellipsoid zone 11 N (Snyder, 1987).

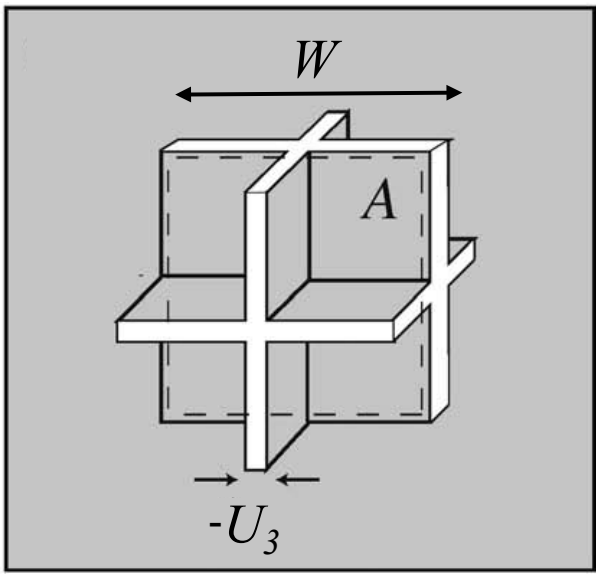

Figure 1.2: Sketch of the cubic sink model, showing three orthogonal, planar dislocations. The width W represents the dimension of each orthogonal square patch, A represents the surface area of each patch, and $-U_3$ represents the tensile closing of each patch. The sketch is modified from Bonafede & Ferrari (2009), their fig. 2(iii).

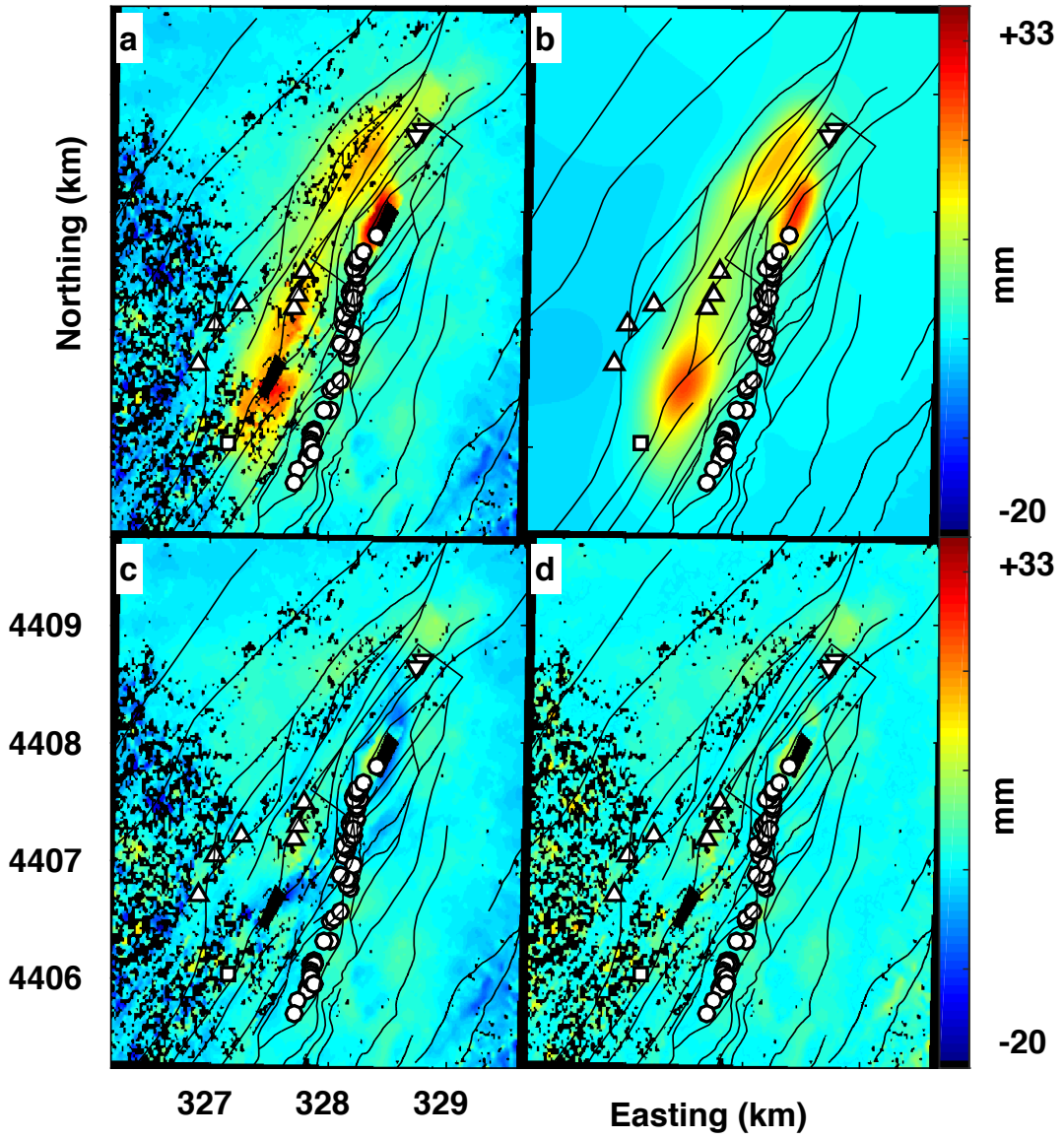

Figure 1.3: Deformation fields in terms of (unwrapped) range change from 22 July 2016 to 22 August 2017 analyzed using the 2-step inversion process outlined in Reinisch et al. (2016). The estimate of the parameter vector was based on a 4-patch model by Ali et al. (2016a). Inversion was first performed using unwrapped range changes. Inversion using the resulting model estimate as a starting model estimate was then performed on wrapped phase changes. Results are shown in terms of unwrapped range change: observed range change (a), modeled range change (b), residual between observed and modeled (c), and absolute value of residuals (d). The blocked rectangular region represents the study area for the PoroTomo experiment. Injection wells are shown as inverted triangles, production wells are upright triangles, and the stimulation well is denoted as a square. Faults are shown with black lines. Fumarole locations are denoted with circles. We use the UTM coordinate system as in Fig. 1.1.

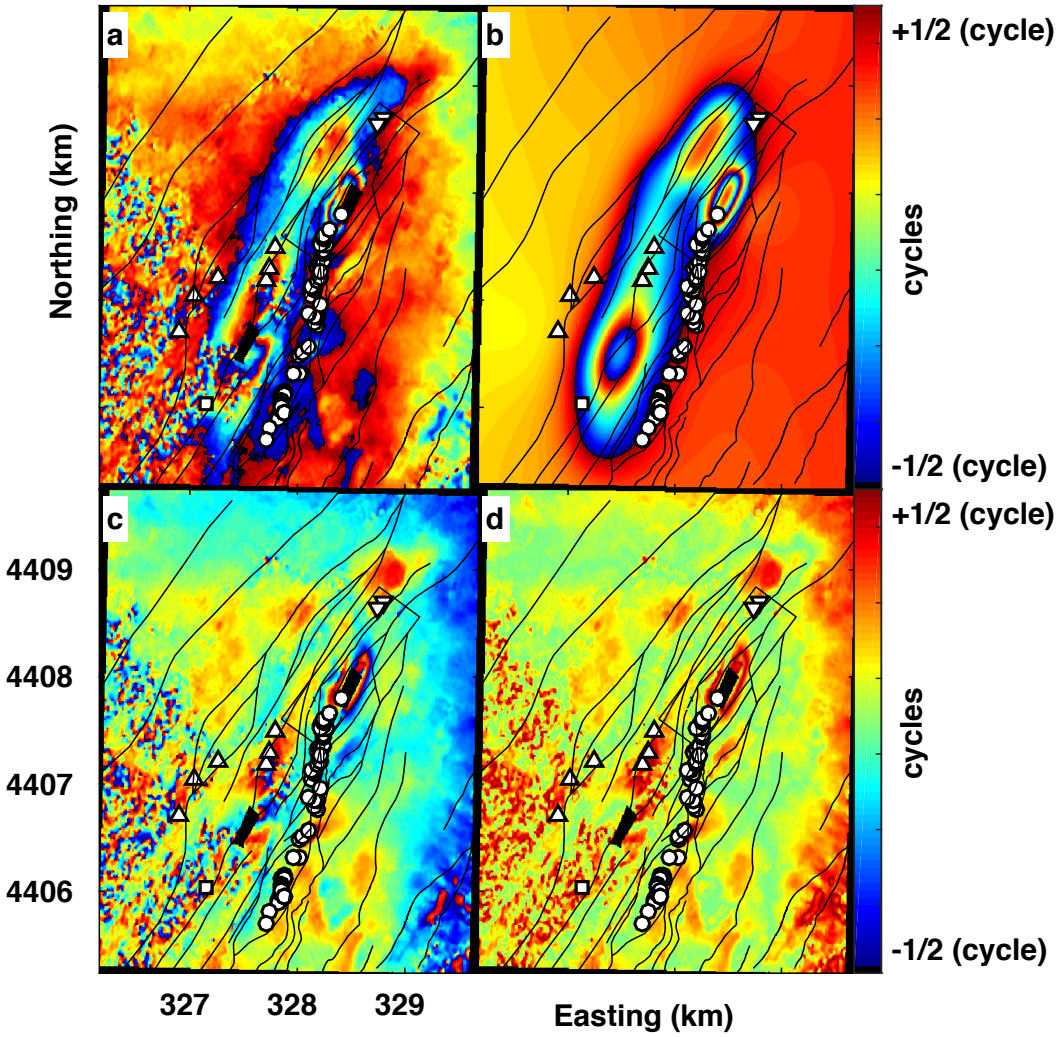

Figure 1.4: Deformation fields in terms of wrapped phase change from 22 July 2016 to 22 August 2017 of the 2-step inversion process outlined in Reinisch et al. (2016), showing observed values (a), modeled values (b), residual values (c), and angular deviation (d). One cycle (or fringe) of color corresponds to 15.5 mm of range change. Plotting conventions as in Fig. 1.3.

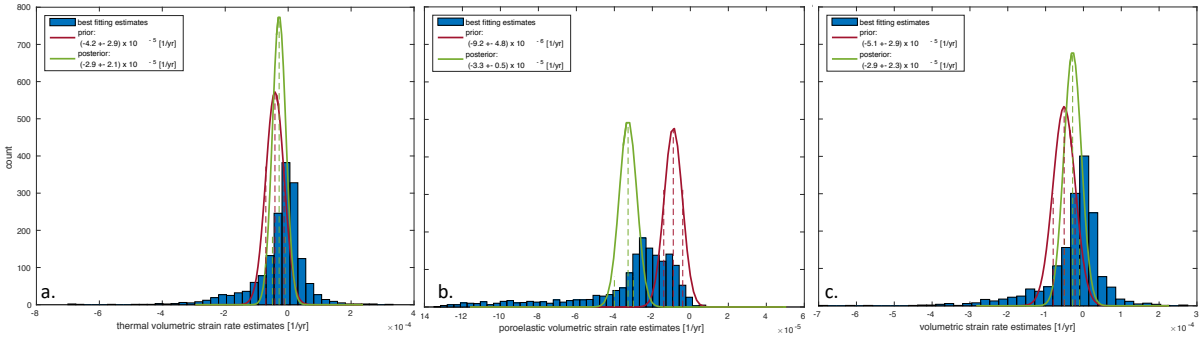

Figure 1.5: Histogram of best fitting estimates of volumetric strain rates for (a) temperature-defined prior, (b) pressure-defined prior, and (c) prior combining temperature and pressure. Overlain are posterior probability densities for both the prior (red) and posterior (green) models.

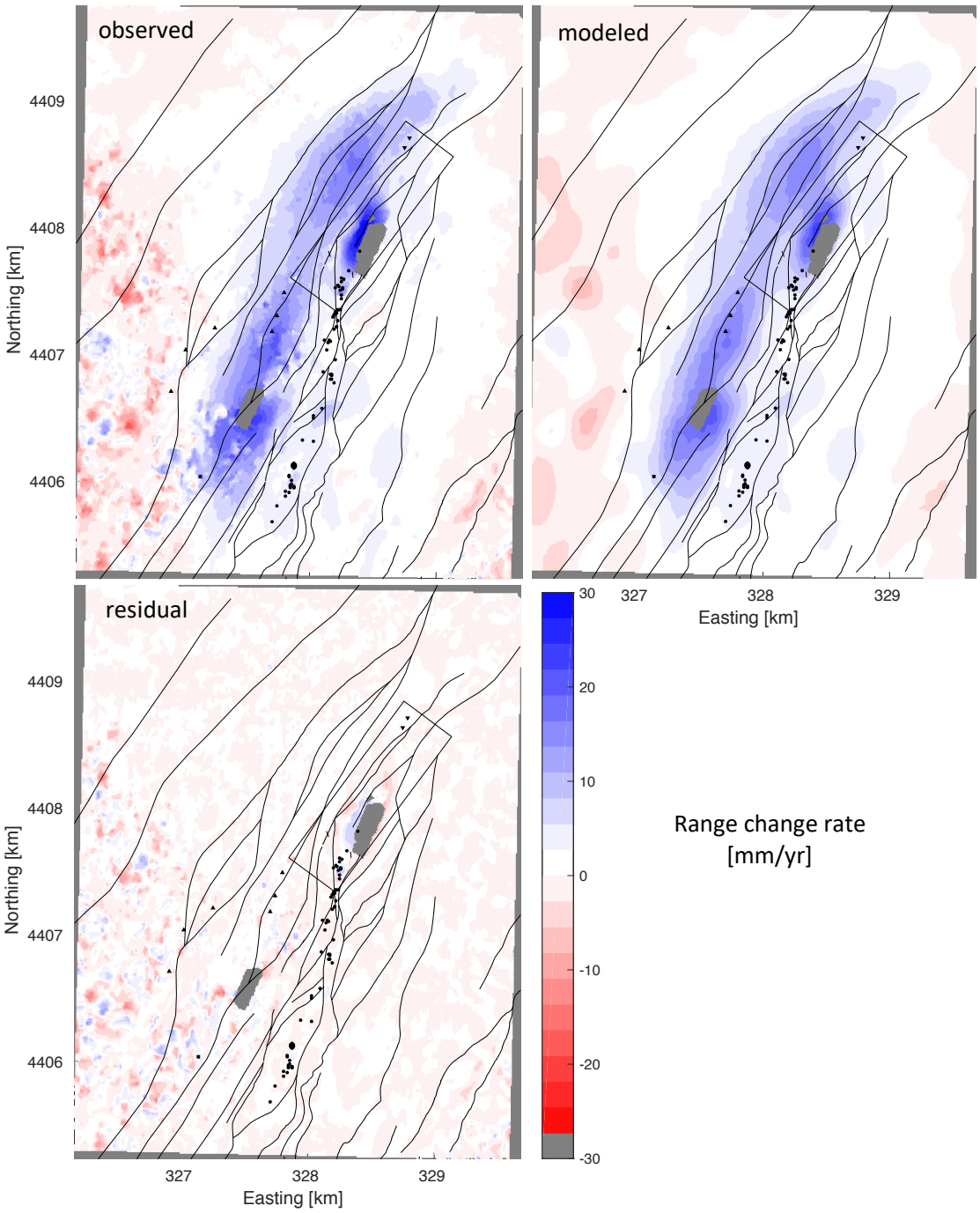

Figure 1.6: Maps of deformation fields for linear, geostatistical inversion with a prior model defined in terms of thermal contraction. The observed deformation field with nuisance effects removed spans from 22 July 2016 to 22 August 2017 and is plotted as rate of range change $\dot{\rho}$. Modeled values of range change rate $\dot{\rho}$ are calculated from best fitting estimates using a temperature-defined prior model. Residual values are shown as observed minus modeled values. Plotting conventions as in Fig. 1.3.

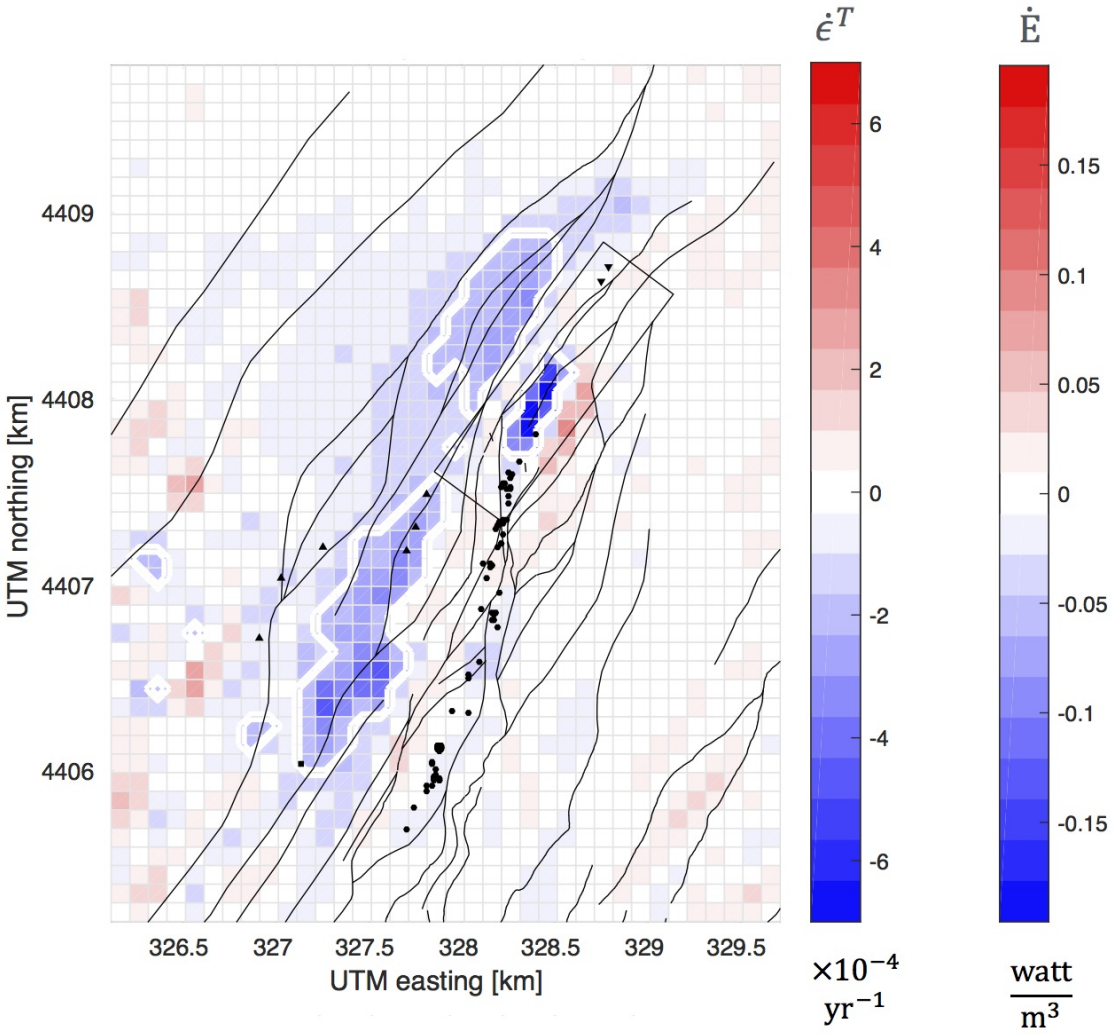

Figure 1.7: Map of parameters estimated from a linear, geostatistical inversion using a prior model defined in terms of thermal contraction. The color of each square denotes the rate of change in a cube (with width $W = 100$ m) in the model. Estimates of $\dot{\epsilon}^{(T)}$ are shown in yr^{-1}. Estimates for thermal energy change rate $\dot{E}$ are shown assuming $c_{rock} = 948$ J/K/kg and $\rho_{rock} = 2800$ kg/m^3. The white line bounds the reservoir region defined by $\dot{V}^{(T)} < -2\sigma_{\dot{V}|\dot{T}}$. Other plotting conventions as in previous figure.

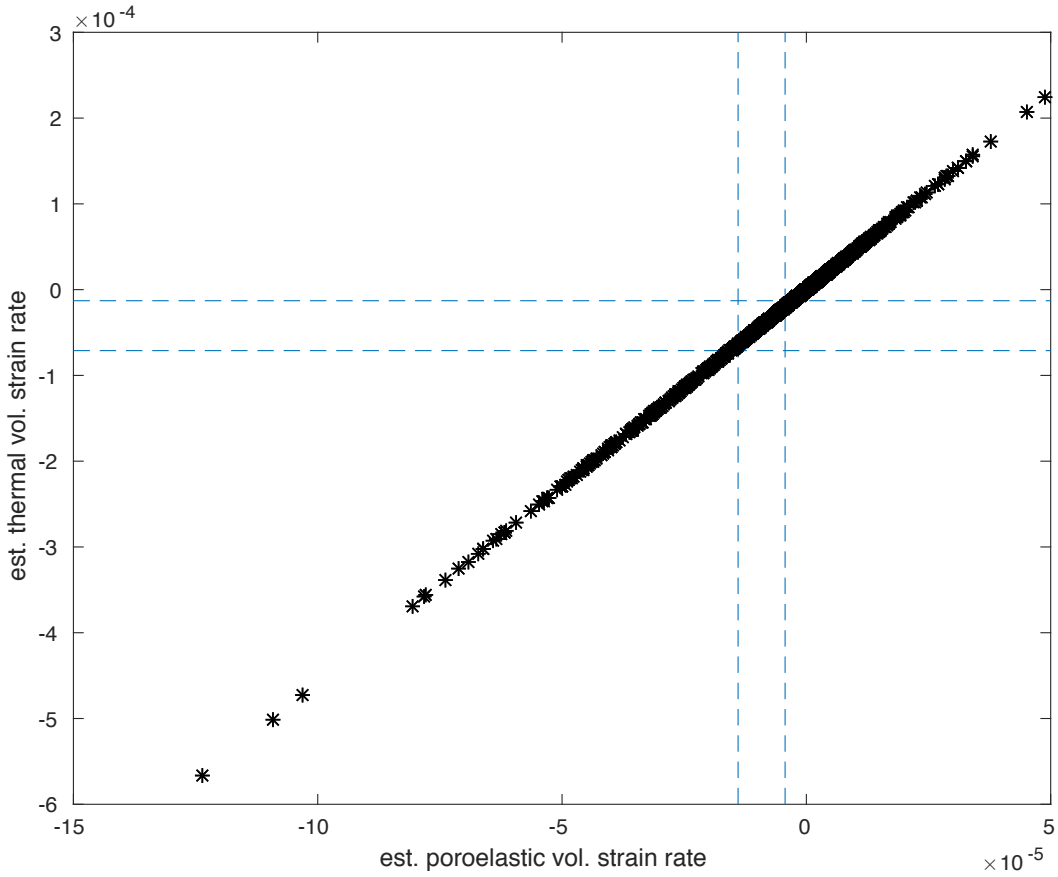

Figure 1.8: Estimates of contributions from thermal strain rate $\dot{\epsilon}^{(T)}$ and poroelastic volumetric strain rate $\dot{\epsilon}^{(P)}$ to best fitting estimates of volumetric strain rates from a linear, geostatistical inversion using a prior model defined in terms of both thermal contraction and a decrease in pore fluid pressure. Prior models for thermal volumetric strain rate (Equation 1.13) and poroelastic volumetric strain rate (Equation 1.14) are shown in blue in terms of 68% confidence intervals.

2 Time-series Analysis of Volume Change at Brady Hot Springs, Nevada, USA Using Geodetic Data from 2004-2018

This work has been submitted to *Journal of Geophysical Research - Solid Earth* on April 15, 2019 with the following author list: Elena C. Reinisch, Michael Cardiff, Corné Kreemer, John Akerley, and Kurt L. Feigl.

Abstract

Brady Hot Springs geothermal field has exhibited subsidence, as measured by interferometric synthetic aperture radar (InSAR). Previous studies have examined both the temporal evolution of the deformation from 2004 through 2016 and the spatial extent of the deformation, directly relating the observed subsidence to volumetric changes below the surface. We extend the modeling at Brady to analyze a data set of interferometric pairs spanning from 2004 through 2018. We examine spatial and temporal trends in the observed deformation by time-series analysis of each of the 1656 cubic voxels in a parameterized elastic dislocation model to identify areas where the subsurface volume changes as a function of time. Joint time-series analysis of Global Positioning System and InSAR pairs confirm significant changes in rates of volume change during time intervals when well operations were varied. The rate of subsidence increases with increased injection, consistent with the identification of thermal contraction of the rock matrix as the dominant driving mechanism. Conversely, the modeled volume increases when pumping ceases, suggesting thermal expansion of the rock matrix.

2.1 Introduction

Brady Hot Springs is a geothermal field in the northwestern Great Basin. Situated about 80 kilometers northeast of Reno, Nevada, it lies between the Truckee Range and the Northern

Hot Springs Mountains. The area is characterized by several NNE-striking normal faults that comprise one of the three major faults systems of the Great Basin region (Benoit et al., 1982; Faulds et al., 2003; Jolie et al., 2015); this major fault dips WNW (Faulds et al., 2003, 2010a). Although a few minor seismic events have been recorded following the installation of a monitoring network in 2010, the largest recorded earthquake to date occurring within 10 km of Brady had a local magnitude of 2.2 (Nathwani et al., 2011; Foxall, 2014, 2016; Cardiff et al., 2017).

The Brady site itself is located within a 600-m-wide left fault step in the fault trace. This structure contains several N-striking, *en échelon* faults acting as highly permeable conduits that channel fluids through the geothermal system (Ali et al., 2016a; Feigl & PoroTomo Team, 2017a; Cardiff et al., 2017; Reinisch et al., 2018). Surface evidence of geothermal activity is visible at Brady as fumaroles, sinter, warm ground and mud pots (Faulds et al., 2010b). A geothermal plant has been in operation at the site since 1992. Currently, the Brady Complex (consisting of the Brady and Desert Peak fields) has a generating capacity of roughly 26 MW. Fluid is produced at depths between 400 and 1770 m via six production wells located in the southwest portion of the field. After the generation of electricity, the majority of the fluid is returned at depths of roughly 200 m via two injection wells located in the northeast portion of the field. The faults within the system are then believed to channel this fluid back to the deep geothermal reservoir to complete the cycle.

Within the past three years, there have been two instances of extended site shutdowns at Brady. The first site shutdown occurred as part of the Department of Energy project entitled "Poroelastic Tomography by Adjoint Inverse Modeling of Data from Seismology, Geodesy, and Hydrology" (PoroTomo). This project, which ran from 2014 through 2018, was supported by the Geothermal Technology Office of the U.S. Department of Energy to assess the integration of various geophysical observation and analysis methods to characterize the subsurface material properties at Brady Hot Springs. During March 2016, termed the project's "deploy-

ment period", well operations were varied at the site while the PoroTomo Team used a variety of techniques to monitor any changes in geophysical processes. There were four stages to the deployment period in March 2016. The first stage was normal operations at the site, during which some of the produced fluid was reinjected at an off-site location. Stage 2, which began on March 14, consisted of a site shutdown until the start of Stage 3 on March 18. From March 18 to March 24, the site came back online with increased infield injection and pulsing. During this time interval, all of the fluid removed during the production process was reinjected back into the field. Stage 4, which began on March 25, was a return to normal operations. The second extended site shutdown started on February 22, 2018, with well operations halted at Brady. This continued until May 1, 2018, at which time most of the wells were back online.

Deformation at rates as high as ~ 25 mm/yr has been previously observed at Brady using interferometric synthetic aperture radar (InSAR). The temporal evolution of such deformation was studied by Ali et al. (2016a), who used time-series analysis of volume change estimates (derived from non-linear inverse modeling of unwrapped range change rates) to test hypotheses regarding the subsurface processes driving the observed deformation. Their time-series data spans the interval from 2004 through 2014.

A recent study by Reinisch et al. (2018) explores the spatial deformation pattern at Brady. Using geostatistical inversion, they estimated volumetric strain rates for a grid of $(100\text{ m})^3$ cubes across a deformation field of unwrapped range change rates from a single InSAR pair spanning 2016 July 22 to 2017 August 22. By applying this inversion in a Bayesian framework, they further identified thermal contraction of the rock matrix as the most likely driving mechanism of the observed subsidence at Brady and interpret the best-fitting estimates as thermal volumetric strain rates.

In this study, we expand on the results of Reinisch et al. (2018) by applying their parameterization to a data set of interferometric pairs spanning from 2003 through 2018 covering Brady Hot Springs. We explore spatial changes in thermal volumetric strain rates through

time using temporal adjustment techniques (e.g. Reinisch et al., 2017) and update the previous interferometric time series performed at Brady. We also use GPS data to identify changes in deformation when well operations were varied in March 2016 and again in early 2018 to further determine the relationships between pumping and deformation at the site.

2.2 Data

2.2.1 InSAR

We use InSAR data from numerous satellites. The German Space Agency (DLR) operates a satellite, TerraSAR-X (TSX) (Pitz & Miller, 2010) which has a repeat time of 11 days. Its radar sensor has an (X-band) wavelength of about 30 millimeters. We work with pairs from tracks 53, 91, and 167 with epochs ranging from 2011 through 2017. To cover years before TSX was operational, we also work with data archived by the Western North America InSAR (WInSAR) Consortium [https://winsar.unavco.org/]. Data from Japan Aerospace Exploration Agency's Advanced Land Observing Satellite (ALOS) tracks 215 and 216 provide coverage from 2006 to 2011. ALOS was a satellite mission with a repeat time of 46 days and an (L-band) radar wavelength of about 240 mm (Rosenqvist et al., 2007). To cover the time interval between 2004 and 2006, we use data from track 485 of the European Space Agency's second European Remote-Sensing Satellite (ERS-2) which carried a radar with a (C-band) wavelength of roughly 57 mm (Francis et al., 1995).

Interferograms are calculated by combining pairs of compatible images. Pairs are formed using GMTSAR (Sandwell et al., 2011a,b), an interferometric processing software package that utilizes Generic Mapping Tools (GMT) to create and visualize interferometric pairs. GMTSAR also allows for removal of noise by applying a modified Goldstein filter that depends on coherence (Goldstein & Werner, 1997; Baran et al., 2003; Sandwell et al., 2011b). Unwrapping is performed using Snaphu (Chen & Zebker, 2000).

We select an optimal subset of pairs from our data set by applying a minimum spanning tree (MST) algorithm using orbital separation (also known as the perpendicular component of baseline $B_\perp$) as the weighting criterion (e.g., Reinisch et al., 2017). The resulting minimum spanning forest (MSF) data set has 196 pairs spanning from April 2003 to October 2018, as shown in Figure 2.3. This data set is publicly available (Reinisch, 2017).

2.2.2 GPS

We also work with data from two continuously operating Global Positioning System (GPS) stations BRD1 and BRDY in the MAGNET network (Figure 2.1). Data from these stations have been analyzed using standard procedures (Blewitt et al., 2018) to produce daily time series of relative position that are publicly available (Kreemer, 2018). GPS station BRD1 was installed on the casing of a completed well (well 18-1) near the injection wells within the subsiding region at the beginning of March 2016 as part of the PoroTomo project (Feigl & PoroTomo Team, 2017a; Blewitt et al., 2018). We consider measurements from BRDY (located to the SSE of the subsiding bowl) to be representative of far-field deformation, and thus consider differences in relative position measured at BRD1 with respect to BRDY in our analysis. We work with GPS measurements in terms of range change $\Delta\rho$ by taking the negative scalar product of the relative displacement vector $\mathbf{u}$ from GPS with the unit vector $\hat{\mathbf{s}}$ pointing from the pixel on the ground to the radar sensor aboard the satellite:

$$\Delta\rho = -\hat{\mathbf{s}} \cdot \mathbf{u}. \tag{2.1}$$

Measurements of relative position from BRD1 with respect to BRDY in terms of range change are shown in Figure 2.4. Range change estimated from paired values of GPS estimates from BRD1 with respect to BRDY have been used to assess the accuracy of unwrapped range change measurements from InSAR as better than 5 mm (Reinisch et al., 2018).

2.3 Methods

2.3.1 Geospatial Inversion

We begin with spatial analysis of each InSAR pair in the data set. To do so, we apply the "multi-cube" parameterization introduced by Reinisch et al. (2018). The parameterized model is comprised of a single grid layer of 1,656 $(100\text{ m})^3$ cubic voxels centered at 100 m depth. Each cube is represented by three square, orthogonally intersecting planar dislocations ("patches") in an elastic half space (Okada, 1985). We set the length of each side of a patch $W = 100$ m, resulting in an initial volume $V_0 = (100\text{ m})^3$, a volume change $\Delta V = -3W^2U_3$, and a volumetric strain rate $\epsilon_V = -3U_3/W$ for each cubic voxel. Dislocation slip $\mathbf{U} = [0, 0, -U_3]$ is confined to the direction perpendicular to each patch's surface, and slip is uniform across all three patches corresponding to tensile opening or closing. This parameterization describes the observed rates of subsidence in terms of the volume change rate of the reservoir. Similarly, subsidence can be interpreted in terms of volumetric strain rates. Reinisch et al. (2018) previously found that thermal contraction is the most likely driving mechanism for subsidence at Brady; thus, we interpret these estimates as thermal volumetric strain rates. Figure 2.5 shows this parameterization with the corresponding mean volumetric strain rate per cubic voxel after applying this parameterization to all 197 pairs in our data set.

2.3.2 Temporal Adjustment

We analyze the estimated volumetric strain rates using temporal adjustment. This procedure converts pair-wise volumetric strain rates $\dot{\epsilon}$ from a set of interferometric pairs into a series of cumulative values of volumetric strain at distinct points in time (Reinisch et al., 2017). This approach assumes separable temporal and spatial dependencies of the deformation field (Feigl & Thurber, 2009; Reinisch et al., 2017). First, we apply temporal adjustment to each cubic voxel to determine how thermal volumetric strain varies temporally over the field. We start by

using a single-rate parameterization:

$$f_1(t_i) = a_1(t_i - t_0) \tag{2.2}$$

where $t_0 = 2003.32$ is the start date of our data set in decimal years. We also consider a piecewise-linear parameterization[1] with m breaks at times t_m that form $(m-1)$ intervals:

$$\begin{aligned} &f_2(t_i) = \Sigma_{j=1}^{j=m} a_j D(t_i), \text{ where} \\ &D(t_i) = \begin{cases} 0 & \text{if } t_i < t_j \\ (t_i - t_j) & \text{if } t_j \leq t_i < t_{j+1} \\ (t_{j+1} - t_j) & \text{if } t_i \geq t_{j+1}. \end{cases} \end{aligned} \tag{2.3}$$

In addition to considering the full time series of each voxel, we also aim to distinguish temporal variations when pumping rates were changed during the March 2016 deployment period and the Spring 2018 shutdown. Both shutdowns occur after the start of 2016, when the available InSAR pairs are from the TSX mission. The repeat time of TSX is 11 days, making InSAR coverage during the March 2016 deployment period fairly sparse. We supplement the InSAR data with paired daily estimates of GPS data to improve the temporal sampling. To analyze transient changes when well operations were varied, we perform a joint inversion of volume change rates estimated for the deforming region shown in Figure 2.1 from both GPS and InSAR. We define this region as a 3000-m-by-1000-m rectangular area centered on the field (327.91 km Easting, 4407.49 km Northing in UTM zone 11) and oriented along strike of the faulting system (about 36.4° NE). This area includes the area of observed deformation (and significant volumetric strain rate). For each InSAR pair, we arrive at a single estimate of volume change rate for this region by summing individual volume change rate estimates

[1]Equation (2.3) has been modified to use "D(t)" instead of "H(t)" to maintain consistency throughout this dissertation.

for each cube that is in the deforming region. When analyzing the GPS data, we are limited to one location for the data set (i.e., the location of BRD1), making application of the "multi-cube" parameterization impractical. Instead, estimates of volume change rate for the deforming region are derived from GPS using a cuboid parameterization with a single 3000-m-by-1000-m cuboid centered on the field at 100 m depth and 100 m thickness, corresponding to the "multi-cube" parameterization used to model the InSAR data. Here we consider BRD1 an appropriate measurement of deformation since it is located within the subsiding bowl. We continue this joint analysis through the end of the Spring 2018 shutdown.

2.4 Results

2.4.1 Temporal Adjustment of Estimates from MSF Data Set

We use the single-rate parameterization (equation (2.2)) to apply temporal adjustment to estimates of volumetric strain rate for each cubic voxel individually. For each voxel time series, we calculate a dimensionless misfit χ of the best-fitting model to the voxel's data set of volumetric strain rates by the square root of the reduced χ^2-test statistic (Strang & Borre, 1997, p. 334). We find the range of misfits of all 1,656 single-rate time series to be $[1.71, 4.38]$.

We also use a piecewise-linear parameterization for each cubic voxel with breaks at the start and end of Stages 2 and 3 of the Deployment period as well as the 2018 site shutdown (equation (2.3), $m = 6$). We find the range of misfits of all 1,656 cubes to be $[1.62, 3.92]$. To determine if the added model complexity is justified, we perform an F-test for model complexity (e.g. Wackerly et al., 2007) for each of the 1,656 sets of time series between the single-rate parameterization and the piecewise-linear parameterization. We test the null hypothesis that the single-rate parameterization and the piecewise-linear parameterization fit the data equally well. The results are shown in Figure 2.6. Areas where the null hypothesis is rejected are shaded in green. In these areas, there is a significant improvement in fit using the piecewise-

linear parameterization. To interpret this result, we note that the voxels that show significant variability in their strain rate over time are located within the deforming part of the geothermal field. Figure 2.1 shows the cumulative modeled range change from the piecewise-linear parameterization. Yearly values of this cumulative volume change are shown in profile in Figure 2.2. Total cumulative volume change is shown in Figure 2.7.

2.4.2 Temporal Adjustment of Shutdown Periods

In addition to the full time series spanning from 2003 through 2018, we focus on March 2016 and Spring 2018 when pumping operations were varied. We perform temporal adjustment on the volume change rates for the deforming region estimated from GPS and InSAR. As opposed to our previous time-series analysis of volumetric strain rates per cubic voxel with 1,656 voxels in a given interferogram, we now consider a single estimate of volume change for each InSAR pair and each GPS pair. We use a piecewise-linear parameterization with breaks denoting the beginning and ending dates of time intervals when pumping deviated from normal operations (Stages 2 and 3 of the PoroTomo deployment period and between 2018 February 22 and 2018 May 1). Results are shown in Figures 2.8 and 2.9. We find a dimensionless misfit of $\chi = 2.5$.

We test whether the rate of volume change varied between stages using a Student's T-test (e.g., Wackerly et al., 2007). Results are shown in Table 2.1. We reject the null hypothesis (that the rates of volume change during each stage are equal), finding a significant difference between volume change rates of consecutive stages with 95% confidence.

2.5 Discussion

Figure 2.5 shows the mean estimate of the volumetric strain rate per cubic voxel. We see that the estimated volumetric strain rate is significantly different from zero in 31% of the voxels. In map view, each of these rapidly contracting voxels falls within 500 m of an active fault trace. In addition, the area of high magnitudes of strain rate is located along strike of the fault system

and matches the pattern of deformation.

We find that statistically significant differences in misfit values between a single-rate temporal parameterization and a more complex, piecewise-linear parameterization (with breaks when well operations were varied) are located within the deforming area observed by InSAR. This suggests that changes in well operations affect deformation rates within this area. This area also comprises the cubic voxels where the estimated rate of contraction is significantly different from zero (Reinisch et al., 2018). The cumulative range change derived from temporal adjustment using the piecewise-linear parameterizations reflects the trend of the observed subsidence following the strike of the fault system, as noted by previous studies (Ali et al., 2016a; Reinisch et al., 2018).

Joint time-series analysis of volume change rates from GPS and InSAR also shows changes in deformation in response to changes in well operations. We find statistically significant differences between the volume change rates when well operations were normal and the volume change rates when well operations were varied. In particular, we see volumetric expansion during both site shutdowns. To further examine this relationship, we test the correlation between well operations and estimates of volume change rate in the deforming region derived from geodetic data. We assign ordinal values to increasing levels of well operations, with zero indicating a site shutdown, one indicating normal operations, and two indicating increased injection (corresponding to Stage 3 of the Deployment period). Using Spearman's rank correlation test (e.g., Wackerly et al., 2007, p. 786), we test the null hypothesis that the estimates of volume change rate of the deforming region and well operations are not correlated against the alternative hypothesis that they are inversely and monotonically related. We find a Spearman correlation coefficient $r_s = -0.93$ and a p-value of 1.7×10^{-2}. Thus, we reject the null hypothesis at 95% confidence and conclude that the volume change rate of the deforming region is inversely related to the (net) injection rate at the site.

Time-series analysis of geodetic data during the PoroTomo deployment period in March

2016 indicates volumetric expansion during the site shutdown in Stage 2. Conversely, volumetric contraction occurs in the area during all other stages. In particular, we see a faster rate of contraction for Stage 3, when there was increased infield injection and all of the produced fluid was reinjected back into the subsurface. This result supports the idea proposed by Reinisch et al. (2018) that thermal contraction in the subsurface is driving the observed subsidence at Brady.

2.6 Conclusions

Using the "multi-cube"parameterization introduced by Reinisch et al. (2018), we analyze the temporal evolution and spatial extent of deformation at Brady between 2003 and 2018. A piecewise-linear parameterization with breaks during March 2016 and Spring 2018 when well operations were varied best describes the temporal and spatial patterns of deformation at the site. We find that in some of the voxels near the injection wells, the volumetric strain rate varies as a function of time, particularly during time intervals when pumping was suspended. Focusing on time intervals when well operations were varied during the March 2016 deployment period and the 2018 shutdown, we confirm a statistically significant, inverse relationship between estimates of volume change rate of the deforming region and well operations. Site shutdowns correspond with thermal expansion in the subsurface, whereas times of normal operations correspond to thermal contraction. Thermal contraction of the rock matrix in the subsurface is the most likely driving mechanism of the observed subsidence.

2.7 Acknowledgements

We thank Paul Spielman, Herb Wang, Jeremy Patterson, and Lesley Parker for helpful discussions. Additionally, we thank Bret Pecoraro and Geoffrey Blewitt for help with GPS data collection and processing, respectively. Interferograms were created using GMTSAR process-

ing software (Sandwell et al., 2011b). Several figures were created using the Generic Mapping Tools (Wessel et al., 2013). We gratefully acknowledge support from the Weeks family to the Department of Geoscience at the University of Wisconsin-Madison. Synthetic Aperture Radar data from the TerraSAR-X and the TanDEM-X satellite missions operated by the German Space Agency (DLR) were used under the terms and conditions of Research Project RES1236. Raw Synthetic Aperture Radar (SAR) data from the ERS satellite mission operated by the European Space Agency (ESA) are copyrighted by ESA and were provided through the WInSAR consortium at the UNAVCO facility. SAR data from the ALOS satellite mission operated by the Japanese Space Agency (JAXA) were acquired from NASA's Distributed Active Archive Center at the Alaska Satellite Facility (ASF). In accordance with the FAIR principles (Stall et al., 2017; Stall, 2018), InSAR and GPS data for this work are available publicly on the Geothermal Data Repository (Reinisch, 2017; Kreemer, 2018). Data products derived from InSAR and GPS and used in the analysis presented within this work are available publicly (Reinisch, to be submitted upon acceptance of manuscript, currently hosted at ftp://roftp.ssec.wisc.edu/porotomo/PoroTomo/DATA/InSARforGDR). Software is available publicly on GitHub in the General Inversion of Phase Technique (GIPhT) repository (Feigl et al., 2019a) and the PoroTomo repository (Feigl et al., 2019b). Research was partially supported by grants from U.S. National Science Foundation (EAR-1654649 and EAR-1347190) and by the Geothermal Technologies Office of the U.S. Department of Energy under grants DE-EE0005510 and DE-EE0006760. Elena C. Reinisch was supported by grants from National Science Foundation Graduate Research Fellowship (DGE-1256259) and the Graduate School at UW-Madison.

Table 2.1: Results from two-tailed Student's T-test at 95% confidence level (e.g., Wackerly et al., 2007, p. 524) for estimated volume change rates from geodetic data during different stages of the PoroTomo Deployment period[a].

Start of Stage A	Start of Stage B	Rate A $\times 10^5$ m^3/yr	Rate B $\times 10^5$ m^3/yr	df	test value	critical value	result w.r.t. H_0
20160301	20160314	(-1.80 ± 0.56)	(7.45 ± 1.81)	11	-13.76	2.20	reject
20160314	20160318	(7.45 ± 1.81)	(-5.19 ± 0.89)	9	15.18	2.26	reject
20160318	20160324	(-5.19 ± 0.89)	(-0.39 ± 0.01)	627	-147.33	1.96	reject
20160324	20180222	(-0.39 ± 0.01)	(2.03 ± 0.10)	679	-565.11	1.96	reject
20180222	20180501	(2.03 ± 0.10)	(-1.21 ± 0.06)	65	-90.44	2.00	reject

[a] H_0: rates between interval A and interval B are equal
H_1: significant difference in rates between intervals A and B
Degrees of freedom (df) are calculated from the number of pair-wise estimates within each time interval.
This table's format has been modified to meet dissertation formatting requirements.

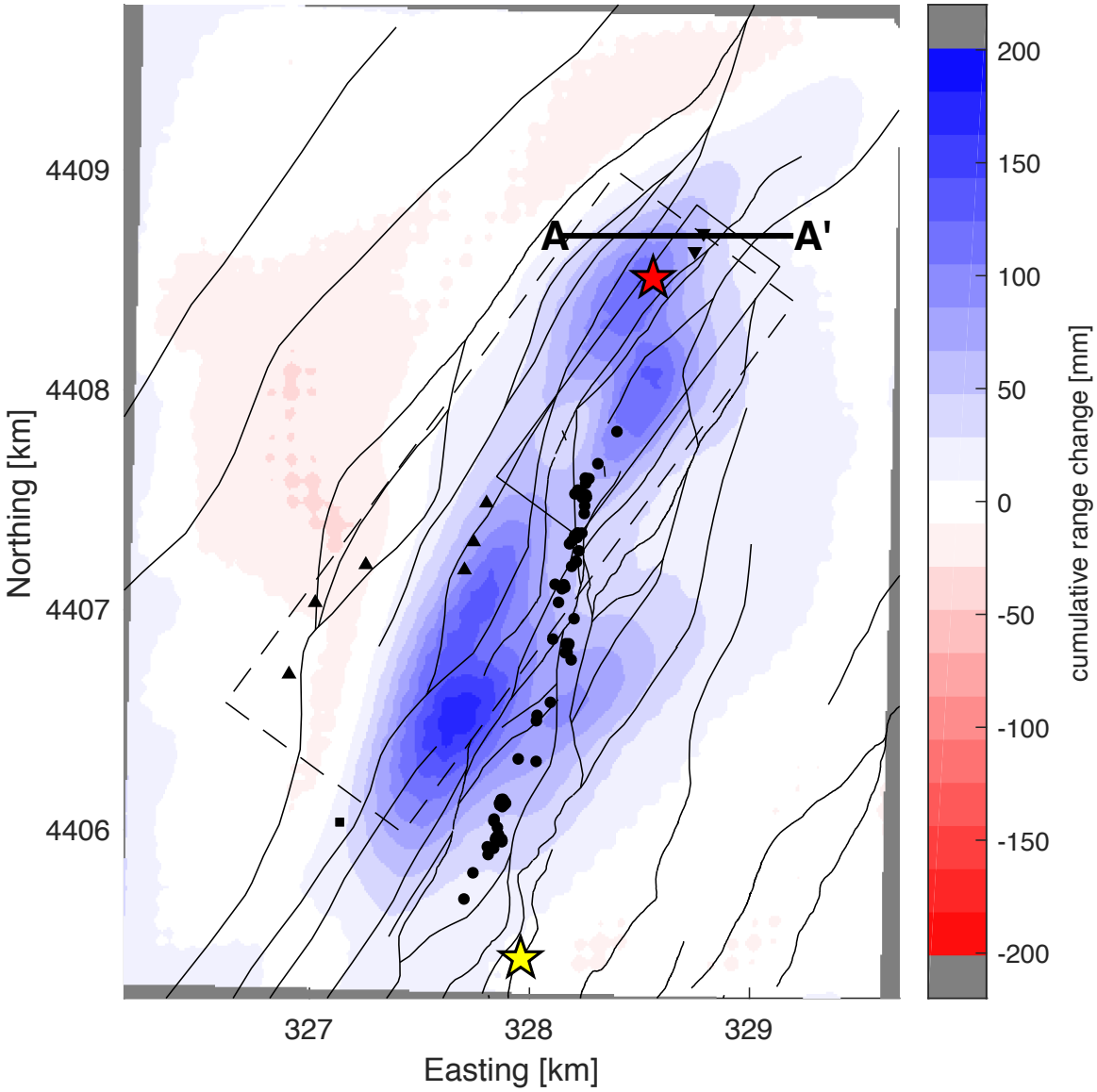

Figure 2.1: Deformation field of modeled cumulative range change in mm from using a piecewise-linear parameterization on volumetric strain rates derived from InSAR pairs from the Envisat, TerraSAR-X, and European Remote Sensing-2 satellites spanning from April 2003 to October 2018. Letters denote the profile sampled in Figure 2.2. Injection wells are shown as inverted triangles, production wells are upright triangles and the stimulation well 15-12 is denoted as a solid black square. Faults from Jolie et al. (2015) are shown with thick black lines. Fumaroles from Coolbaugh et al. (2004) are shown with filled circles. The red star indicates continuous GPS station BRD1. The yellow star indicates continuous GPS station BRDY, which is used as a reference to estimate and remove far-field deformation in our analysis. The solid black line delimits the study area for the PoroTomo project (Feigl & PoroTomo Team, 2017a). The dashed black rectangular area central to the field denotes the deforming region used for analysis of shutdown intervals. Coordinates are easting and northing in the Universal Transverse Mercator (UTM) projection on the WGS84 ellipsoid zone 11 N (Snyder, 1987).

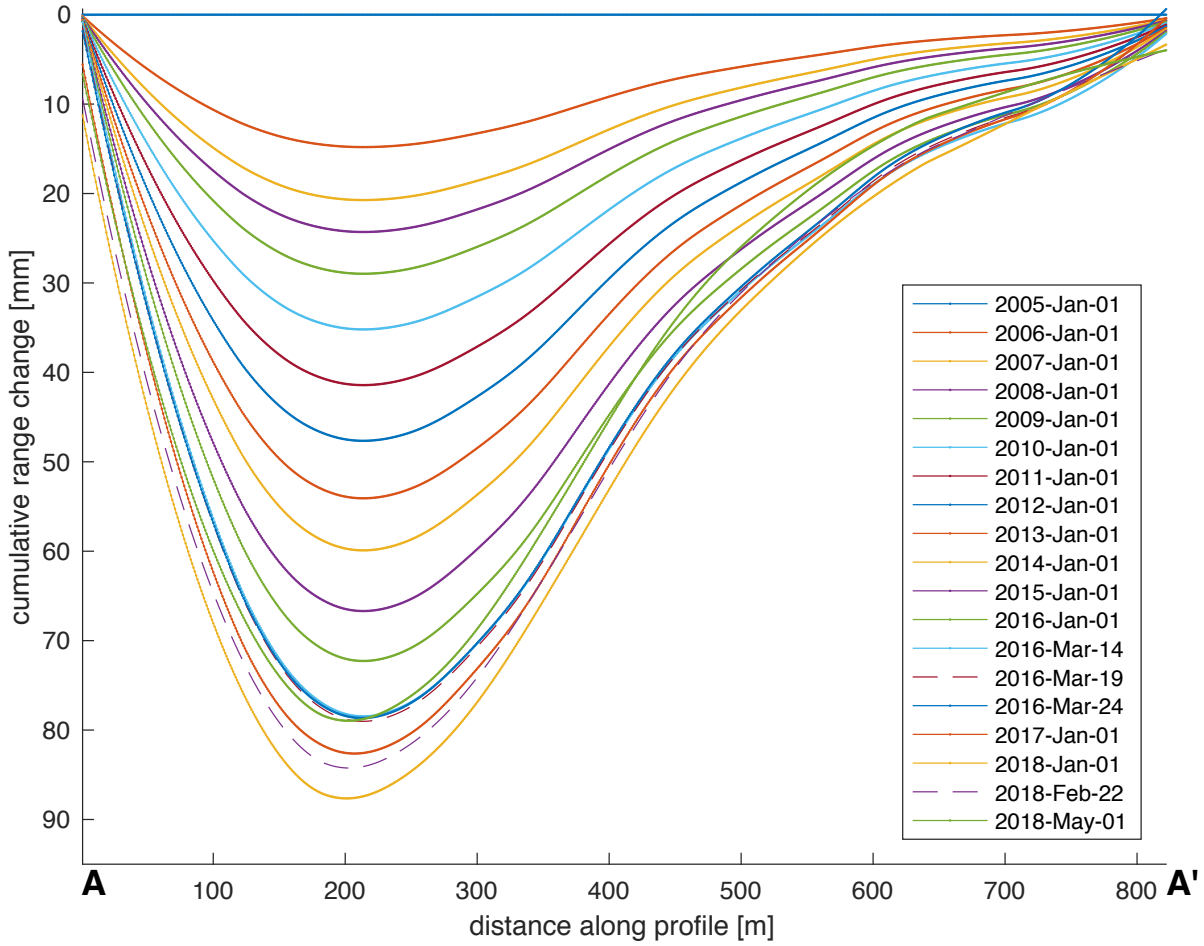

Figure 2.2: Modeled cumulative range change along the east-west profile A - A' mapped in Figure 2.1. Profiles are shown for every year of the data set (solid lines) as well as at the start of each break in the piecewise-linear parameterization corresponding to time intervals when the site was shut down in March 2016 and Spring 2018 (dashed lines).

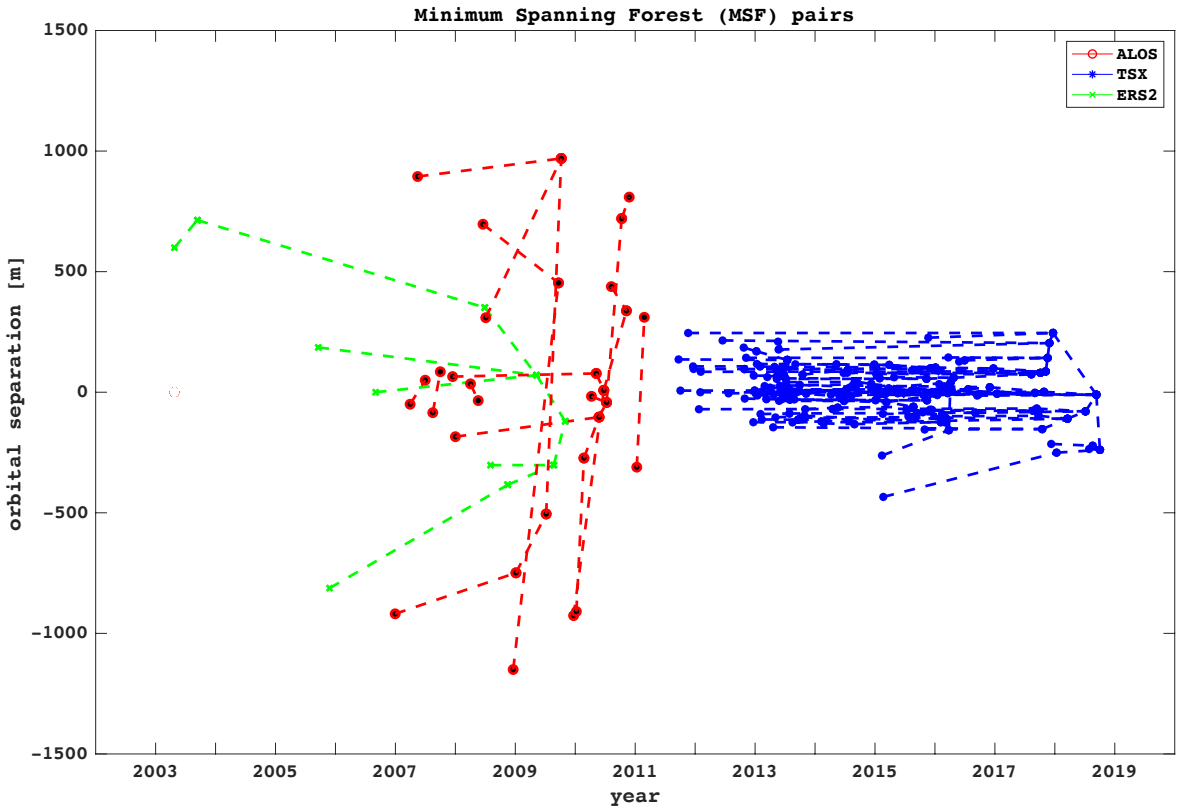

Figure 2.3: Graph showing pairs in the minimum spanning forest data set chosen by minimizing orbital separation. ERS-2 pairs are shown in green, ALOS pairs are shown in red, and TSX pairs are shown in blue.

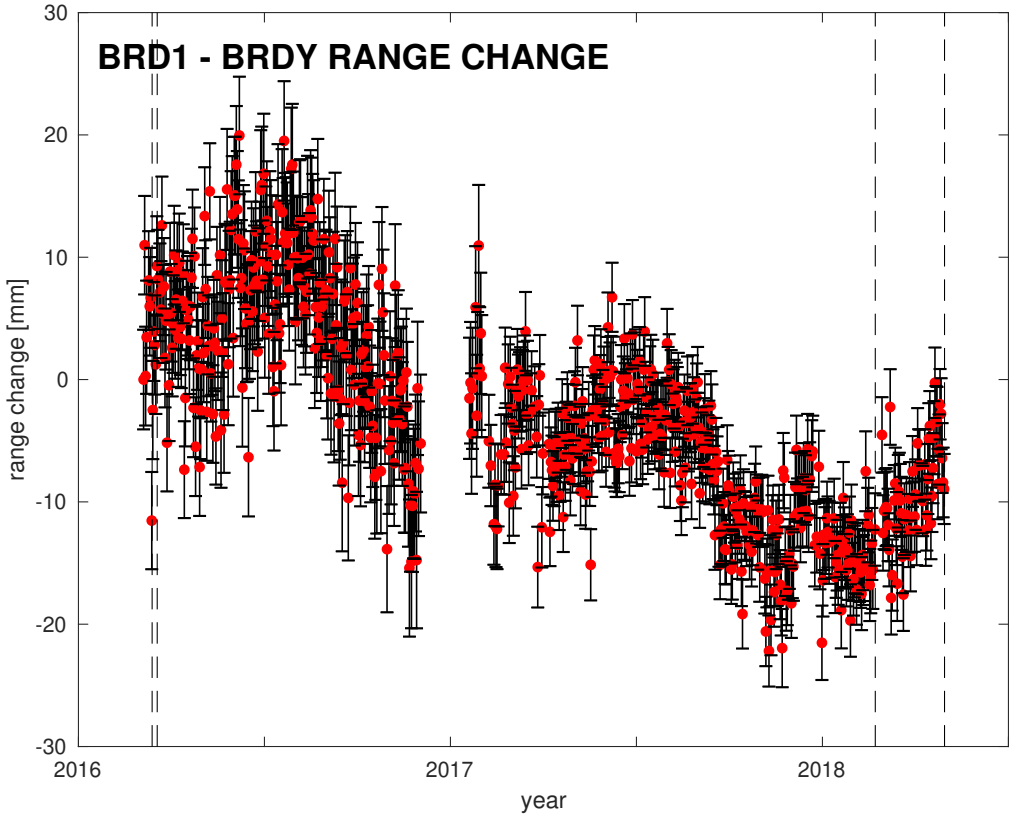

Figure 2.4: Measurements of relative position derived from GPS data of station BRD1 with respect to BRDY in terms of range change along the unit pointing vector $\hat{\mathbf{s}} = [-0.55, 0.10, -0.82]$. Values are shown in red with black bars indicating 1σ uncertainty. Vertical dashed lines delimit shutdown intervals at the site in March 2016 and Spring 2018.

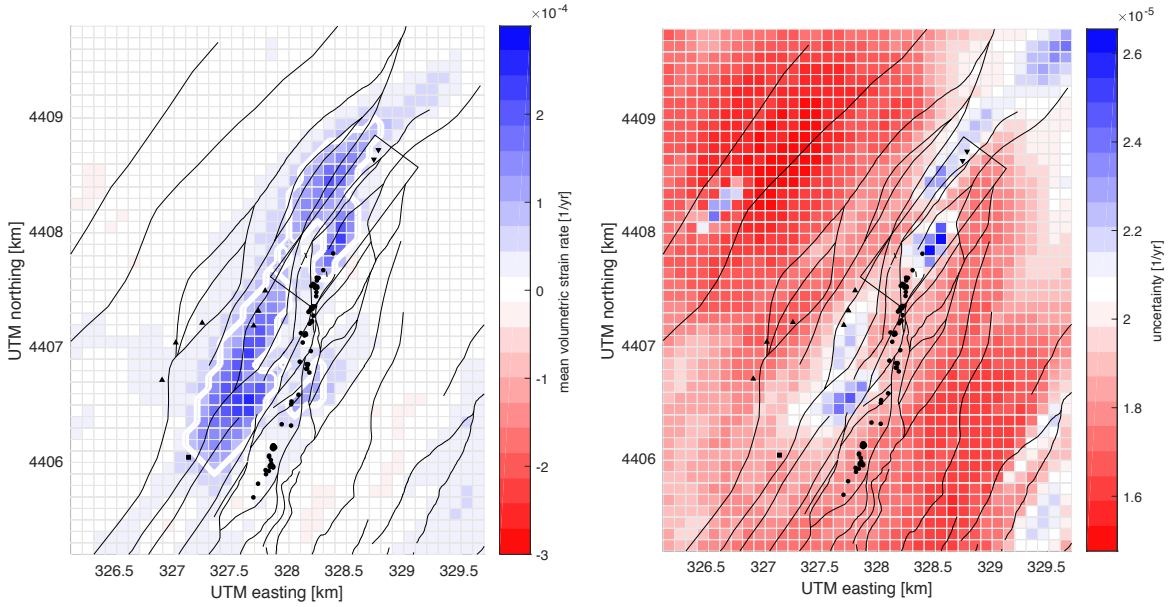

Figure 2.5: Map of mean (thermal) volumetric strain rate estimates $\overline{\dot{\epsilon}^{(T)}}$ per cubic voxel (left) and associated uncertainty per cubic voxel (right). The white line bounds the areas of significant contraction defined by $\overline{\dot{\epsilon}^{(T)}} < -2\sigma_{\dot{T}}$, where $\sigma_{\dot{T}} = 4.0 \times 10^{-5}$ 1/yr is the standard deviation of $\overline{\dot{\epsilon}^{(T)}}$. Other plotting conventions as in Figure 2.1.

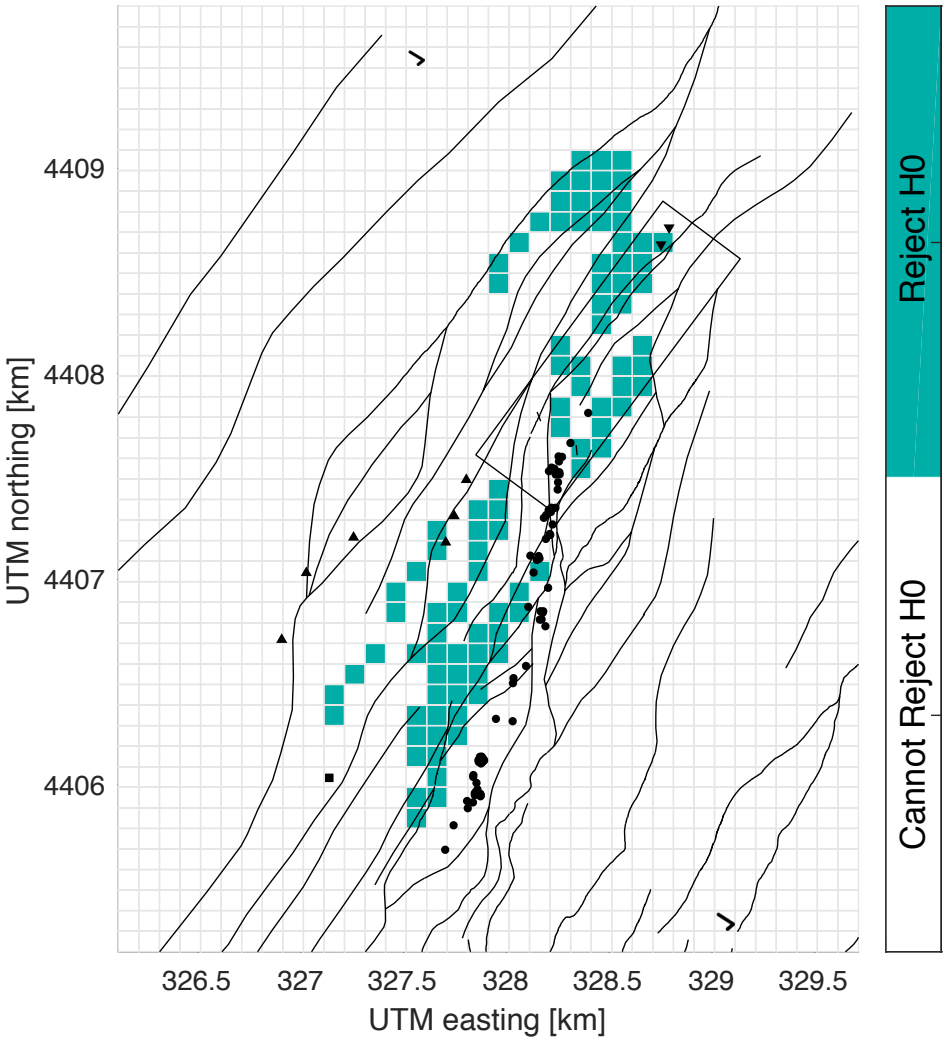

Figure 2.6: Map showing the results from the F-test for model complexity at 95% confidence between a single-rate parameterization and a piecewise-linear parameterization with breaks when well operations were varied in March 2016 and the 2018 shutdown. The grid lines delimit the individual cubes in the time-dependent model. The null hypothesis is rejected at 95% confidence in the cubes highlighted in blue-green. Other plotting conventions as in Figure 2.1.

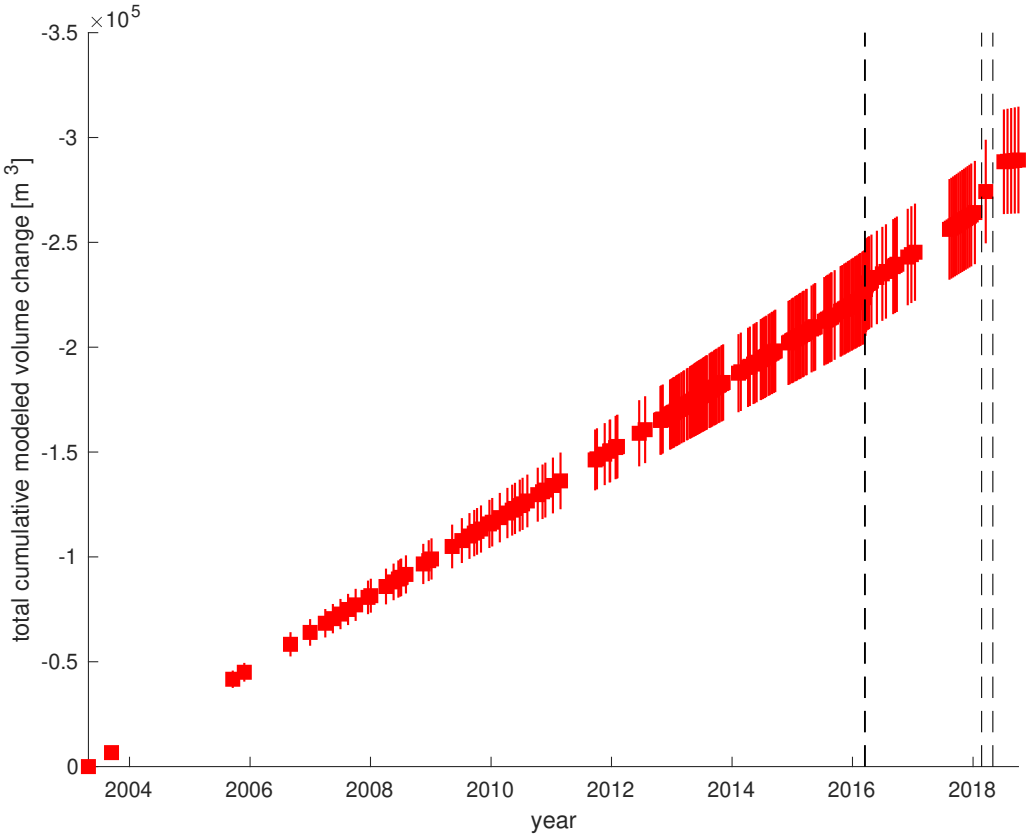

Figure 2.7: Time series of modeled total cumulative volume change with 1σ uncertainty bars using a piecewise-linear parameterization with breaks in March 2016 and Spring 2018 when well operations were varied (vertical dashed lines).

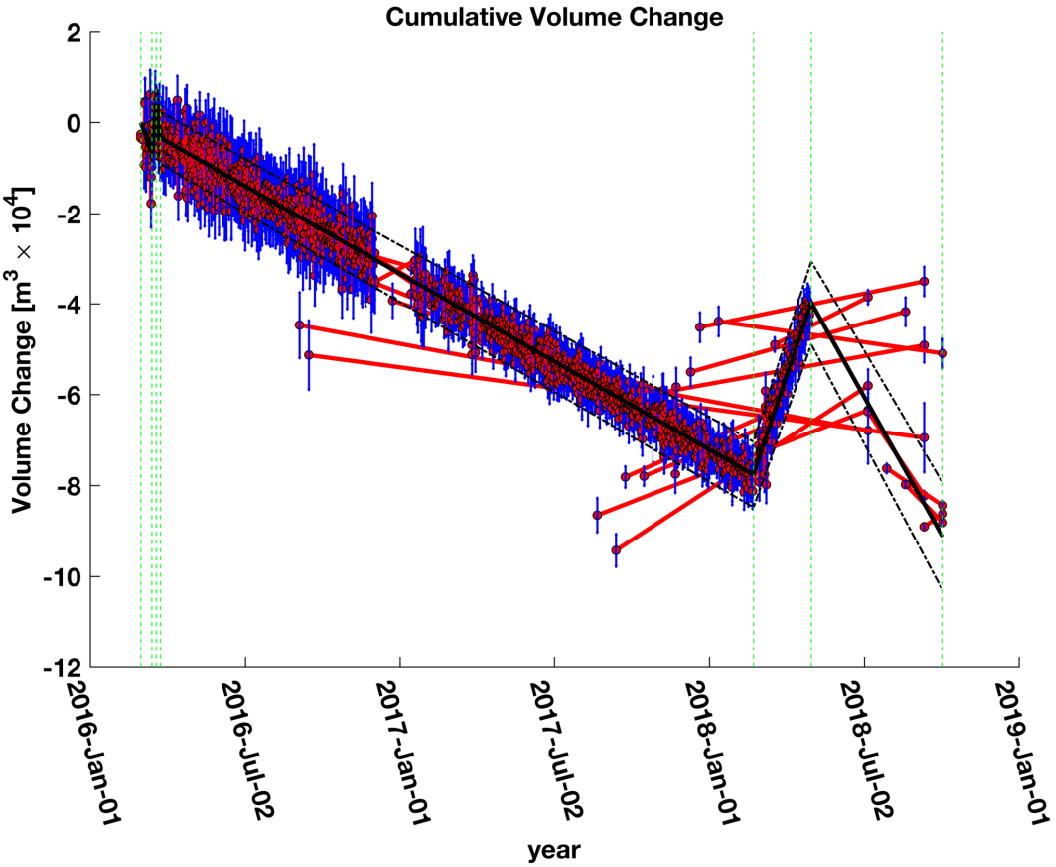

Figure 2.8: Time series spanning the March 2016 deployment period and 2018 shutdown, showing cumulative volume change over time from temporal adjustment of volume change rates estimated from InSAR and GPS data. Black lines show the modeled volume change with 68% confidence intervals (dashed black lines) as estimated by temporal adjustment with a piecewise-linear temporal function with breaks (vertically dashed green lines) at the start/end of each deployment stage and site shutdown (Reinisch et al., 2017). Red segments indicate measurements of observed volume change derived from individual geodetic pairs. For each pair, the volume change at the mid-point of each time interval is plotted to fall on the modeled curve and the vertical blue bars denote 1σ measurement uncertainty after scaling by the square root of the variance scale factor $\sigma_0 = 2.5$.

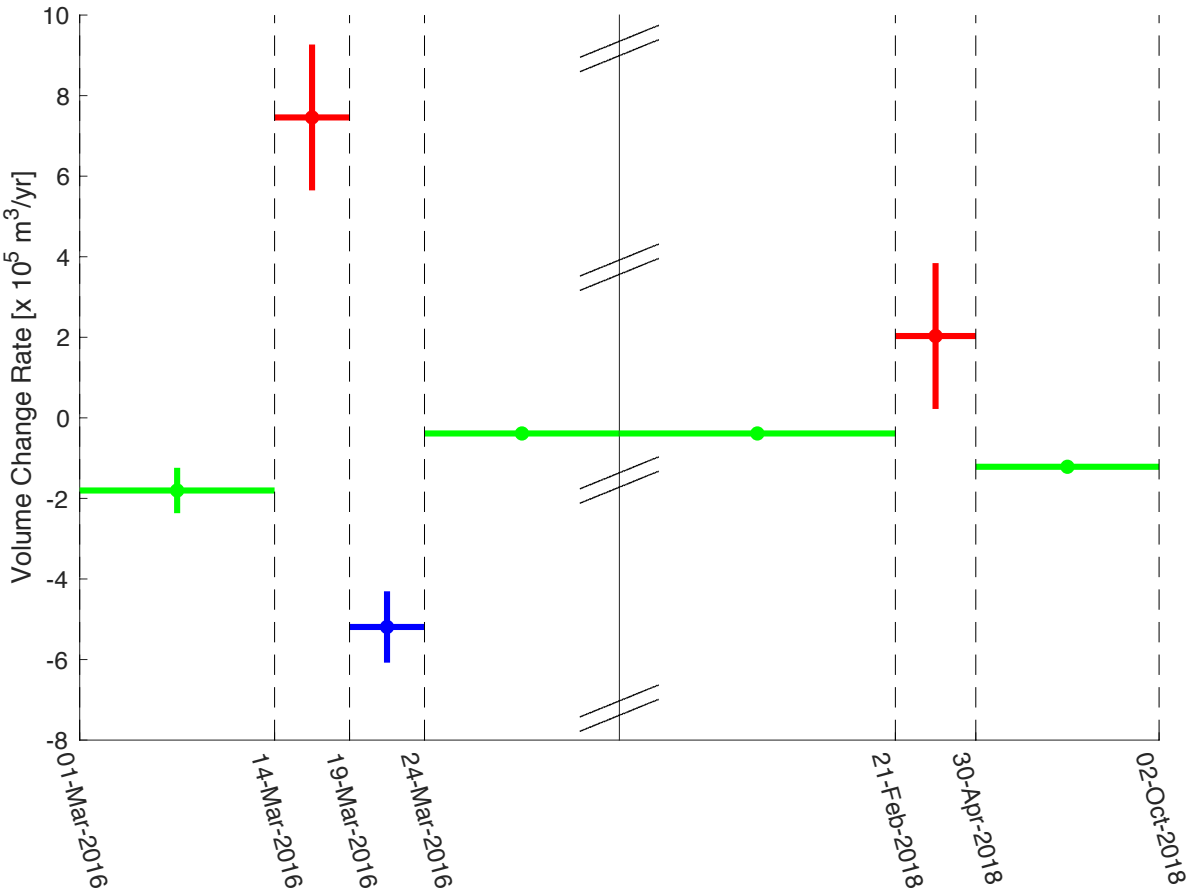

Figure 2.9: Estimated rates of volume change from the start of the March 2016 deployment period to 2018 October 2 after temporal adjustment of InSAR and GPS data using a piecewise-linear parameterization with breaks at the start/end of each deployment stage and the 2018 shutdown. Rate estimates are shown as dots with vertical and horizontal bars denoting the uncertainty and duration of the stage, respectively. Dashed black lines denote breaks in the parameterization. Normal operations stages are shown in green. Red denotes when the site was shut down (Stage 2 and the 2018 shutdown). Stage 3, when there was increased infield injection and pulsing, is shown in blue. The solid black line denotes a break in the time axis.

3 Geodetic Measurements and Numerical Models of Deformation at Coso Geothermal Field, California, USA, 2004-2016

Portions of this work are to be submitted to *Remote Sensing of Environment* in Fall 2019 with the following author list: Elena C. Reinisch, S. Tabrez Ali, Michael Cardiff, J. Ole Kaven, and Kurt L. Feigl.

Abstract

We measure transient deformation at Coso geothermal field using interferometric synthetic aperture data acquired between 2004 and 2016 and relative position estimated from Global Positioning System (GPS) to quantify relationships between deformation, pumping, and seismicity. We parameterize the reservoir as a cuboidal sink and solve for best-fitting reservoir dimensions and location before and after 2010. Time-series analysis is performed on resulting volume change estimates from individual interferometric and GPS pairs. We find changes in subsidence rate, reservoir contraction, and estimated sink depth after 2010, which we attribute to changes in injection protocol corresponding to sustainability efforts implemented in late 2009.

3.1 Introduction

The Coso geothermal field, located near China Lake, California, is the third largest geothermal field in the United States with an installed capacity to generate $\sim$270 MW of electrical power. It lies within an extensional step-over between dextral faults that hosts an actively developing metamorphic core complex (Unruh et al., 2002; Monastero et al., 2005). Directly beneath the field lies a partially molten magma body, located below the relatively shallow ($\sim$5 km depth) brittle-ductile transition, which heats water migrating deep into the geothermal area following

precipitation in the Sierra Nevada mountain range (Fournier et al., 1980). The buoyant hot water eventually rises via faults and fractures associated with the transtensional tectonics of the region into the reservoir comprised of highly fractured plutonic and metamorphic rocks of Mesozoic age (Monastero et al., 2005; Davatzes & Hickman, 2010). Fluid temperatures within the reservoir reach $\sim 350^{\circ}$ C at the relatively shallow depths of ~ 3 km tapped by more than 80 production wells (Figure 3.1). Following generation of electricity and condensation, the fluids are reinjected via more than 30 injection wells around the field. The average rates of (fluid) production and reinjection between 2004 and 2016 have been $(24.30 \pm 0.27) \times 10^8$ kg/month (924 ± 10 kg/s) and $(11.72 \pm 0.02) \times 10^8$ kg/month (446 ± 7 kg/s), respectively, which, neglecting natural recharge, corresponds to a net extraction rate of $\sim 12.58 \times 10^8$ kg/month (478 kg/s) (Division of Oil, Gas, and Geothermal Resources, 2016). In late 2009, the reservoir operators of the Coso Geothermal Plant implemented the Hay Ranch Water Project, which uses a ~ 15-km pipeline to recharge the existing reservoir at Coso with supplemental water, thereby increasing geothermal energy production (e.g., TEAM Engineering & Management, Inc., 2018; OpenEI, 2015).

Coso geothermal field is well known for being one of the most seismically active regions in California. Previous studies at Coso have linked such seismicity to the motion of fluids within the geothermal system and changes in local tectonic stress (e.g., Fialko & Simons, 2000; Bhattacharyya & Lees, 2002; Kaven et al., 2011, 2012, 2013; Schoenball et al., 2016). Geodetic studies have also noted that the area of observed subsidence corresponds with the production region near the Coso geothermal plant (e.g., Fialko & Simons, 2000), leading to the suggestion that geothermal fluids are driving both the deformation and seismicity at the site.

Similar phenomena have been observed at other geothermal fields, as recently reviewed by Majer et al. (2007), Brodsky & Lajoie (2013), and Ellsworth (2013). One example is Brady Hot Springs, a geothermal field in Nevada. Here, Cardiff et al. (2017) find evidence relating increased microseismic activity to periods of brief cessations in pumping at the site. Such behav-

ior is explained by the adaptation of subsurface effective stress to long-term normal operations, such that "extraction of fluids inhibits fault slip by increasing the effective stress on faults; in contrast, brief pumping cessations represent times when effective stress is decreased below its long-term average, increasing the likelihood of microseismicity" (Cardiff et al., 2017).

In this study, we further explore the associations amongst pumping, seismicity, and deformation at Coso to examine the strength of their relationships as well as identify geophysical mechanisms that could explain such relationships. We use an updated seismic catalog, pumping records from the site, as well as interferometric synthetic aperture radar (InSAR) and Global Positioning System (GPS) data spanning from 2004 to 2016.

3.2 Data

3.2.1 InSAR

We analyze 38 synthetic aperture radar (SAR) images acquired between 2004 and 2016 over Coso. Of these, 34 SAR images were acquired in ascending track 349 between 2004 and 2010 by the C-band ASAR sensor aboard the Envisat satellite (McLeod et al., 1998). An additional 4 SAR images were acquired after 2014 in ascending track 64 by the C-band sensor aboard the Sentinel-1A satellite (Geudtner et al., 2014). We use the images to create 91 interferometric pairs using an open-source InSAR processing software (GMTSAR), which utilizes Generic Mapping Tools (GMT) to create and visualize interferometric pairs (Sandwell et al., 2011a,b). The topographic contribution in the interferograms is removed using a digital elevation model with 1 arc-second posting from the Shuttle Radar Topographic Mission (Farr et al., 2007). Unwrapping is performed using the "statistical-cost, network-flow phase-unwrapping algorithm" (Snaphu) developed by Chen & Zebker (2000) to calculate the range change rate $\dot{\rho}$ in millimeters per year. Subsidence (positive range change) as rapid as $\sim$30 mm/year is observed over a circular area some 3 km in radius centered on the production wells (Figure 3.1). This signature

is consistently observed in all interferometric pairs spanning the production interval between 2004 and 2016, as shown in Figure 3.2. The rate and spatial extent of the deformation field are broadly consistent with InSAR data spanning 1993 to 1999 (Fialko & Simons, 2000).

The pairs from ENVISAT are selected using a minimum spanning tree (MST) algorithm according to orbital separation (e.g., Reinisch et al., 2017). The same data set was used in a previous deformation modeling study at Coso (Ali et al., 2016b). To summarize individual interferometric pairs, we consider the field of unwrapped range change rate $\dot{\rho}(E, N)$. The mean rate between 2005 and 2010 is derived by averaging range change rates from our 81 ENVISAT pairs (Figure 3.1), where E and N are the position coordinates easting and northing, respectively in a Universal Transverse Mercator (UTM) projection (Snyder, 1987). The k^{th} pixel of the mean rate field $\bar{\dot{\rho}}_k(E, N)$ is computed as

$$\bar{\dot{\rho}}_k(E, N) = \frac{1}{n_k} \sum_{i=1}^{n_k} \dot{\rho}_i(E, N) \tag{3.1}$$

We use the same averaging procedure to form a second stack, spanning 2014 to 2016, from the 10 pairs in the Sentinel-1A data set.

3.2.2 GPS

Data from continuous GPS station COSO provides daily estimates of the three components (eastward, northward, and upward) of relative position. The station is a part of the Southern California Integrated GPS Network and is located within 5 km of the center of the identified subsidence bowl. The GPS time-series data have been analyzed using methods outlined in Herring et al. (2016) and are publicly available (Hudnut et al., 2006). The time series has also been analyzed according to procedures outlined in Blewitt et al. (2018); this time series is publicly available as well (Blewitt, 2018b).

Data are also available from campaign GPS station COSJ, located to the northwest of the deforming region. This station is a part of the MAGNET network with publicly available time

series of relative position that have been analyzed using standard procedures outlined in Blewitt et al. (2018) (Blewitt, 2018a).

We use a subset of the time series from station COSO that spans from 2004 to 2015 to analyze deformation within the deforming region. We use data from COSJ to estimate far-field deformation. We work with GPS estimates analyzed according to Blewitt et al. (2018) when comparing displacement between COSO and COSJ in order to maintain consistency.

3.2.3 Accuracy

We analyze the accuracy of unwrapped InSAR range change rates by comparison to GPS measurements. Starting with our ENVISAT pairs, we first convert the GPS estimates of vector displacement $\mathbf{u}$ from both stations to range change $\Delta\rho$ by taking the negative scalar product with the unit vector $\hat{\mathbf{s}}^{(ENVI)} = [0.35; 0.08; -0.93]$ pointing from the pixel on the ground to the radar sensor aboard the satellite.

$$\Delta\rho^{(GPS)} = -\hat{\mathbf{s}}^{(ENVI)} \cdot \mathbf{u}^{(GPS)} \tag{3.2}$$

We then linearly interpolate and extrapolate $\Delta\rho^{(GPS,COSO)}$ and $\Delta\rho^{(GPS,COSJ)}$ in time to find estimates corresponding to the start and end dates of the ENVISAT pairs. The GPS range change values at individual points in time are then converted to pairs by first taking the difference between range change estimates from COSO and COSJ to remove the far-field deformation and then by time corresponding to the time intervals of the ENVISAT pairs. The uncertainty for the range change estimated from GPS is derived from measurement uncertainty at each station. Differenced range changes are then converted to range change rates after dividing by the time interval for each pair. We find an estimated range change rate of 3.8 mm/yr at COSO with respect to COSJ. We then difference the InSAR range change measurements for pixels corresponding to COSO with measurements for pixels corresponding to COSJ from the ENVISAT pairs. We use the standard error of the mean as an estimate of uncertainty for the

range changes observed using InSAR. The mean range change rate at COSO with respect to COSJ as measured by ENVISAT is 5.8 ± 10.7 mm/yr. We compare the difference between the GPS and InSAR data sets for unwrapped range change rates estimated at COSO with far-field deformation effects removed using a Student's one-sample T test (e.g. Wackerly et al., 2007). We test the null hypothesis that the means of the two data sets are equal. We find $T_{calc} = -1.3$, which is less in absolute value than the critical value $T_{\alpha/2,\nu=80} = 2.0$. Thus, we conclude (with 95% confidence) that there is no significant difference between mean range change rate estimated from GPS and measured by ENVISAT.

We perform the same procedure for our Sentinel-1A (S1A) pairs. In this case, we use the Sentinel-1A unit pointing vector $\hat{\mathbf{s}}^{(S1A)} = [0.63; 0.11; -0.77]$ to derive the corresponding range change rates from GPS. The estimated range change rate at COSO with respect to COSJ from GPS over the 2014-2016 time frame is 4.6 mm/year. The mean range change rate at COSO with respect to COSJ as measured by Sentinel-1A is 3.3 ± 2.2 mm/yr. Repeating the same test at 95% confidence, we find $T_{calc} = 2.1$ to be less than the critical value $T_{\alpha/2,\nu=9} = 2.3$. Thus, we conclude that there is no significant difference between range change rate estimated from GPS and measured by Sentinel-1A.

Figures 3.3 and 3.4 show histograms of the difference in range change rates between GPS and individual InSAR pairs for both the ENVISAT and Sentinel-1A data sets.

3.2.4 Seismic Catalog

Local and regional seismicity near the Coso geothermal field is recorded by a local borehole seismic network and analyzed by the Navy Geothermal Program Office. Kaven et al. (2012) refined the initial event locations by estimating a best fitting one-dimensional velocity model and relocating all events. Resulting event hypocenters are found to have location uncertainties on the order of 300 m horizontally and 600 m vertically. We analyze a subset of this catalog that includes events that occurred in the time interval between 2005 and 2015 (Figures 3.5

and 3.6). The average values of seismic velocities in this region are 5.8 and 3.5 km/s for V_p and V_s, respectively. The average Poisson's ratio is thus $\nu = 0.21$. Given the average V_p, we estimate the density of the surrounding material to be about 2.6 g/cm^3 (Lindseth, 1979). This is consistent with other density estimates at Coso (e.g., Feighner & Goldstein, 1990; Monastero et al., 2005). To analyze the seismicity associated with the geothermal reservoir, we select only those events with hypocenters located within the ellipsoidal volume modeled as a sink that fits the ENVISAT stack (Ali et al., 2016b). A Gutenberg-Richter plot of the relationship between number of events and magnitude indicates that this subset of the catalog is complete to magnitude 0 (Figure 3.7).

3.2.5 Pumping Records

Pumping records for the monthly rates of gross injection and gross production in kilograms per month for the Coso geothermal power plant from 2005 to 2016 (Figure 3.8) have been published by the Division of Oil, Gas, and Geothermal Resources (2016).

3.3 Methods

3.3.1 Estimating Volume Change of the Reservoir

A previous modeling study by Ali et al. (2016b) uses a poroelastic, homogeneous model to describe the deformation at Coso. Their 2-dimensional, axisymmetric numerical model consists of a confined reservoir embedded within impermeable host rock with a domain that is 100 km long (X-axis) and 50 km deep (Z-axis). A single well at the center of the reservoir is used to withdraw the fluid at a rate corresponding to an annual pressure drop of 0.33 MPa/yr. They assume a Biot coefficient of unity, a porosity of 5%, a uniform permeability of $k = 10^{-14}$ m^2, a Poisson's ratio of 0.25, and a static Young's modulus of 25 GPa for the entire domain, including the reservoir. A pressure boundary condition for the maximum possible pressure drop of

0.33 MPa/yr, corresponding to a drop in hydraulic head of 33 m/yr is imposed at a single node in the center of the reservoir. Using the finite element code DEFMOD (Ali, 2014; Meng, 2017) and the stack of ENVISAT pairs, they solve the coupled deformation-diffusion equation (e.g. Zheng et al., 2003, eq. 5 and 8) to estimate the dimensions of the reservoir. Their best-fitting results are shown in Figure 3.9 and Table 3.1. We use these 2-dimensional results as a guide for subsequent 3-dimensional modeling.

To arrive at refined estimates of dimensional properties and volume change of the reservoir in this study, we model the deformation in each of the 91 interferometric pairs using a "cuboid" parameterization to include a single sink at a given depth in an elastic half space with uniform material properties (Okada, 1985). In this model, the cuboid represents a volume element with sides of width W, length L, and height H, with an initial volume of $V_0 = LWH$. The cuboid is sliced into eight equal-sized octants by three rectangular patches that are mutually orthogonal. Each rectangular patch is a dislocation with a negative value of tensile opening. The slip u_i on a singular patch is proportional to the ratio of its area to the total volume change:

$$\Delta V = u_x LH + u_y WH + u_z LW. \tag{3.3}$$

The model parameters, including the source location, volume change, cuboid dimensions, and InSAR-related nuisance parameters (e.g. Feigl & Thurber, 2009; Reinisch et al., 2018), along with their uncertainties, are estimated using simulated annealing methods employed by the General Inversion of Phase Technique (GIPhT) (Feigl & Thurber, 2009; Ali et al., 2014).

The temporal distribution of our InSAR data set divides our deformation modeling into two distinct time intervals: 2004 to mid-2010 (corresponding to ENVISAT pairs), and 2014 to 2016 (corresponding to Sentinel-1A pairs). Working with the same stack of ENVISAT pairs as Ali et al. (2016b), we estimate all the model parameters starting with initial estimates based on the best-fitting results from Ali et al. (2016b) (Table 3.1). We assume the Poisson's ratio to be $\nu = 0.21$, consistent with the average values of seismic velocities used to locate the

seismicity (Kaven et al., 2013). We then take the best-fitting estimates for the sink location and cuboid dimensions found from the stack inversion to be fixed and estimate individual volume change for each of our 81 ENVISAT interferometric pairs. We repeat the same procedure for the Sentinel-1A pairs using their corresponding stack.

3.3.2 Time-Series

To analyze the trend of the deformation over time, we perform time-series analysis using temporal adjustment on the set of volume changes $\Delta V_{i,j}$ estimated from the individual InSAR pairs spanning the time intervals from t_i to t_j. This procedure converts the pair-wise volume changes $\Delta V_{i,j}$ for individual interferometric pairs into a cumulative value of volume change at each point t_i and t_j in time (Reinisch et al., 2017). As described previously, this approach implicitly assumes that the temporal dependence and spatial dependence of the deformation field are separable functions (Feigl & Thurber, 2009; Reinisch et al., 2017). Accordingly, we write the vector displacement field $\mathbf{u}$ as

$$u(t, x) = f(t)G(x) \tag{3.4}$$

Where $f(t)$ is a function of time t only and $G(x)$ is a function of spatial position coordinate x only. In our case we consider $G(x)$ to be the model of a cuboidal sink contracting in a half space with uniform elastic properties. For the temporal function, we consider several possibilities, including constant rate during the time interval between 2004 and 2010:

$$f_1(t_i) = a_1(t_i – t_0) \tag{3.5}$$

where the initial time $t_0 = 2003.87$ is the start date of our data set in decimal years, and constant rate during the time interval between 2010 and 2016:

$$f_2(t_i) = a_2(t_i – t_1) \tag{3.6}$$

where the time $t_1 = 2010$ refers to the date when pumping operations were altered at Coso (e.g., TEAM Engineering & Management, Inc., 2018; OpenEI, 2015; Eneva et al., 2018). To model the full data set, we use a piecewise-linear parameterization with m breaks at times t_m that form $(m-1)$ segments:

$$\begin{aligned} &f_3(t_i) = \Sigma_{j=1}^{j=m} a_j D(t_i), \text{ where} \\ &D(t_i) = \begin{cases} 0 & \text{if } t_i < t_j \\ (t_i - t_j) & \text{if } t_j \leq t_i < t_{j+1} \\ (t_{j+1} - t_j) & \text{if } t_i \geq t_{j+1}. \end{cases} \end{aligned} \tag{3.7}$$

We use this function with $m = 2$, $m = 4$, and $m = 12$. We also consider an exponentially decaying rate parameterization

$$f_4(t_i) = a_e \left(1 - exp\left(-\frac{t_i - t_0}{\tau}\right)\right) \tag{3.8}$$

where τ is a characteristic time scale found through nonlinear optimization.

To increase data coverage, we also analyze the volume change in the temporal dimension using displacement data from GPS. We difference each daily record of relative position in our data set with the previous day's record, resulting in 3,650 measurements of differential position, i.e. displacement. We then convert these displacements to range change using Equation (3.2) and divide by the time interval $\Delta t = t_j – t_i$ of the paired values to arrive at the range change rate $\dot{\rho}$. We estimate the volume change and reservoir depth in a similar manner to the InSAR data

set by taking the best-fitting estimates for the source location and cuboid dimensions found from the stack inversion to be fixed. We then perform a similar time-series analysis on the resulting volume change rates to that of the InSAR data using temporal adjustment.

3.4 Results

3.4.1 Deformation Modeling

The results from applying the "cuboid" parameterization to mean range change rates from both the ENVISAT and Sentinel-1A stacks are shown in Figures 3.10 and 3.11 as well as Tables 3.2 and 3.3, respectively. We find an estimated depth of reservoir to be 2.4 km for the time period covering 2004 to 2011, consistent with the results from Ali et al. (2016b), while the estimated depth of the reservoir from 2014 to 2016 is 3.1 km. We calculate the dimensionless misfit $\chi = 1.7$ of the model to the ENVISAT data as the square root of the reduced χ^2-test statistic (Strang & Borre, 1997, p. 334). Similarly, we find the misfit of the model to the Sentinel-1A stack to be $\chi = 1.2$.

We similarly estimate the reservoir depth before and after 2010 using the GPS data and source location estimates from the InSAR stacks. We find that the best-fitting estimated reservoir depth for observations before 2010 is (2.6 ± 0.5) km, whereas the best-fitting estimated reservoir depth for observations after 2010 is (3.1 ± 0.6) km. For these solutions, the misfit χ is 1.4 and 1.6, respectively.

3.4.2 Time-Series Analysis

We start by parameterizing the volume change estimates before and after 2010 by separate, single-rate temporal functions corresponding to when well operations were varied at the site (e.g., TEAM Engineering & Management, Inc., 2018; OpenEI, 2015; Eneva et al., 2018). Due to a lack of data between 2011 and 2014, we also include a break at the end of the ENVISAT

data set (September 3, 2010). Interferometric pairs included in the analysis are shown in Figure 3.12. For the InSAR data, we parameterize all the ENVISAT estimates between 2004 and 2010 using a single rate, and then similarly parameterize all the Sentinel-1A estimates between 2014 and 2016 using a single rate function. We cannot estimate any volume change for the time between 2011 and 2014, when we have no InSAR coverage. The results for this parameterization (equation (3.7), $m = 4$) are shown in Figure 3.13. We calculate the dimensionless misfit to be $\chi = 0.5$. We perform a two-tailed Student's T test to test the null hypothesis that these two estimated rates are equal (e.g., Wackerly et al., 2007). We find a significant difference between the estimated rate before 2010 and the estimated rate after 2014 with 95% confidence (Table 3.4).

We also use a piecewise-linear temporal function with breaks on June 1st and December 1st of each year from 2005 to 2010 (equation (3.7), $m = 12$) to further examine if any seasonal trends we see in the pumping records (Figure 3.8) are reflected in the InSAR data before changes in well operations. We perform an F test for model complexity to decide whether the increased complexity of the piecewise-linear model is justified (e.g., Wackerly et al., 2007, pp. 536 and 627). We test the null hypothesis that the single rate parameterization and the piecewise-linear parameterization fit the data equally well at 95% confidence. We find $F_{calc} = 0.94$, which is less than the critical value $F_{\alpha=0.05} = 1.43$ with degrees of freedom $df_1 = 90$ and $df_2 = 79$. We conclude that the complexity of the piecewise-linear model is not justified with 95% confidence and continue with the single rate parameterization.

We use the same single-rate temporal functions for analyzing volume change estimated from GPS, treating the data before 2010 and after 2010 separately, as shown in Figure 3.14 (equations (3.5) and (3.6)). We calculate the dimensionless misfit for the pre-2010 interval to be $\chi = 2.3$. The dimensionless misfit for the post-2010 interval is $\chi = 1.5$. We perform a two-tailed Student's T test to test the null hypothesis that the rates in the two intervals are equal (e.g., Wackerly et al., 2007, p. 524). The null hypothesis is rejected with 95% confidence

(Table 3.5) We find that the rate for the post-2010 interval is significantly smaller (slower) than the pre-2010 rate.

We summarize these results in Figures 3.15 and 3.16. Table 3.6 compares several estimates of the subsurface volume change rate $\dot{V}$. Rates are derived from pumping records using a range for production brine density of $\rho_{prod} \in [990, 1250]$ kg/m^3. Injection brine density is calculated using the thermal expansion coefficient for water, a production temperature of 350 C$^\circ$, and an injection temperature of 160 C$^\circ$ (Rose, 2013). Results shown in Table 3.6 assume a density of 1000 kg/m^3 for the produced brine and 1043 kg/m^3 for the injected brine. Net production is calculated as the difference between rates derived from gross injection and gross production.

3.4.3 Correlation Tests

We quantify the relationship between seismicity, pumping, and deformation by performing correlation tests on the values plotted in Figures 3.15 and 3.16. We first test the correlation between deformation and gross production rate. Using the modeled values of volume change derived from temporal adjustment (shown in Figures 3.15c and 3.16c), we estimate the volume change at the start of each month and compare it to the monthly gross production rate (shown in Figures 3.15b and 3.16b). We normalize the values using a statistical Z-transform, defined as

$$\hat{\mathbf{x}} = \frac{\mathbf{x} - \bar{\mathbf{x}}}{\sigma_x} \tag{3.9}$$

(e.g., Wackerly et al., 2007, p. 181). The results are summarized in Figure 3.17. We first consider the monotonic relationship between volume change and gross production rate using Spearman's test (e.g., Wackerly et al., 2007, p. 786). We find a Spearman's correlation coefficient $r_s = 0.75$ with a corresponding p-value of $p = 2.14 \times 10^{-16}$, suggesting a strong monotonic relationship between volume change and gross production. We further explore the linearity of this relationship using Pearson's test. We find a high correlation between the volume change and gross production rate, with a (Pearson's) correlation coefficient of $R = 0.75$

(e.g., Wackerly et al., 2007, p. 599). We test the null hypothesis of no correlation against the alternative of non-zero correlation using a Student's T test (e.g., Wackerly et al., 2007, p. 599). We find a p-value of $p = 2.2 \times 10^{-16}$, indicating the probability of rejecting the null hypothesis of no correlation when it is actually true. Thus, we conclude that the positive correlation between the volume change each month and gross production rate is significant. Consequently, this result supports our hypothesis that deformation is causally associated with pumping at Coso. Performing the same tests with the rates of gross injection and net production yields p-values of 5.3×10^{-7} and 8.0×10^{-7}, respectively.

We also test the correlation between the seismicity rate (number of seismic events per month, shown in Figures 3.15a and 3.16a) and monthly pumping rate in terms of gross injection, gross production, and net production (shown in Figures 3.8, 3.15b, and 3.16b). We consider both a monotonic relationship and a specifically linear relationship. The results are summarized in Table 3.7 and Figure 3.18. We see that the rate of seismicity is most highly correlated with the gross production rate. The combination of the Spearman and Pearson tests show a strong monotonic relationship, which may be further described as linear, between the rates of seismicity and gross production. We do not see this same confidence when comparing seismicity to gross injection. Both correlation tests reject (with p-values less than 10^{-8}) the null hypothesis that there is no correlation between seismicity and gross production rates. We conclude that the positive correlation between number of seismic events per month and monthly gross production rates is significant.

3.4.4 Identifying a Driving Mechanism for the Observed Subsidence

We convert our estimates of volume change from modeling the interferometric pairs with a "cuboid" parameterization to volumetric strain rates by dividing by the initial volume V_0 of the single cuboid and the time span Δt. The modeling results indicate that the cuboidal sink is shrinking with an average volumetric strain rate of $\bar{\dot{\epsilon}} = \bar{\Delta V}/(V_0 \Delta t)$ of the order of 90

microstrain/year or 3 picostrain/second in absolute value. Next, we consider two possible mechanisms: (1) thermal contraction of the rock matrix and (2) decreasing pore-fluid pressure. Accordingly, we interpret our estimates of volumetric strain derived from our estimates of volume change as a result of temperature change and/or pressure change. Considering a decrease in pore fluid pressure as the cause of volume change, the observed volume change rate $\dot{V}$ in the cuboidal reservoir is related to a pressure change rate $\dot{P}$ [Pa/yr] by:

$$\dot{V}^{(P)} = (c_m \dot{P}) V_0 \tag{3.10}$$

$$= \dot{\epsilon}^{(P)} V_0, \tag{3.11}$$

where c_m [Pa^{-1}] is Geertsma's uniaxial expansion coefficient, which is a coefficient analogous to the poroelastic expansion coefficient $1/H$ but used in the case of a uniaxially constrained body (Wang, 2000). The term $\dot{\epsilon}^{(P)}$ [yr^{-1}] is a poroelastic volumetric strain rate.

Alternatively, if we consider the volume change to be caused by thermal contraction, then the estimated rate of volume change rate in the cuboid is related to a temperature change rate $\dot{T}$ [K/yr] by

$$\dot{V}^{(T)} = (\alpha_T \dot{T}) V_0 \tag{3.12}$$

$$= \dot{\epsilon}^{(T)} V_0 \tag{3.13}$$

where α_T [K^{-1}] is the thermal expansion coefficient and $\dot{\epsilon}^{(T)}$ [yr^{-1}] is a thermal volumetric strain rate.

We can also consider a combination of these two processes through a linear combination of Equation (3.11) and Equation (3.13).

Following the procedure in Reinisch et al. (2018), we define *a priori* confidence intervals for reasonable values of strain rate under each interpretation. Using results from well logs (Blankenship, 2016), we define mean values for the rates of change in pressure $\dot{P}$ and temper-

ature $\dot{T}$ with confidence intervals defined such that a rate of zero is two standard deviations away from the mean value.

$$\dot{P} \in (-9.4 \pm 4.7) \times 10^5 \text{ Pa/yr} \tag{3.14}$$

$$\dot{T} \in (-2.6 \pm 1.3) \text{ K/yr} \tag{3.15}$$

We similarly define confidence intervals for $\alpha_T \in (1.0 \pm 0.5) \times 10^{-5}$ 1/K and $c_m \in (5.0 \pm 2.5) \times 10^{-10}$ 1/Pa (e.g., Mossop & Segall, 1997, 1999; Fialko & Simons, 2000; Wang, 2000; Nygren, 2005; Rutqvist et al., 2015; Ali et al., 2016b). This leads to confidence intervals for volumetric strain rate interpreted in terms of decreasing pore-fluid pressure alone, thermal contraction alone, or a combination of thermal contraction and decreasing pore-fluid pressure:

$$\dot{\epsilon}^{(P)} \in (-5.6 \pm 4.2) \times 10^{-5} \text{ yr}^{-1} \tag{3.16}$$

$$\dot{\epsilon}^{(T)} \in (-2.6 \pm 2.0) \times 10^{-5} \text{ yr}^{-1} \tag{3.17}$$

$$\dot{\epsilon}^{(P+T)} \in (-8.2 \pm 4.6) \times 10^{-5} \text{ yr}^{-1}. \tag{3.18}$$

We then compare the realized *a posteriori* 68% confidence interval for our estimates to the *a priori* 68% confidence intervals defined in Equation 3.16 to determine if any of the interpretations are unreasonable. Figure 3.19 shows the resulting comparisons for ENVISAT and Sentinel-1A pairs. In each case, we see no overlap between the realized 68% confidence interval for the volumetric strain rates and the 68% confidence interval for reasonable values of $\dot{\epsilon}^{(T)}$ defined *a priori*. We infer that the estimated values of volumetric strain rates are too high to be attributed to thermal contraction of the rock matrix alone. In contrast, we see clear overlap between the realized 68% confidence interval for volumetric strain rates and the 68% confidence interval for reasonable values of $\dot{\epsilon}^{(P)}$ and $\dot{\epsilon}^{(P+T)}$ defined *a priori*, with the most apparent overlap with the $\dot{\epsilon}^{(P)}$ interpretation. We conclude that decreasing pore-fluid pressure is the dominant driving mechanism causing the subsidence observed at Coso.

3.5 Discussion

For observations before 2010, we find the best-fitting cuboidal model for the reservoir to have a centroid depth of 2418 ± 531 m, consistent with previous studies (e.g., Ali et al., 2016b; Eneva et al., 2018). The results using the Sentinel-1A stack for the time interval between 2014 and 2016, however, show that the best-fitting depth for the reservoir between 2014 and 2016 is 3099 ± 195 m. The reservoir depths estimated from GPS data during both the pre-2010 and post-2010 intervals are similar to the results estimated from InSAR data.

We find that the volumetric strain is most reasonably attributed to decreasing pore-fluid pressure during both time intervals.

We find an overall positive correlation between the number of seismic events per month and monthly gross production and net production rates. However, closer examination of Figure 3.15 suggests a seasonal trend during the months of May and June when the net production rates are decreased and then increased by the plant. We see that the number of seismic events tends to increase during this temporary decrease in net pumping rate operations before 2010. Similar behavior has been explained at Brady Hot Springs by the adaptation of subsurface effective stress to long-term normal operations (Cardiff et al., 2017). To determine if the same mechanism could be occurring at Coso, we evaluate the correlation between monthly seismicity rates and monthly rates of both gross and net production before and after the start of 2010 (Figure 3.20). We see no apparent correlation between production rates and seismicity rates after the start of 2010. In contrast, when limiting the data set to before 2010, we discern a negative linear correlation between seismicity rates and net production rates, with a Pearson's correlation coefficient of $R = -0.65$ and p-value of $p = 2.0 \times 10^{-8}$.

A sustainability effort, termed the Hay Ranch Water Project, was implemented in late 2009 to recharge the existing reservoir at Coso with supplemental water (e.g., TEAM Engineering & Management, Inc., 2018; OpenEI, 2015). With this development in mind, we suggest that

before the implementation of the recharge pipeline, the effective stress conditions at Coso had adapted to long-term normal operations. Subsequently, recharging the reservoir may have altered this behavior, thus decreasing the effect of changes in pumping rate on seismic activity.

The results from the geodetic modeling suggest that the depth to the center of the reservoir increased after 2010. A change in reservoir depth could be explained by reservoir depletion after 2010, when the pumping rate was increased (e.g., Eneva et al., 2018). If the fluid level in the reservoir drops, then faults that were previously saturated by fluids within the reservoir would no longer be filled with such pressurized fluids. This Coulomb effect would explain the correlation between monthly seismicity rates and pumping rates before 2010 and the lack of correlation thereafter. An increase in reservoir depth after 2010 could also explain the decrease in maximum deformation rates observed by InSAR after 2010 (e.g., Sentinel-1A pairs), as shown in Figure 3.2 and found in previous studies (e.g., Eneva et al., 2018). The magnitude of displacement at the surface decreases as the depth of the sink increases (e.g., Okada, 1985).

We also find a significant difference between volume change rates estimated before 2010, between 2010 and 2011, and after 2014 from our InSAR data set. The previous reasoning explains the decrease in estimated volume change rate between pairs before 2011 and pairs after 2014. The significant increase in the first 6 months following completion of the Hay Ranch project could be explained by the increased pumping activity at the site, as suggested by Eneva et al. (2018, their Figure 4) and apparent in Figure 3.8. The strong correlation between the amount of volume change and pumping rates (Figure 3.17) corroborates such an explanation.

Comparing the volume change rates in Table 3.6, we find that the estimates of volume change rate of the reservoir from deformation modeling are an order of magnitude less than those predicted through standard density calculations using the pumping records. Under the simple assumptions of a nearly incompressible fluid in a poroelastic half space, Segall (1985) interprets Skempton's coefficient B as the "ratio of solid volume change to change in pore fluid volume.... Thus, for example, if water is uniformly withdrawn from a rock with $B = 0.8$

the volumetric contraction of the rock is 80% of the volume of the extracted water." Deng et al. (2016) give the range of Skempton's coefficient for crustal rock to be between 0.5 and 0.9. Given the metamorphic setting of Coso with basalt and rhyolites present (e.g., Monastero et al., 2005; OpenEI, 2015), values for B could fall below this range as well (e.g., Zencher et al., 2006). Considering the recharge to the system, a value of B around 0.65 would explain the discrepancy between volume change rate estimates in Table 3.6.

Eneva et al. (2018) have also suggested poroelastic effects to explain the subsidence at Coso. The model presented by Segall (1985) for depleting a reservoir at constant rate and source location has been used to describe changes in subsidence at other geothermal fields (e.g., Barbour et al., 2016). According to this model, if the rate of production (or net extraction) is constant, then the response in terms of subsidence would vary as a smooth function of time. To test this possibility, we perform temporal adjustment using a temporal function with exponentially decaying rate (equation (3.8)) with a characteristic time constant $\tau = 18$ yr found through nonlinear optimization. Our cuboidal models estimated from the InSAR and GPS data sets show different reservoir depths before and after 2010, which violate the model assumptions from Segall (1985). Instead, we use the differential (day-to-day) measurements of vertical displacement corresponding to the pairs in the GPS data set. We find a misfit of $\chi = 2.0$. For comparison, we perform temporal adjustment on the pair-wise vertical displacements using a piece-wise linear parameterization with a break on 2010 January 1 (equation (3.7), $m = 2$), after the well operations were altered. We find a misfit of $\chi = 1.8$, indicating a better fit than the smooth model corresponding to a reservoir depleting at constant rate. Again using an F-test, we reject the null hypothesis that the two models provide equally good fit with 95% confidence. We conclude that the changes in subsidence rate, reservoir contraction, and sink depth are due to the change in injection protocol in late 2009. Apparently, the geothermal system at Coso is too complex to be explained by a model of a simple sink with constant rate of depletion and constant location.

3.6 Conclusion

Using methods outlined previously (Reinisch et al., 2018), we have advanced the characterization of the subsidence observed by InSAR at Coso geothermal field by estimating the volume change rate for each interferometric pair using a "cuboid" parameterization. Using temporal adjustment, we find a significant difference between volume change rates estimated before and after 2010 with 95% confidence. We also identify decreasing pore-fluid pressure as the dominant mechanism driving the observed deformation. We confirm a significant positive correlation between deformation and production rate. We also confirm an overall positive correlation between seismicity rate and gross production rate. There is a negative correlation between seismicity rate and net production before 2010, suggesting that subsurface effective stress conditions at Coso had adapted to long-term normal operations at that time. However, we do not find the same correlation past 2010, which appears to be a result of sustainability efforts implemented at Coso in late 2009 and the subsequent increase in depth of the reservoir.

3.7 Acknowledgements

We thank Herb Wang, Martin Schoenball, Nick Davatzes, and Kelly Blake for helpful discussions. We also thank Chuck Wicks and Andy Barbour of the USGS and Mariana Eneva of Imageair Inc. for constructive comments. Several figures were created using the Generic Mapping Tools (Wessel et al., 2013).

Raw Synthetic Aperture Radar (SAR) data from the Envisat satellite mission operated by the European Space Agency (ESA) are copyrighted by ESA and were provided through the WInSAR consortium at the UNAVCO facility. Raw Synthetic Aperture Radar (SAR) data from the Sentinel-1A satellite mission operated by ESA were available free of charge through the Distributed Active Archive Center (DAAC) at the Alaska Satellite Facility (ASF) and through the Sentinels Scientific Data Hub. This material is based on data services provided by UN-

AVCO through the GAGE Facility with support from the National Science Foundation (NSF) and National Aeronautics and Space Administration (NASA) under NSF Cooperative Agreement No. EAR-1261833.

We gratefully acknowledge support from the Weeks family to the Department of Geoscience at the University of Wisconsin-Madison. This study was partially supported by grants from the National Science Foundation (EAR-1654649 and EAR-1347190). Elena C. Reinisch was supported by a National Science Foundation Graduate Research Fellowship (DGE-1256259) and an Advanced Opportunity Fellowship from the Graduate School at UW-Madison.

Table 3.1: Finite element modeling results from Ali et al. (2016b).

Parameter Name	Best-fitting Estimate	Uncertainty
Easting in m	428651.3	1000
Northing in m	3987538.4	1000
Reservoir Depth in m	2366.6	250
Reservoir half thickness in m	2053.1	250
Reservoir half length in m	3027.2	500
Young's Modulus in GPa	25	0
Poisson's Ratio	0.25	0
Pressure Change in MPa	-0.3	0

Table 3.2: Results from nonlinear inversion with a "cuboid" parameterization on the stack of MST Envisat pairs.

Parameter Name	Best-fitting Estimate	Uncertainty
Easting gradient $\delta\rho/\delta x$	6.78E-08	2.19E-07
Northing gradient $\delta\rho/\delta y$	-9.93E-09	1.86E-07
Upwards gradient $\delta\rho/\delta z$	-9.97E-07	9.67E-07
Offset in cycles	-0.5	0.8
Poisson ratio ν	0.21	0
Volume Change ΔV [m^3]	-2.02E+05	2.81E+04
Centroid Easting E in m	428580.4	531.3
Centroid Northing N in m	3987509.0	250.0
Centroid Depth in m	2418.2	531.3
Cuboid L in m	3.07E+03	3.23E+02
Cuboid W in m	2.28E+03	2.25E+02
Cuboid H in m	1.95E+03	2.42E+02

Table 3.3: Results from nonlinear inversion with a "cuboid" parameterization on the stack of Sentinel-1A pairs.

Parameter Name	Best-fitting Estimate	Uncertainty
Easting gradient $\delta\rho/\delta x$	1.64E-09	6.25E-08
Northing gradient $\delta\rho/\delta y$	-1.39E-07	9.38E-08
Upwards gradient $\delta\rho/\delta z$	6.73E-07	2.19E-06
Offset in cycles	-0.5	0.6
Poisson ratio ν	0.21	0
Volume Change ΔV [m^3]	-1.07E+06	2.25E+05
Centroid Easting E in m	428870.4	48.4
Centroid Northing N in m	3986482.0	46.9
Centroid Depth in m	3098.7	195.3
Cuboid L in m	3.12E+03	4.84E+01
Cuboid W in m	2.34E+03	4.84E+01
Cuboid H in m	1.93E+03	4.84E+01

Table 3.4: Results from two-tailed Student's T test with degrees of freedom df at the 95% confidence level (e.g., Wackerly et al., 2007, p. 524) for estimated volume change rates.
H_0: equal rates
H_1: rates differ

Start of break 1	Start of break 2	Rate 1 $\times 10^6$ [m^3/yr]	Rate 2 $\times 10^6$ [m^3/yr]	df	test value	critical value	result
20031114	20100101	(-1.2 ± 0.04)	(-1.3 ± 0.29)	78	3.95	1.99	reject H_0
20031114	20141102	(-1.2 ± 0.04)	(-0.80 ± 0.05)	76	-25.16	1.99	reject H_0
20100101	20141102	(-1.3 ± 0.29)	(-0.80 ± 0.05)	16	-4.67	2.12	reject H_0

Table 3.5: Results from two-tailed Student's T test with degrees of freedom df at the 95% confidence level (e.g., Wackerly et al., 2007, p. 524) for estimated volume change rates from geodetic data pre-2010 and post-2010.
H_0: no significant difference in rates
H_1: signficant difference in rates

Pre-2010 rate $\times 10^6$ m^3/yr	Post-2010 rate $\times 10^5$ m^3/yr	df	test value	critical value	result
(-1.2 ± 0.02)	(-8.10 ± 0.09)	3638	-843.22	1.96	reject H_0

Table 3.6: Estimates of subsurface volume change from multiple data sets.

data source	$\dot{V}$ [liter/s]
Gross injection (Division of Oil, Gas, and Geothermal Resources, 2016)	427 ± 105
Gross production (Division of Oil, Gas, and Geothermal Resources, 2016)	-924 ± 202
Net production (Division of Oil, Gas, and Geothermal Resources, 2016)	-497 ± 228
Cuboid sink estimated from InSAR data from 2005 to 2010	-38 ± 1
Cuboid sink from InSAR data from 2014 to 2016	-25 ± 2
Cuboid sink estimated from GPS data from 2005 to 2010	-38 ± 1
Cuboid sink from GPS data from 2014 to 2016	-26 ± 3
Average recharge (Spane Jr, 1978; Austin & Moore, 1987)	130

Table 3.7: Results from correlation tests between number of events per month and monthly pumping rates.

pumping category	Spearman's R_s	Spearman's p-value p	Pearson's R	Pearson's p-value p
gross injection	0.20	0.05	0.15	8.1×10^{-2}
gross production	0.68	2.6×10^{-19}	0.48	5.7×10^{-9}
net production	0.50	8.1×10^{-10}	0.36	2.8×10^{-5}

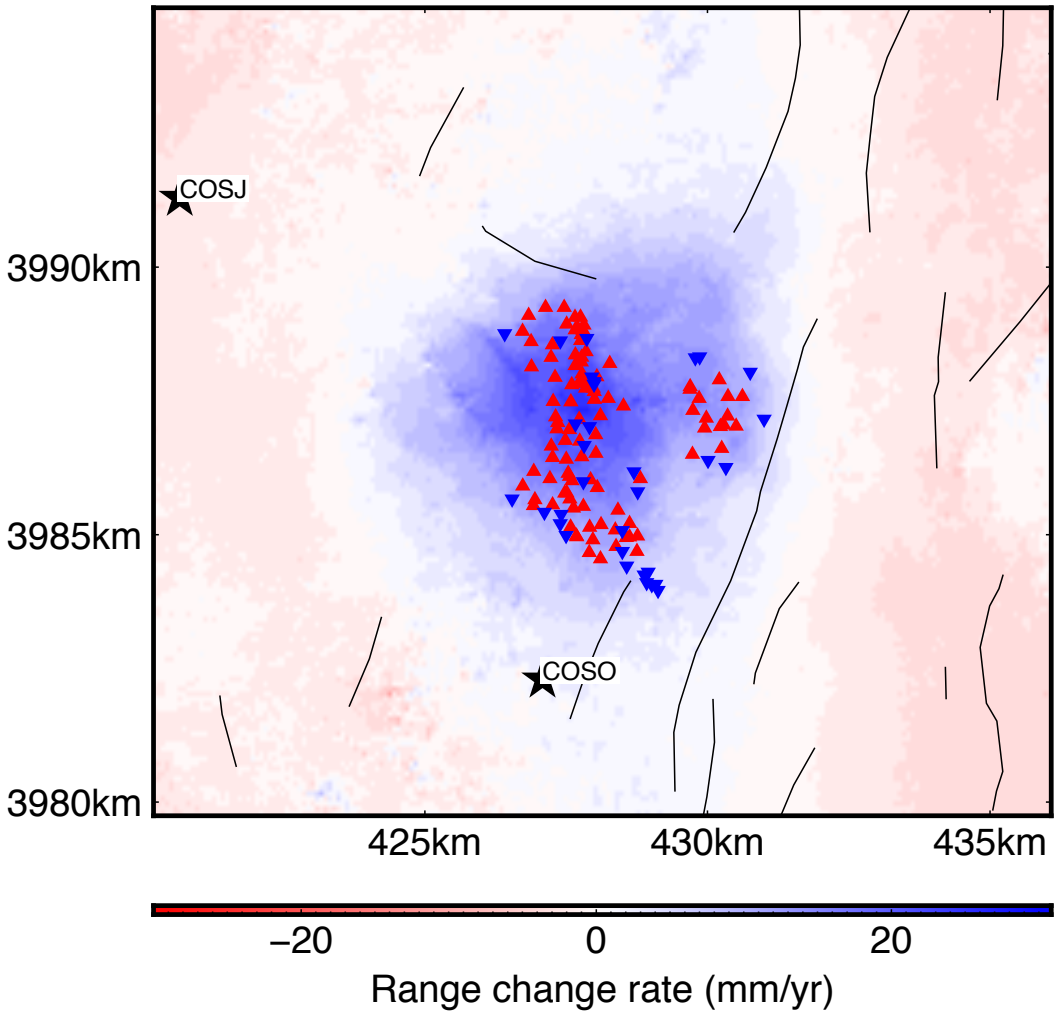

Figure 3.1: Interferogram showing the field of stacked unwrapped range change rate $\bar{\dot{\rho}}(E, N)$ from 81 ENVISAT pairs. The pairs span from 2004 to 2010 and are selected using a minimum spanning tree algorithm according to orbital separation. Production wells are shown as upright, red triangles and injection wells are shown as inverted, blue triangles. GPS stations are labeled and denoted with black stars. Coordinates are easting and northing [km] in Universal Transverse Mercator (UTM) projection zone 11N, WGS84 (Snyder, 1987). Faults from Jennings (1975) and Jennings et al. (2000) are shown as thin black lines.

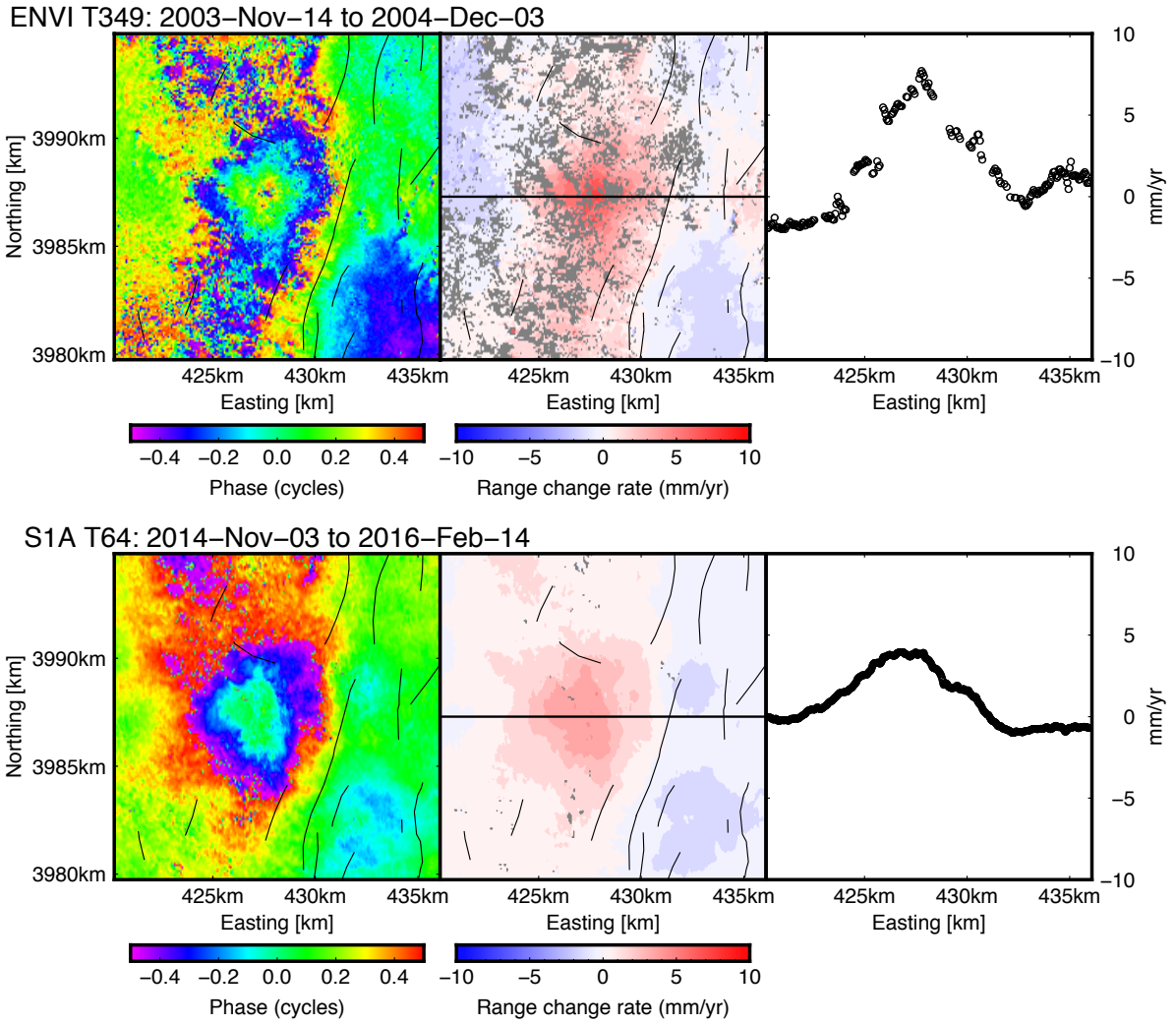

Figure 3.2: Example interferograms from ENVISAT and Sentinel-1A satellites spanning the production interval. For each pair (row), the left panel shows wrapped phase in cycles, the middle panel shows range change rate in mm/year, and the right panel shows values of range change rate in mm/year taken along the profile (thick black line in the middle panel). The incidence angle (between line of sight from the satellite and pointing straight down) is 21.1° and the azimuth (from North) is 94.6° for ENVISAT pairs. The incidence angle is 39.7° and the azimuth is 96.3° for Sentinel-1A pairs. One cycle of color in wrapped phase corresponds to 28 mm of range change. Plotting conventions as in Figure 3.1.

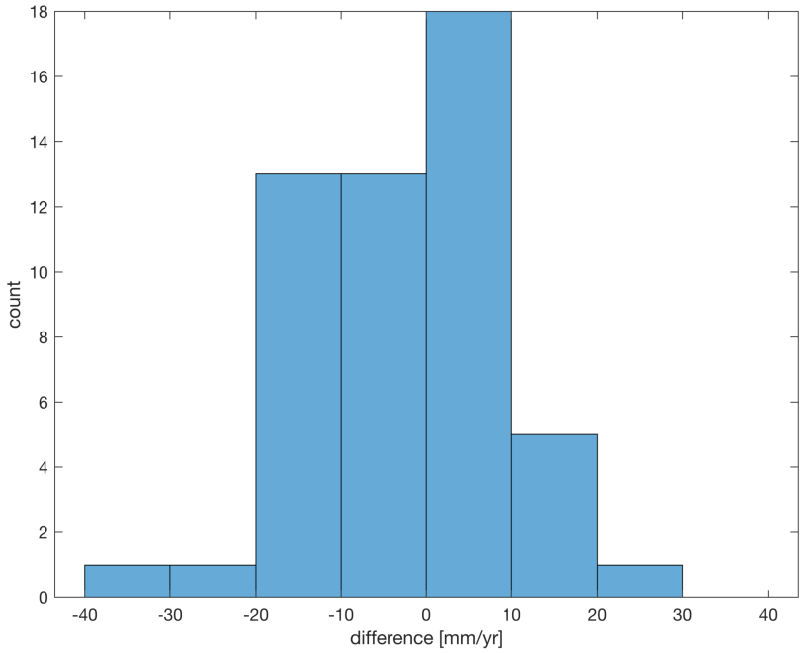

Figure 3.3: Histogram of differences between range change rate at COSO with respect to COSJ estimated from GPS using linear interpolation and extrapolation and range change rates at COSO with respect to COSJ observed by ENVISAT pairs.

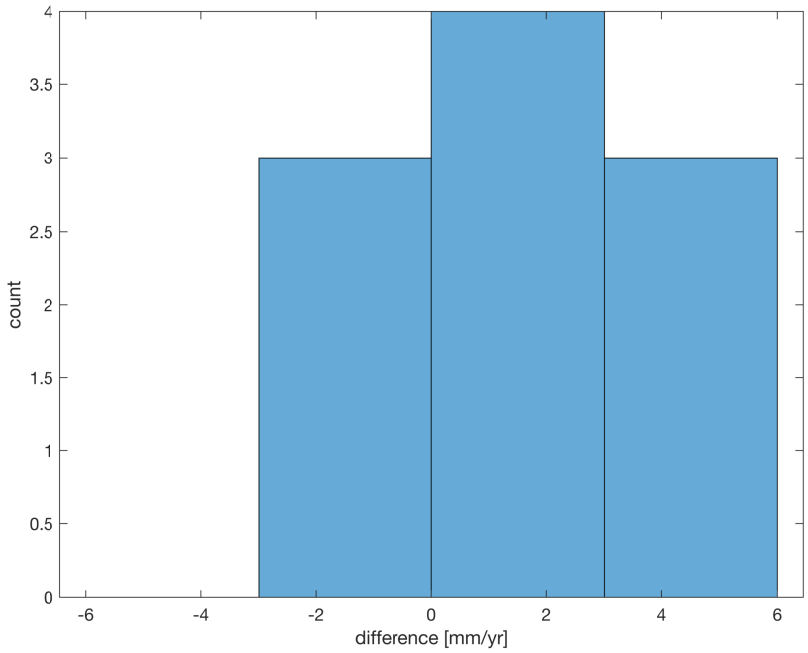

Figure 3.4: Histogram of differences between range change rate at COSO with respect to COSJ estimated from GPS using linear interpolation and extrapolation and range change rates at COSO with respect to COSJ observed by Sentinel-1A pairs.

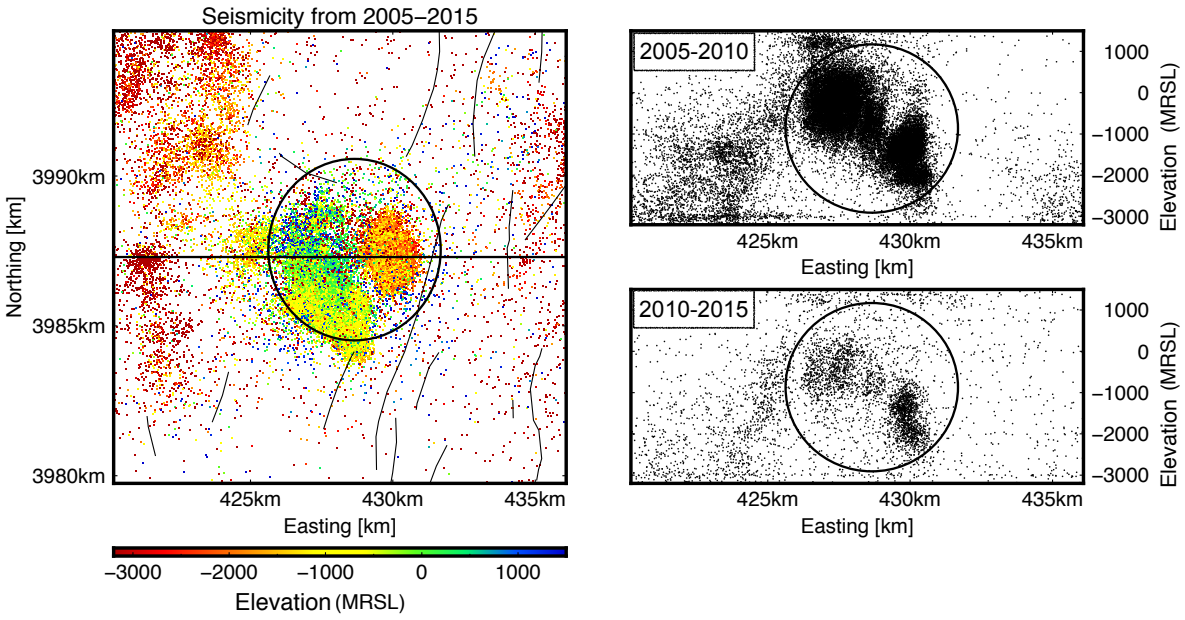

Figure 3.5: Map of seismic events at Coso from 2005 to 2015 with hypocenters located within the ellipsoidal volume modeled as a sink that fits the ENVISAT stack (Ali et al., 2016b). Coordinates are easting and northing in [km] in Universal Transverse Mercator projection zone 11N, WGS84 (Snyder, 1987). Events plotted in map view are colored by elevation in meters with respect to sea level (MRSL). Events along the profile shown in map view are plotted in cross section according to whether they occurred before or after 2010. Boundaries for the ellipsoidal volume used to select a subset of events are outlined in black.

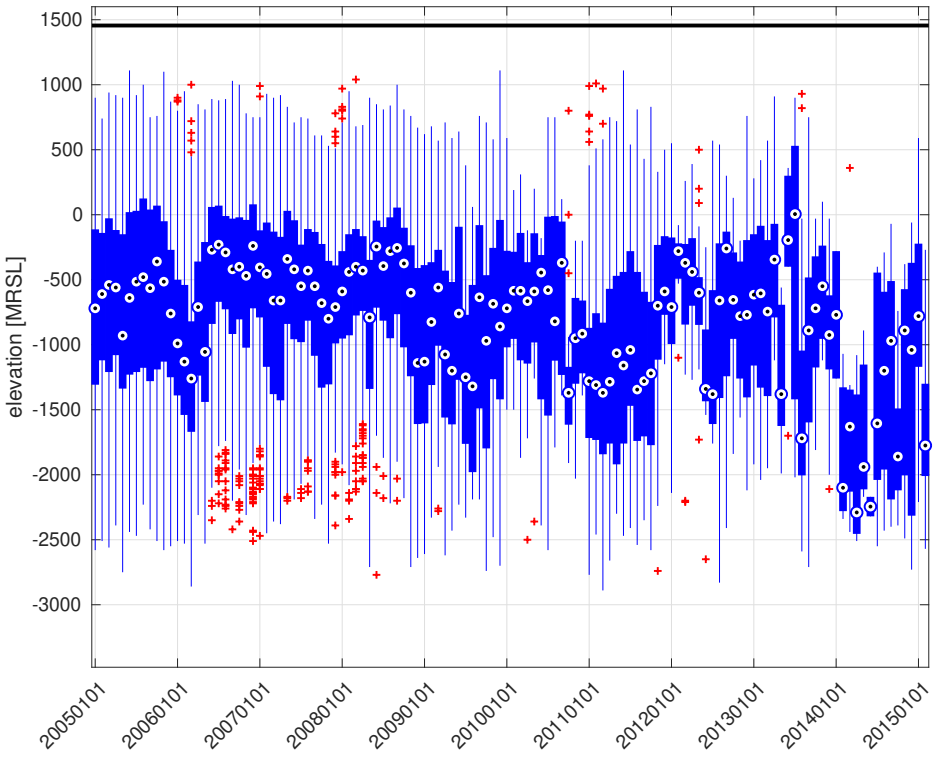

Figure 3.6: Box plot showing elevation of events in meters with respect to WGS84 ellipsoid subset over time period of interest. Dates are given in YYYYMMDD. Records are grouped by month. Median values are shown in white circles, box edges indicate the 25th and 75th percentiles. The range of values outside these percentiles but not considered outliers are shown as whiskers. Individual outliers are shown in red. Solid black line is the elevation 1455.4 m of GPS station COSO and represents a typical elevation at the field.

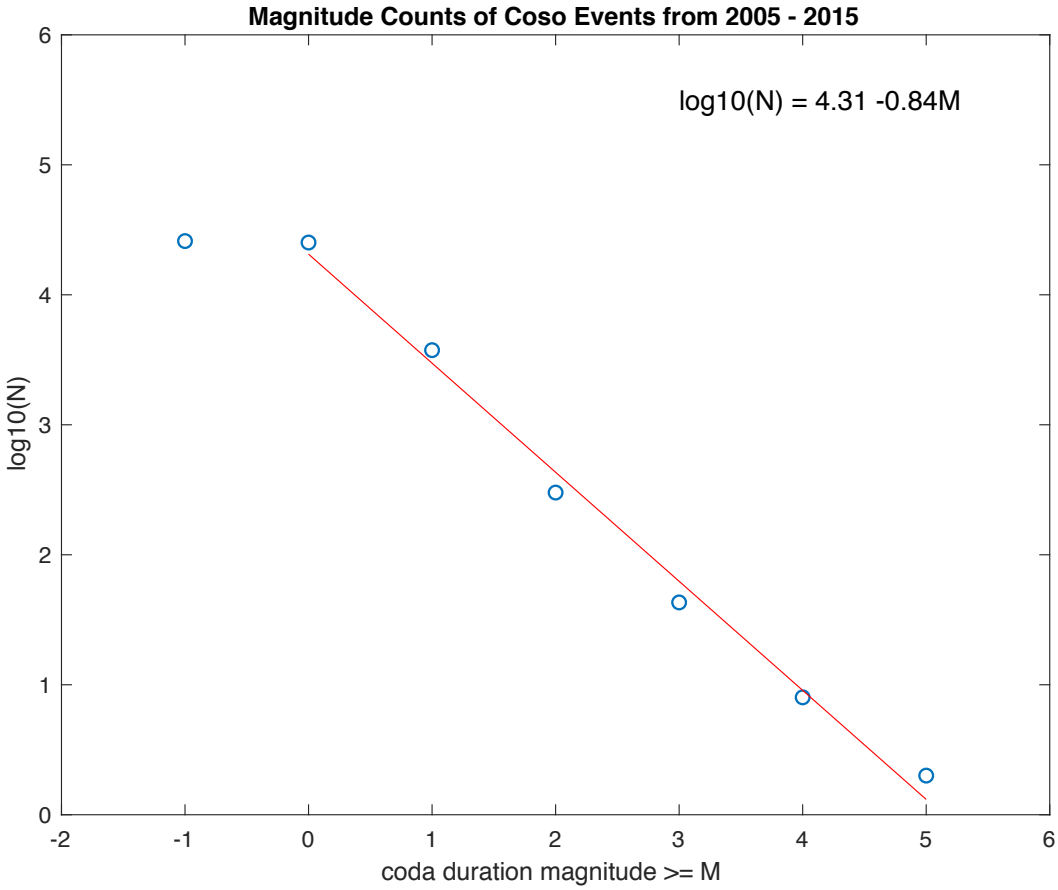

Figure 3.7: Number of seismic events grouped by magnitude from 2005 to 2015.

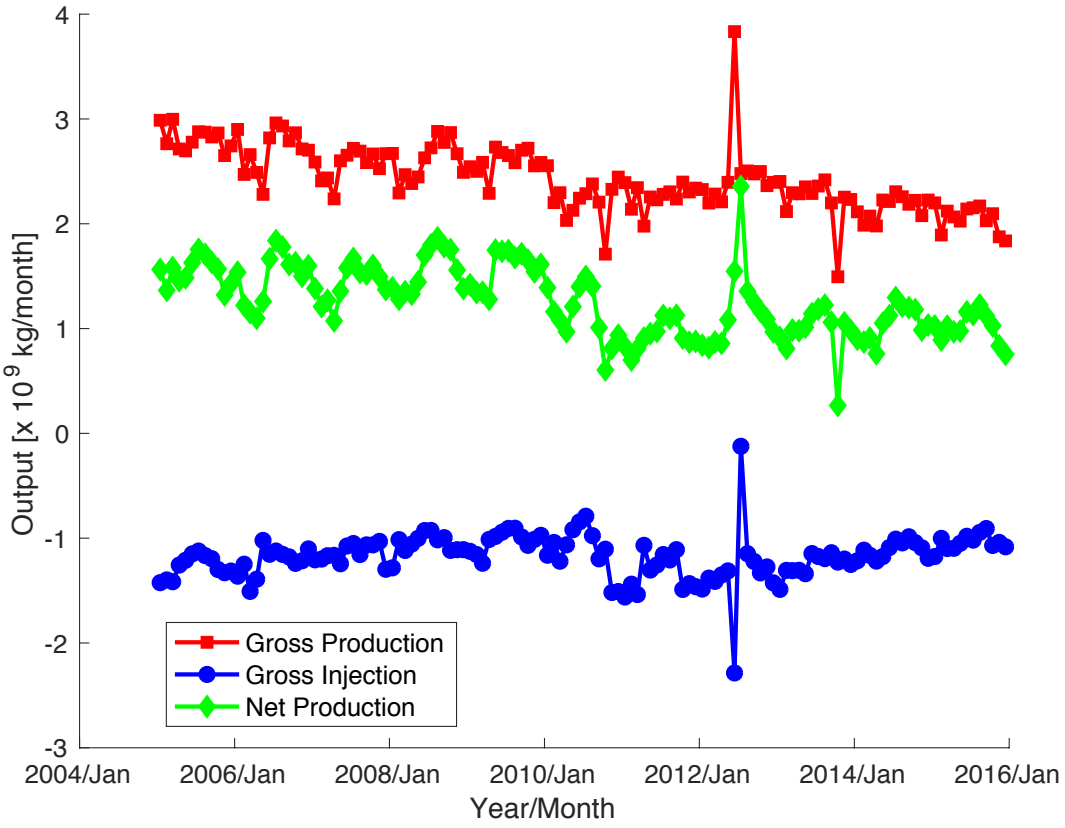

Figure 3.8: time-series showing rate of gross geothermal injection (blue), gross production (red), and net production (green) in kg/month. Data are from the Division of Oil, Gas, and Geothermal Resources (2016).

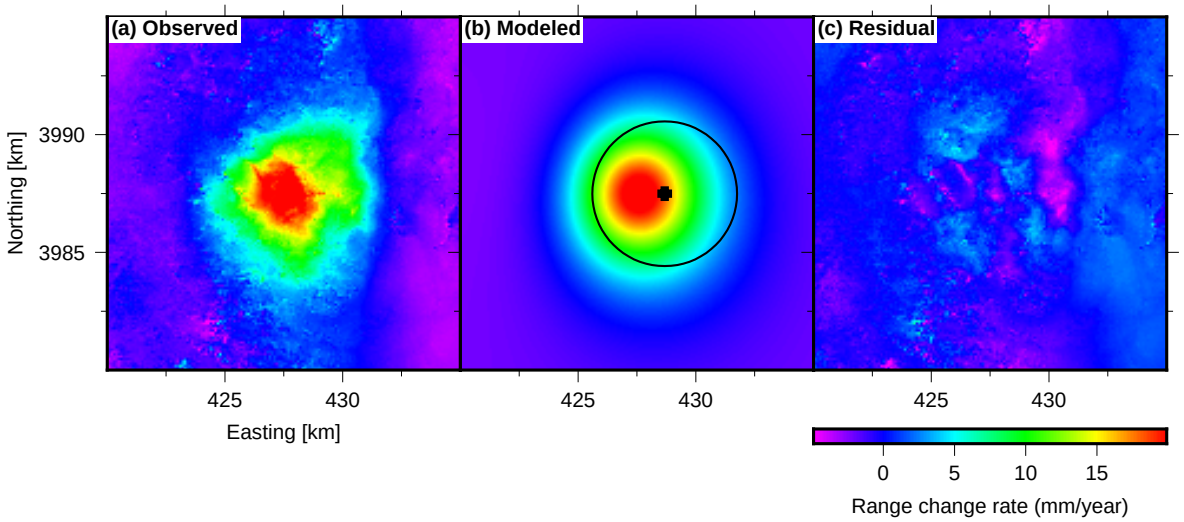

Figure 3.9: Deformation fields showing the finite element modeling results from Ali et al. (2016b) using a static Young's modulus of 25 GPa. (a) Observed deformation field from the ENVISAT stack in range change rate (mm/yr), (b) modeled values of range change rate from inversion with the center and dimensions of the modeled volume outlined in black, (c) residual values (observed minus modeled).

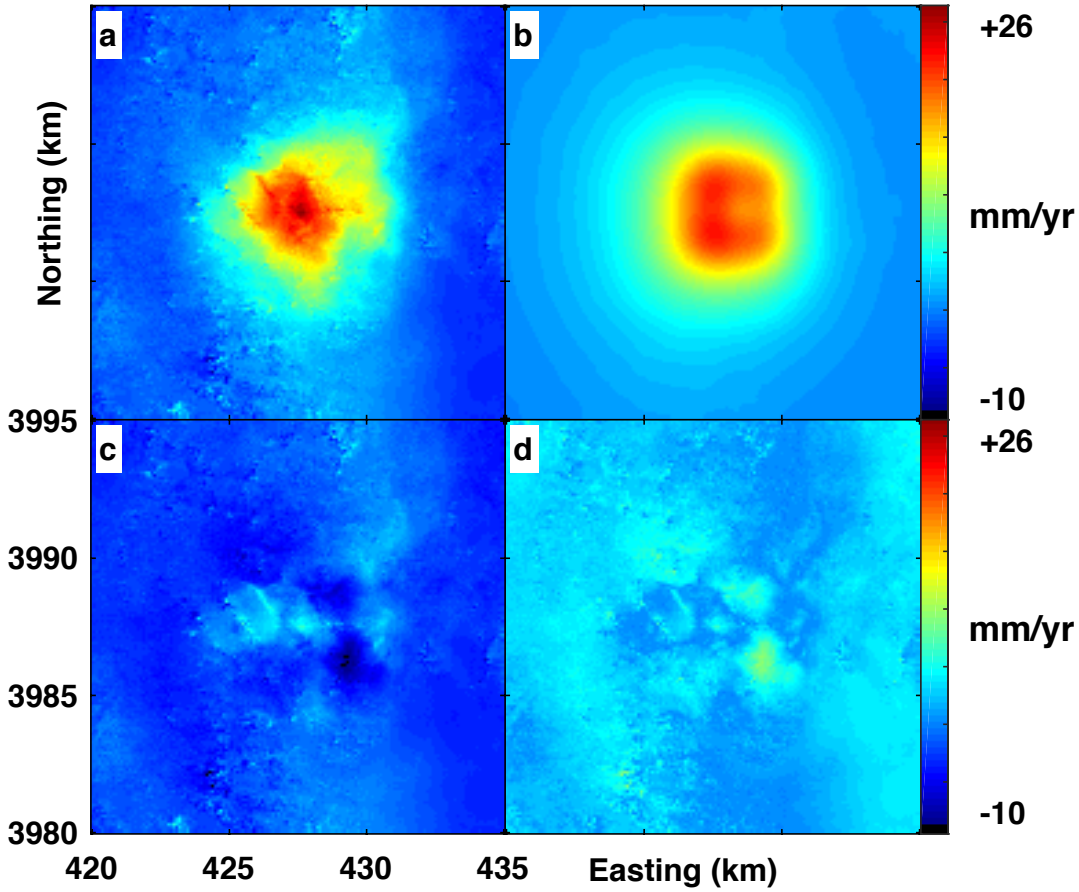

Figure 3.10: Deformation fields in terms of (unwrapped) range change rates from the MST Envisat stack spanning November 14, 2003 to September 3, 2010 analyzed using nonlinear inversion methods outlined in Feigl & Thurber (2009). The estimate of the parameter vector was based on finite element models by Ali et al. (2016b). Inversion was performed using unwrapped range change rates. Results are shown in terms of unwrapped range change rate: (a) observed range change rate, (b) modeled range change rate, (c) residual between observed and modeled, and (d) absolute value of residuals. We use the UTM coordinate system as in Figure 3.1.

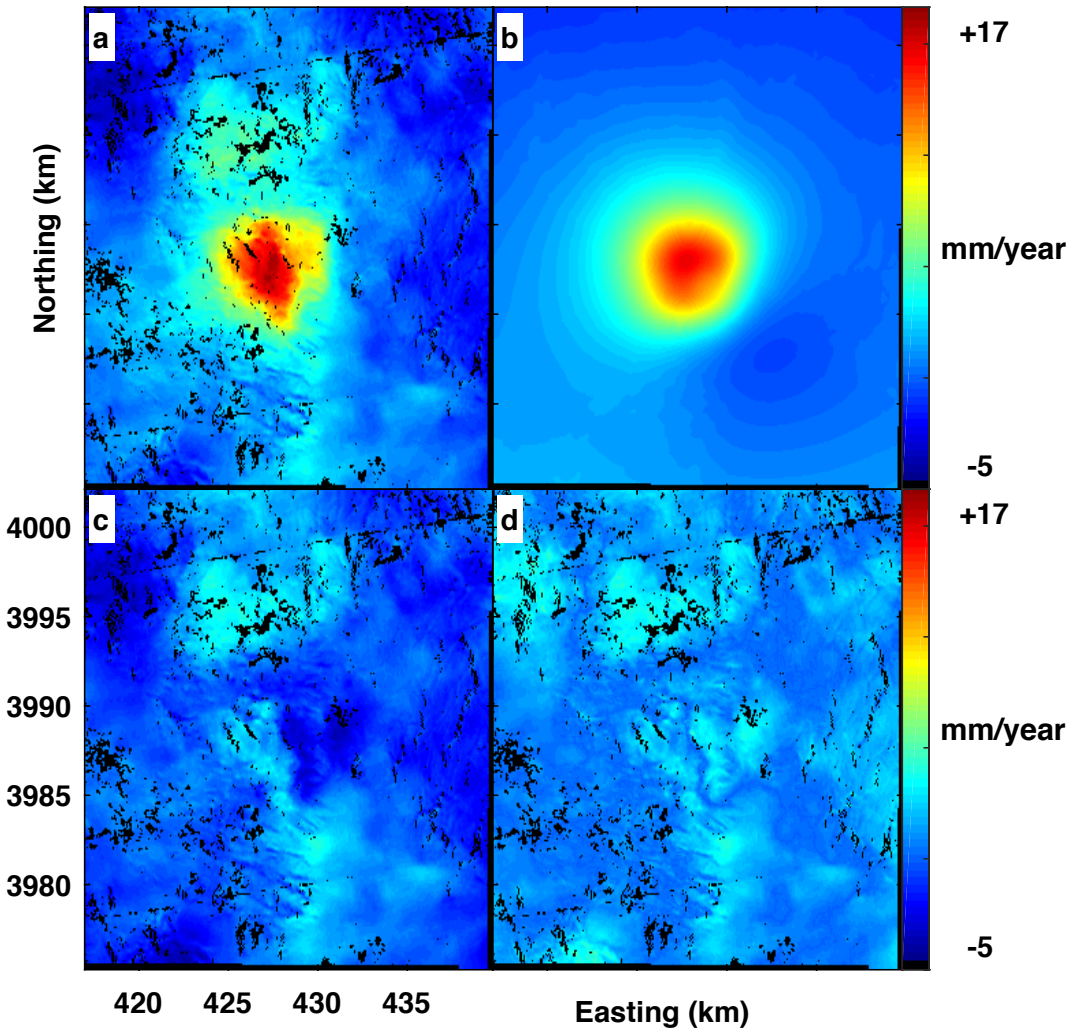

Figure 3.11: Deformation fields in terms of (unwrapped) range change rate from the Sentinel-1A stack spanning November 3, 2014 to April 26, 2016 analyzed using nonlinear inversion methods outlined in Feigl & Thurber (2009). The estimate of the parameter vector was based on finite element models by Ali et al. (2016b). Inversion was performed using unwrapped range change rates. Results are shown in terms of unwrapped range change rate: (a) observed range change rate, (b) modeled range change rate, (c) residual between observed and modeled, (d) and absolute value of residuals. We use the UTM coordinate system as in Figure 3.1.

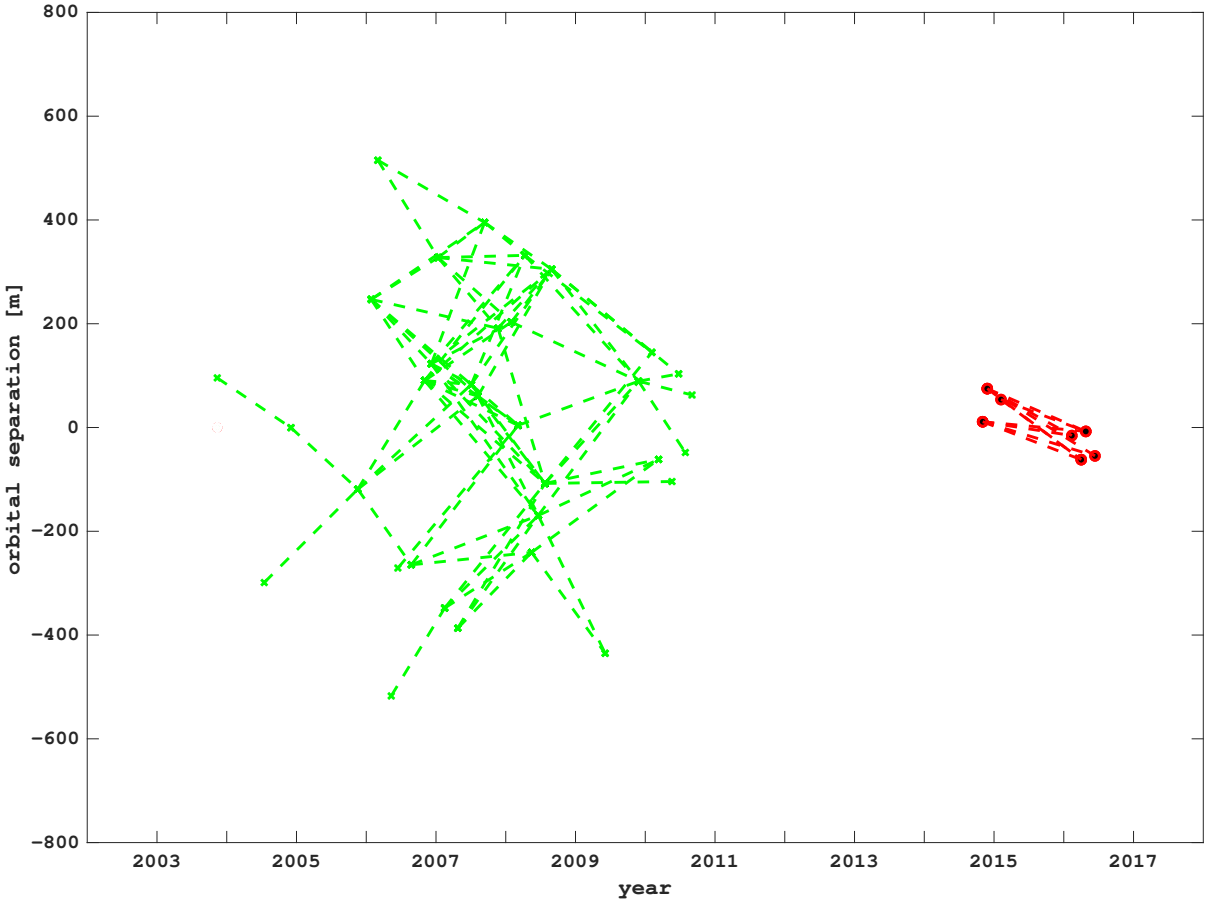

Figure 3.12: Interferometric pairs included in the temporal adjustment procedure. Pairs from component A (shown in green) are the minimum spanning tree subset of 81 pairs from ENVISAT between 2004 and 2010 picked according to orbital separation, plotted as the perpendicular component of the "baseline" vector separating the satellite's trajectories at the two times ("epochs") of image acquisition. Pairs from component B (shown in red) are the 10 pairs from the Sentinel-1A satellite between 2014 and 2016.

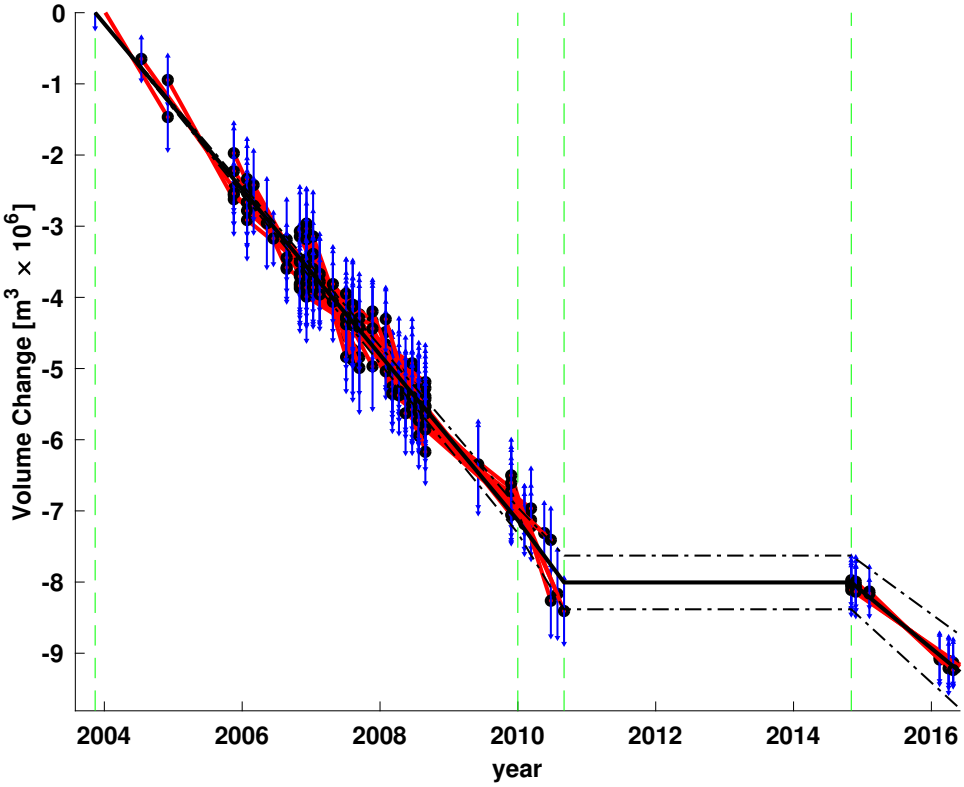

Figure 3.13: Time series at Coso, showing cumulative volume change in the cuboidal source over time from temporal adjustment of volume change rates estimated from InSAR data spanning 2004 to 2016. Black lines show the modeled volume change with 68% confidence intervals (dashed lines) as estimated by temporal adjustment with a piecewise-linear temporal function (Reinisch et al., 2017). Red segments indicate measurements of observed volume change derived from individual interferometric pairs. For each pair, the volume change at the mid-point of each time interval is plotted to fall on the modeled curve and the vertical blue bars denote 1σ measurement uncertainty, after scaling by the square root of the variance scale factor.

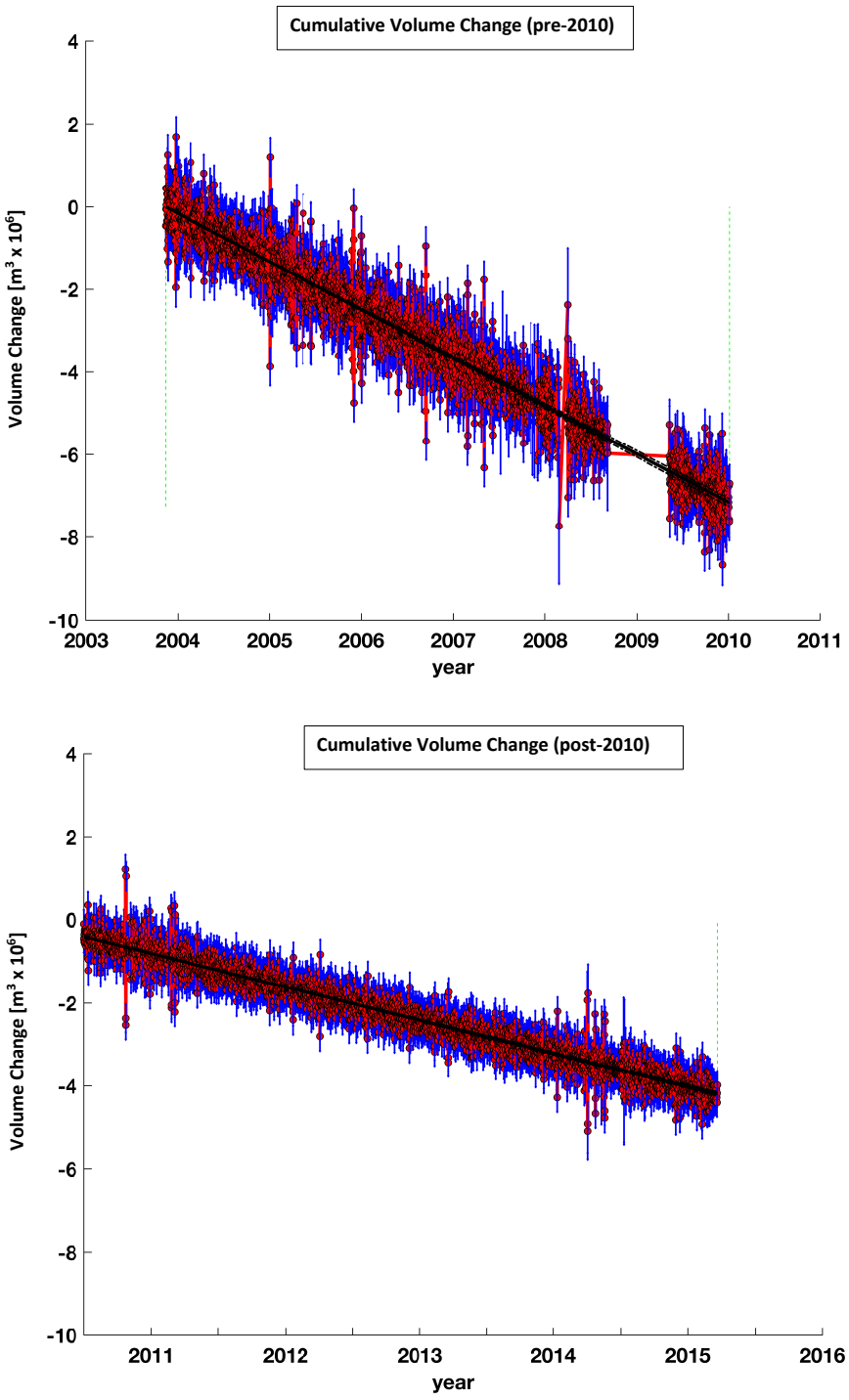

Figure 3.14: Time series at Coso, showing cumulative volume change over time from temporal adjustment of volume change rates estimated from GPS data spanning 2004 to 2016. Data before 2010 is shown above. Data after 2010 is shown below. Plotting conventions as in Figure 3.13.

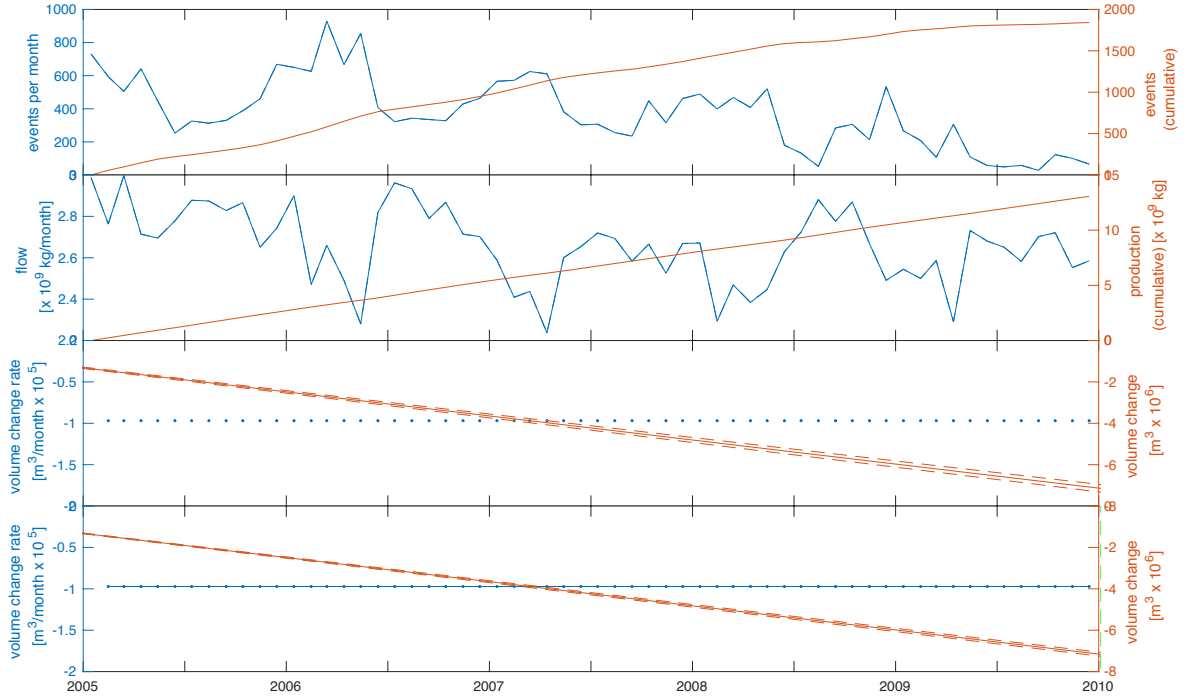

Figure 3.15: Comparison of analyzed data sets at Coso showing rates and cumulative values before 2010. For each panel, the rate is shown in blue with the scale on the left and the cumulative amount in orange with the scale on the right. (a) Seismicity in terms of monthly rate of seismic events located within the main field (blue) and cumulative events per month (orange). (b) Pumping in terms of monthly rate of gross production [kg/month] (blue) and cumulative gross production [kg]. (c) Best-fitting estimates of volume change from temporal adjustment of InSAR data in terms of monthly volume change rate [m^3/month] (blue) and cumulative volume change with 68% confidence bounds (orange). (d) Best-fitting estimates of volume change from temporal adjustment of GPS data in terms of monthly volume change rate [m^3/month] (blue) and cumulative volume change with 68% confidence bounds (orange).

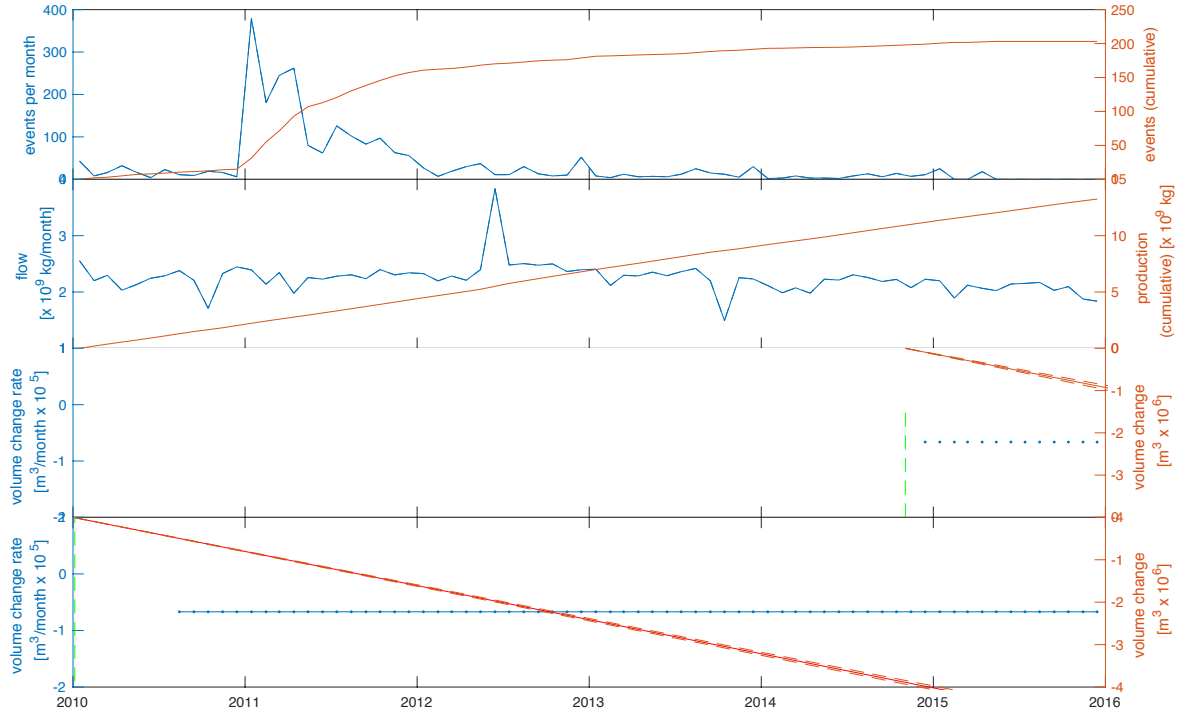

Figure 3.16: Comparison of analyzed data sets at Coso showing rates and cumulative values after the start of 2010. Plotting conventions as in previous figure.

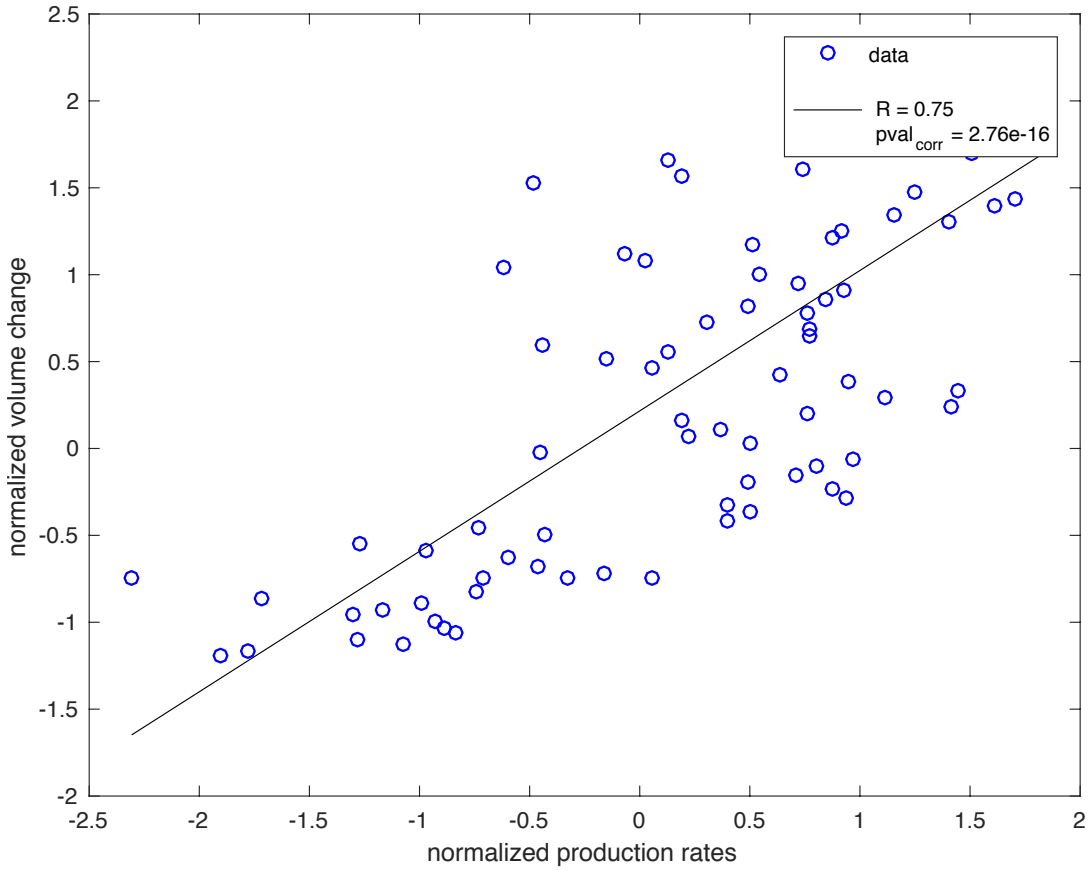

Figure 3.17: Scatter plot showing the monthly volume change estimated from temporal adjustment of InSAR data and monthly gross production rates.

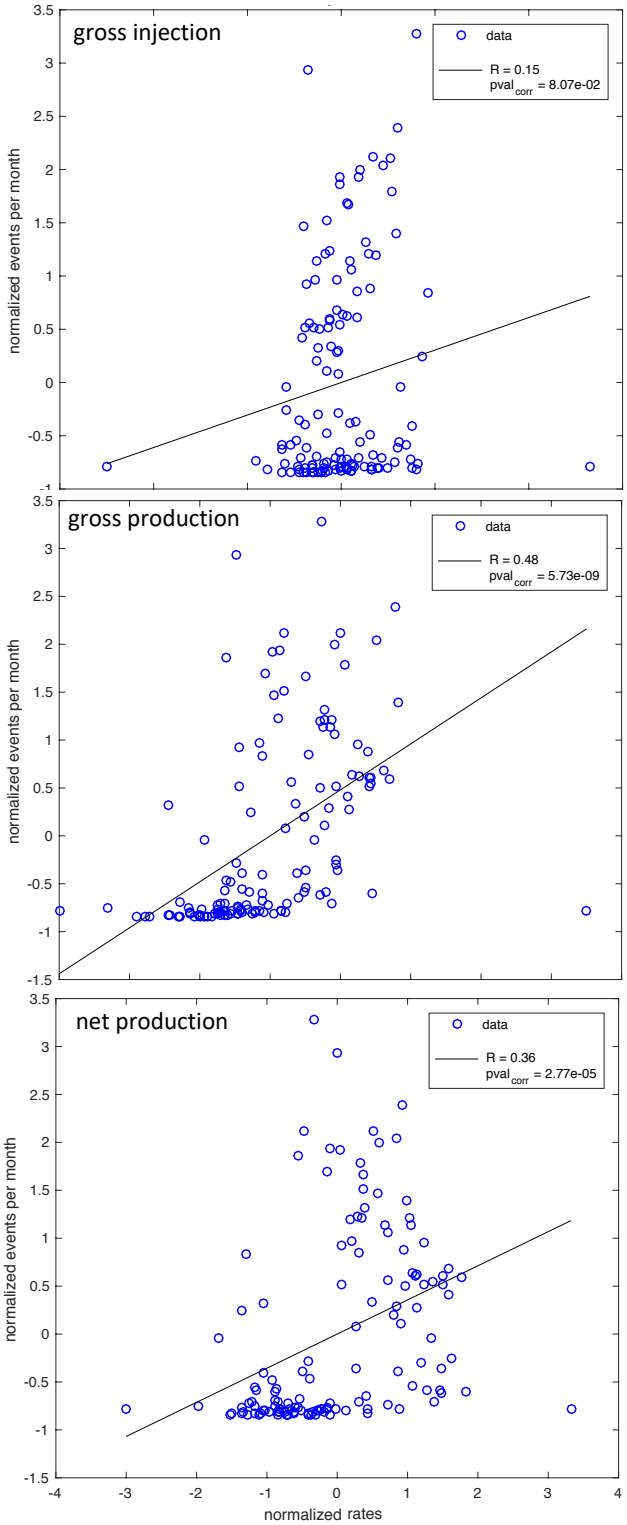

Figure 3.18: Scatter plots showing the number of seismic events per month and (a) monthly gross injection rate, (b) monthly gross production rate, and (c) net production rate.

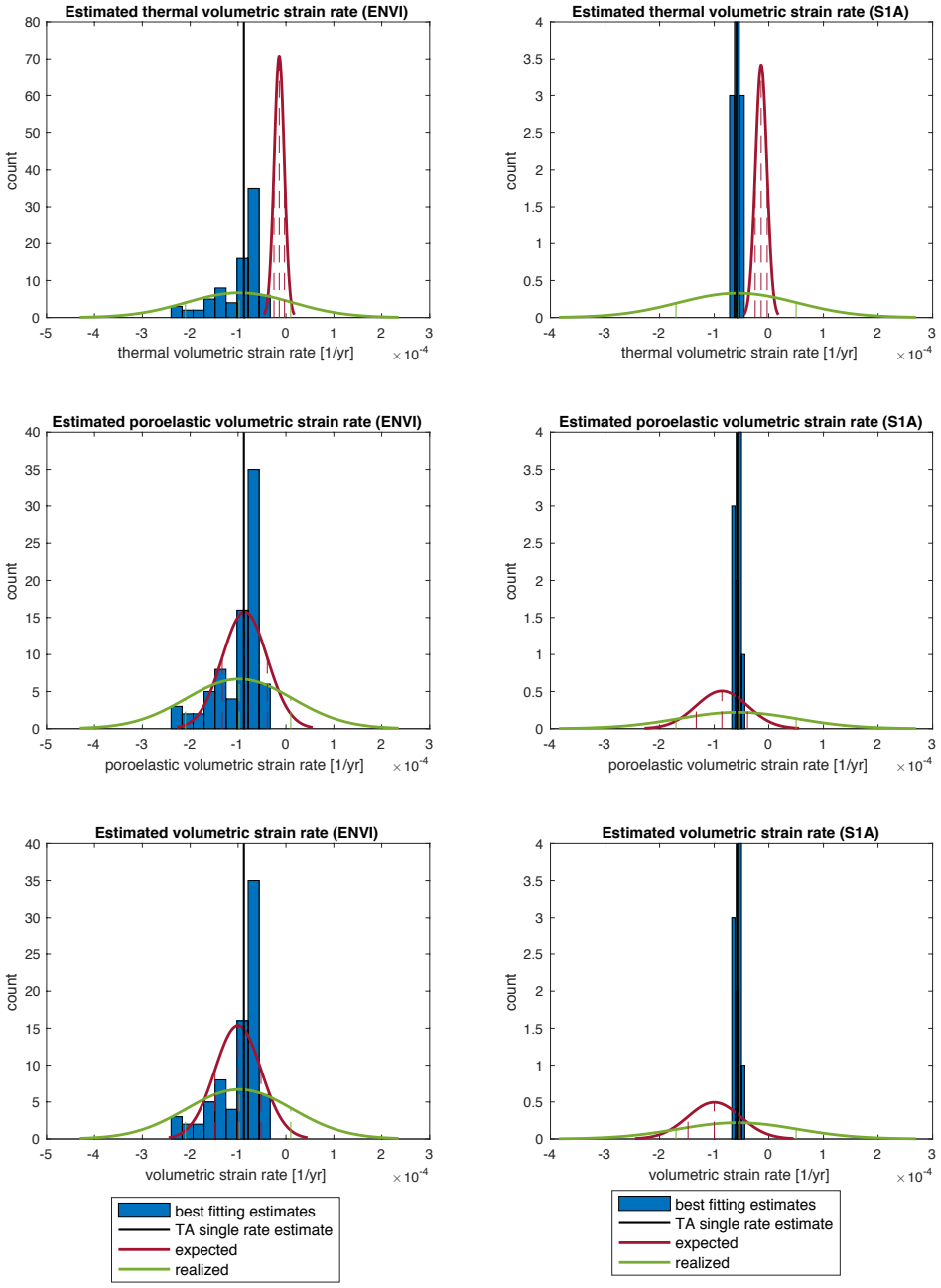

Figure 3.19: Histograms of best-fitting estimates of volumetric strain rates interpreted in terms of thermal contraction of the rock matrix (first row), a decrease in pore-fluid pressure (second row), and a linear combination of the two (third row) for ENVISAT pairs corresponding to the time interval from 2004 to mid-2010 (first column) and Sentinel-1A pairs corresponding to the time interval between 2014 and 2016 (second column). Overlain are 68% confidence intervals for reasonable values defined *a priori* (red) and realized values from deformation modeling (green). Also shown is the best fitting estimate of mean strain rate (black) found from temporal adjustment with a single rate temporal function.

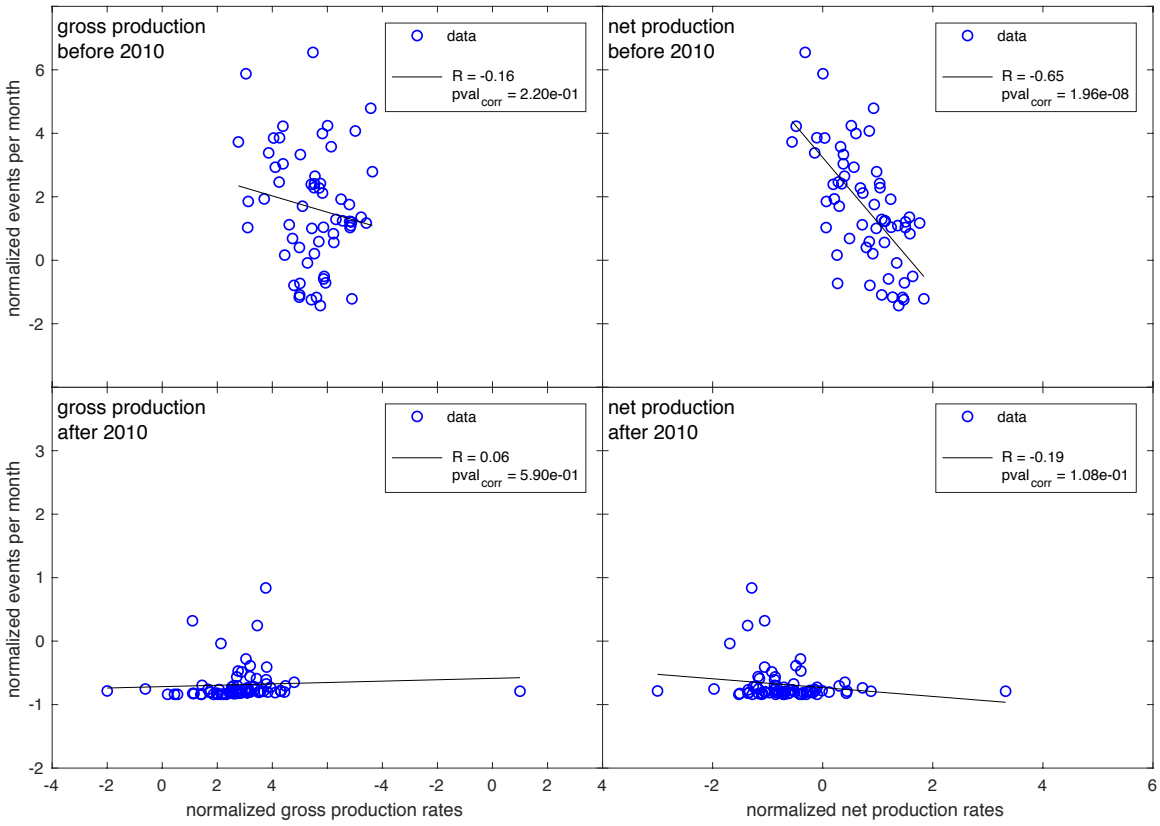

Figure 3.20: Scatter plots showing normalized monthly seismicity rate compared to normalized monthly gross production rate (first column) and normalized monthly net production rate (second column) both before and after the start of 2010 (first and second rows, respectively).

4 Spatio-temporal Analysis of Deformation at San Emidio Geothermal Field, Nevada, USA Between 1992 and 2010

This work has been submitted to *Remote Sensing* special issue "InSAR for Earth Observation" on June 28, 2019 with the following author list: Elena C. Reinisch, Michael Cardiff, John Akerley, Ian Warren, and
Kurt L. Feigl.

Abstract

Although subsidence has been observed at San Emidio geothermal field in Nevada using interferometric synthetic aperture radar since the early 1990s, the spatial extent and temporal evolution of the subsidence have not heretofore been quantified. We develop a deformation model to characterize the spatial extent of subsidence at San Emidio in terms of volume change of the reservoir. We also examine the temporal relationship between the observed deformation and pumping at the site. Comparison between data products from our analysis and SQUEESAR data products from a previous study at San Emidio identifies distinctions between different approaches to interferometric deformation analysis for areas with poor correlation and low quality interferograms.

4.1 Introduction

San Emidio geothermal field is located $\sim$100 km N of Reno, Nevada in the Basin and Range Province. The field resides in the San Emidio Desert with the Fox Range to its west and the Northern Lake Range to its east (Rhodes, 2011). The faulting regime at San Emidio is predominantly N-striking and W-dipping and consists of two major faults: the Northern Lake Range fault and the San Emidio fault (Rhodes, 2011; Eneva et al., 2011). Near the operating

power plant, the San Emidio fault is intersected by a NNE-striking normal fault. There is also an ENE-striking sinistral-normal fault located in the northeast portion of the region that connects two strands of the Northern Lake Range fault system (Rhodes, 2011; Eneva et al., 2011).

In 1987, a binary power plant began operating under the supervision of Empire Geothermal Power LLC in the SW region of San Emidio with a capacity of 3.6 MW (Warren et al., 2018) (Figure 4.1). The plant used shallow production wells between 30 to 100 m depth until the early 2000s. To address the issue of cooling in the shallow reservoir, new production wells were installed at depths between 500 and 700 m along the San Emidio fault and the original production wells were converted to injection wells (Warren et al., 2018). In 2008, the ownership of the power plant changed to Geothermal Inc., who commissioned a new plant with an operating capacity of 14.7 MW in 2012 (Warren et al., 2018).

The geographic location of San Emidio and its resulting weather conditions present challenges to modeling the deformation observed at San Emidio by interferometric synthetic aperture radar (InSAR) due to poor correlation and low quality among interferometric pairs. In addition, the signature of the deformation signal at San Emidio is small. A previous study by Eneva et al. (2011) employs a method which makes use of both persistent and distributed scatterer processing to improve data quality and enhance signal detection in InSAR pairs (SQUEESAR, Ferretti et al., 2011). While effective, this method can be computationally expensive.

In this study, we explore improving pair selection using a minimum spanning tree (MST) algorithm with a weighting criterion defined to avoid pairs with low quality while simultaneously selecting pairs with clearer deformation signal. We establish a deformation model that spatially characterizes the subsidence signal at San Emidio. Using time-series analysis on a data set of pairs spanning from 1992 to 2010, we estimate how deformation changes over time at the field.

4.2 Data

We select the same sets of Synthetic Aperture Radar (SAR) scenes as used by Eneva et al. (2011) to facilitate comparison between the resulting interferometric (InSAR) data products. This includes 98 epochs from the C-band Envisat (ENVI) satellite (McLeod et al., 1998): 53 from descending track 27 and 45 from ascending track 120. Also included are 38 epochs from the descending track 27 of the European Remote-Sensing satellite missions ERS-1 and ERS-2 (Fletcher, 2013). These epochs are listed in Table 4.1.

Interferograms are calculated by combining pairs of compatible images using GMTSAR (Sandwell et al., 2011a,b), an interferometric processing software package that utilizes Generic Mapping Tools (GMT) to create and visualize interferometric pairs. GMTSAR allows for removal of noise by applying a modified Goldstein filter that depends on coherence (Goldstein & Werner, 1997; Baran et al., 2003; Sandwell et al., 2011b).

4.3 Methods

4.3.1 Selecting and Weighting Pairs

Given each of the three satellite track's set of epochs (at points in time), we select a data set of pairs (spanning intervals in time). To do so, we consider image quality as measured by the amount of phase noise within an interferometric pair (e.g., McLeod et al., 1998). Factors that contribute to quality include: (a) the orbital separation (also known as the perpendicular component $B_\perp$ of the baseline), (b) the time span of the pair (also known as the temporal baseline), and (c) the difference in Doppler centroid frequencies (e.g., Refice et al., 2006; Perissin & Wang, 2012; Agram & Simons, 2015). One popular approach is to select minimum spanning tree (MST) pairs using orbital separation as a weighting criterion (e.g., Berardino et al., 2002). This method falls short, however, when imaging mountainous areas such as northern Nevada, which receive considerable precipitation in winter months.

To address these complications, we weight pairs by a measure of their quality. We use an empirical measure of quality $\gamma(i,j)$ for a pair spanning from time t_i to time t_j as defined by the product of three individual components (Rodriguez & Martin, 1992; Refice et al., 2006; Moreira et al., 2013):

$$\gamma(i,j) = \gamma_g(i,j) \cdot \gamma_t(i,j) \cdot \gamma_D(i,j) \tag{4.1}$$

where subscripts g, t, and D represent geometric, temporal, and Doppler contributions, respectively. We define these individual coherence components in a manner similar to that of Refice et al. (2006) and incorporate additional complexity in the geometric and temporal components.

The geometric component is defined as:

$$\gamma_g(i,j) = \left(1 - \frac{|b_\perp(i,j)|}{w_b b_{crit}}\right) \cdot [\mathcal{H}(w_b b_{crit} - |b_\perp(i,j)|)] \tag{4.2}$$

where b_{crit} represents the critical baseline (about 1100 m for Envisat and ERS (Holzner, 2003; Refice et al., 2006)), w_b is a specified weighting value for the critical baseline (set to be 0.5), and $\mathcal{H}$ represents the Heaviside "step" function. The Heaviside function is used to filter pairs with orbital separation greater than $w_b b_{crit}$.

The temporal component is defined using an exponential decay function:

$$\begin{aligned}\gamma_t(i,j) = \exp\left(\frac{-|\Delta t|}{b_{temp}}\right) \cdot \Big[&\min[\min[\mathcal{H}(m_{t_i} - 3.5), 1 - \mathcal{H}(m_{t_i} - 11.5)], \\ &\min[\mathcal{H}(m_{t_j} - 3.5), 1 - \mathcal{H}(m_{t_j} - 11.5)]\Big]\end{aligned} \tag{4.3}$$

where Δt is the time span (in absolute value) of the pair in days, b_{temp} is a specified temporal decay constant (set to 80 days), and m_{t_i} is the numerical value of the month of t_i. In this case, we use the Heaviside function to filter pairs with epochs occurring during winter months (mid-November through mid-March).

Finally, the Doppler component of the coherence is defined as:

$$\gamma_D(i,j) = \left(1 - \frac{|f_{Dc}(i) - f_{Dc}(j)|}{B_a}\right) \cdot [\mathcal{H}(B_a - |f_{Dc}(i) - f_{Dc}(j)|)] \tag{4.4}$$

where f_{Dc} is the Doppler centroid frequency [Hz] for each image and B_a is the azimuthal bandwidth [Hz].

We normalize γ to be between zero and one and set a MST weighting criterion of

$$w(i,j) = 1 - \gamma_{norm}(i,j). \tag{4.5}$$

The resulting subset of pairs optimizes the quality of the interferograms. This data set includes three trees in a minimum spanning forest (MSF) comprised of data from both the ERS and Envisat satellites, as graphed in Figure 4.2.

4.3.2 Deformation Modeling

We use simulated annealing to derive a model that best describes the deformation. This non-linear approach to deformation modeling is implemented in an open-source software package named the General Inversion of Phase Technique (GIPhT) (Feigl & Thurber, 2009; Ali & Feigl, 2012). For a given deformation model and a corresponding set of initial estimates and bounds for the parameters, GIPhT inverts data values from pixels of an observed interferogram using simulated annealing and outputs refined estimates of the model parameters. While GIPhT can use the observed values of either wrapped phase (in cycles) or unwrapped range change (in m), we work with wrapped phase change to avoid losing information and to avoid errors incurred from unwrapping (Feigl & Thurber, 2009).

We consider a simple model for the deformation observed at San Emidio. To describe the reservoir, we assume a cuboidal model with a single sink in an elastic half space with uniform material properties. The cuboid represents a volume element with sides of width W, length

L, and height H, giving an initial volume of $V_0 = LWH$. This volume element is defined by three rectangular patches that are mutually orthogonal. We estimate seven model parameters, including source location (easting, northing, and elevation), cuboid dimensions (length, width, and height), and volume change ΔV. We assume a uniform Poisson's ratio of $\nu = 1/4$. To start, we choose initial estimates of the location and dimension parameters based on results from Eneva et al. (2011). In addition to the seven parameters corresponding to the deformation model, we also estimate nuisance parameters corresponding to contributions from atmospheric effects, orbital errors, and an initial offset per epoch (e.g., Feigl & Thurber, 2009).

4.3.3 Time-series Analysis

To determine any temporal trends in the deformation, we perform time-series analysis on the estimated volume changes derived from the spatial deformation modeling. To handle the pair-wise nature of these volume changes, we use a graph-theoretic approach to the procedure known as temporal adjustment, which converts a series of individual, pair-wise volume changes $\Delta V_{i,j}$ into cumulative volume change at individual points t_i and t_j in time (Reinisch et al., 2017). We consider several different time functions, starting with a single-rate parameterization:

$$f_1(t_i) = a_1(t_i - t_0) \tag{4.6}$$

where $t_0 = 1992.43$ is the start date of our InSAR data set in decimal years.

We also consider a piecewise-linear parameterization with m breaks at times t_m that form

$(m-1)$ intervals:

$$f_2(t_i) = \Sigma_{j=1}^{j=m} a_j D(t_i), \text{ where}$$
$$D(t_i) = \begin{cases} 0 & \text{if } t_i < t_j \\ (t_i - t_j) & \text{if } t_j \leq t_i < t_{j+1} \\ (t_{j+1} - t_j) & \text{if } t_i \geq t_{j+1}. \end{cases} \tag{4.7}$$

where a_j is a parameter to be estimated.

4.4 Results

4.4.1 Analysis of Data Quality

To determine the quality of our data selection, we compare deformation measured from our MST data sets to those from Eneva et al. (2011) derived using the SQUEESAR procedure. We work with wrapped phase to avoid the additional uncertainty and potential loss of information caused by unwrapping (e.g., Feigl & Thurber, 2009). For each of the three sets of data, we calculate the eastward component of the phase gradient directly from wrapped phase using quadtree resampling (Ali & Feigl, 2012). As described by Ali & Feigl (2012), this quantity is one component of the deformation gradient (Malvern, 1969). We use quadtree resampling (Ali & Feigl, 2012) to smooth interferometric phases and derive the east component of the phase gradient fields to form a stack of interferometric pairs (Sandwell & Price, 1998). Both of these functionalities are incorporated into GIPhT. We also convert the SQUEESAR results from Eneva et al. (2011, , Fig. 2b,d) into wrapped phase and perform the same quadtree resampling and gradient procedure. Finally, we compare each of the three SQUEESAR stack gradients to the corresponding stack gradients of pairs selected by MST. The resulting gradient data sets are summarized in Table 4.2.

The mean and sample standard deviation of each differenced set of gradients is shown in Table 4.3 in terms of strain rate. We see that none of the three sets of differences is significantly different than zero. To determine if the means of the SQUEESAR stack gradients are different from the means of the MST stack gradients, we perform a Student's T-test. The results are summarized in Table 4.4 and Figure 4.3. All three data sets fail to reject the null hypothesis of equal means at 95% confidence. The (sample) standard deviations listed in Table 4.2 suggest that there are significant differences in variance between the data sets, which we confirm using an F-test at 95% confidence (e.g., Wackerly et al., 2007).

4.4.2 Deformation Modeling

We develop a best-fitting deformation model for San Emidio starting with the ENVI T27 stack of (unwrapped) range change rates derived by Eneva et al. (2011) using SQUEESAR. To avoid complications arising from signals due to sources other than those due to production at the site (e.g., precipitation, mining), we focus on only modeling the deformation observed around the production wells. We find that the deformation is best described by modeling the reservoir as a cuboidal sink. The best-fitting estimates of the model parameters are shown in Table 4.5. Results are shown in Figure 4.4. We define the cost of the inversion as the L1 misfit of the unwrapped range change rate (Ali et al., 2016a) and find it to be 0.7 mm/yr. We then model all individual pairs of wrapped phase change in our data set using the best-fitting estimates of the dimensions of the cuboidal sink.

4.4.3 Time-series Analysis

We work with volume change rates derived from modeling deformation from individual pairs using the cuboidal sink model. Starting with a single-rate parameterization (equation (4.6)), we find a best-fitting estimate of volume change rate to be $(-1.4 \pm 0.5) \times 10^4$ m^3/yr. We define a misfit χ of the model to the data as the square root of the reduced χ^2 statistic (Strang & Borre,

1997, p. 334). We find $\chi = 1.8$. Results are shown in Figure 4.5.

We also explore the possibility that the rate changes over time. We try a three-segment piecewise-linear parameterization with a break during the gap in the data set. We find best-fitting estimates of volume change rates for the two intervals of data coverage to be $(-1.3 \pm 0.1) \times 10^4$ m^3/yr for the time interval from 1992 to 2001 and $(-1.7 \pm 0.1) \times 10^4$ m^3/yr for the time interval from 2003 to 2010. We find a corresponding misfit of $\chi = 1.8$.

To determine if the increased complexity of the piecewise-linear parameterization is justified, we use an F-test for model complexity (e.g., Wackerly et al., 2007, p. 627). The results are shown in Table 4.6. We find that the added complexity of the piecewise-linear parameterization is not justified at 95% confidence. We conclude that the temporal trend of the volume change of the modeled reservoir is best explained as a constant rate.

4.5 Discussion

When we compare our MST data sets (selected using quality γ as a weighting criterion) to the corresponding data sets from SQUEESAR, we find no significant difference in stacked easting gradients at 95% confidence in all three InSAR data sets.

We find that the deformation at the San Emidio geothermal field is well explained by parameterizing the reservoir as a cuboidal sink (Figure 4.6). This sink aligns with faults in the area and spatially encompasses the majority of production and injection wells at the site. We found a best-fitting depth of 500 m, which is consistent with lower bounds of likely reservoir depths based on cross-section analyses (Matlick, 1995; Warren et al., 2018).

When modeling the observed deformation as a function of time, we find that the best-fitting parameterization is a constant rate of volume change. We compare the cumulative values of volume change derived from temporal adjustment with records of monthly average production reported to the State of Nevada to explore the possibility that the observed deformation is related to pumping at the site. We normalize the estimated cumulative volume change values and

the observed cumulative gross production values using the statistical Z-transform (e.g., Wackerly et al., 2007). We then test the correlation using Pearson's test (e.g., Wackerly et al., 2007, p. 599) with the null hypothesis that there is no correlation between pumping and deformation. We find a statistically strong correlation between normalized cumulative volume change and normalized cumulative gross production with a correlation coefficient of $R = 0.99$ and a p-value of $p << 10^{-100}$. Thus, we conclude that there is a significant correlation between deformation and pumping.

4.6 Conclusions

We have developed a new method to select a good set of interferometric pairs using a minimum spanning tree algorithm with a seasonally- and spatially-weighted measure of image quality as the weighting criterion. This selection procedure yields a temporally averaged phase gradient rate field that is equivalent in mean, but lower in variance, than that produced by the SQUEESAR procedure. Using nonlinear inversion, we determine that the deformation at San Emidio is well explained by parameterizing the reservoir as a cuboidal sink. Temporal analysis of volume change rates estimated from individual interferometric pairs using this deformation model suggests a constant rate of volume change between 1992 and 2010. When comparing cumulative volume change to cumulative gross production, we find an strong, positive correlation. This suggests that deformation at San Emidio may be influenced by geothermal production at the site.

4.7 Acknowledgements

Interferograms were created using GMTSAR processing software (Sandwell et al., 2011b,a). Several figures were created using the Generic Mapping Tools (Wessel et al., 2013). We gratefully acknowledge support from the Weeks family to the Department of Geoscience at the

University of Wisconsin-Madison. Raw Synthetic Aperture Radar (SAR) data from the ERS and Envisat satellite missions operated by the European Space Agency (ESA) are copyrighted by ESA and were provided through the WInSAR consortium at the UNAVCO facility.

Research was partially supported by grants from U.S. National Science Foundation (EAR-1654649 and EAR-1347190) and by the Geothermal Technologies Office of the U.S. Department of Energy under grants DE-EE0005510 and DE-EE0006760. Elena C. Reinisch was supported by grants from National Science Foundation Graduate Research Fellowship (DGE-1256259) and the Graduate School at UW-Madison.

Table 4.1: List of epochs in data set.

epoch (YYYYMMDD)	satellite	track	frame
19920503	ERS	T27	2799
19920607	ERS	T27	2799
19920712	ERS	T27	2799
19920816	ERS	T27	2799
19930103	ERS	T27	2799
19930418	ERS	T27	2799
19930627	ERS	T27	2799
19930905	ERS	T27	2799
19931219	ERS	T27	2799
19950411	ERS	T27	2799
19950516	ERS	T27	2799
19950620	ERS	T27	2799
19950829	ERS	T27	2799
19951107	ERS	T27	2799
19951108	ERS	T27	2799
19951212	ERS	T27	2799
19960116	ERS	T27	2799
19960117	ERS	T27	2799
19960430	ERS	T27	2799
19960501	ERS	T27	2799
19960814	ERS	T27	2799
19961023	ERS	T27	2799
19961127	ERS	T27	2799
19970312	ERS	T27	2799
19970730	ERS	T27	2799
19971008	ERS	T27	2799
19980506	ERS	T27	2799
19980610	ERS	T27	2799
19990106	ERS	T27	2799
19990804	ERS	T27	2799
19990908	ERS	T27	2799
20000405	ERS	T27	2799
20000510	ERS	T27	2799
20000614	ERS	T27	2799
20000719	ERS	T27	2799
20000823	ERS	T27	2799
20000927	ERS	T27	2799
20001206	ERS	T27	2799
20010110	ERS	T27	2799

20031029	ENVI	T120	801
20031203	ENVI	T120	801
20040623	ENVI	T27	2799
20040630	ENVI	T120	801
20040901	ENVI	T27	2799
20040908	ENVI	T120	801
20041006	ENVI	T27	2799
20041013	ENVI	T120	801
20041110	ENVI	T27	2799
20041117	ENVI	T120	801
20041222	ENVI	T120	801
20050119	ENVI	T27	2799
20050223	ENVI	T27	2799
20050302	ENVI	T120	801
20050330	ENVI	T27	2799
20050504	ENVI	T27	2799
20050511	ENVI	T120	801
20050608	ENVI	T27	2799
20050615	ENVI	T120	801
20050713	ENVI	T27	2799
20050720	ENVI	T120	801
20050817	ENVI	T27	2799
20050921	ENVI	T27	2799
20051026	ENVI	T27	2799
20051130	ENVI	T27	2799
20051207	ENVI	T120	801
20060111	ENVI	T120	801
20060208	ENVI	T27	2799
20060215	ENVI	T120	801
20060315	ENVI	T27	2799
20060419	ENVI	T27	2799
20060426	ENVI	T120	801
20060524	ENVI	T27	2799
20060531	ENVI	T120	801
20060628	ENVI	T27	2799
20060802	ENVI	T27	2799
20060906	ENVI	T27	2799
20061011	ENVI	T27	2799
20061018	ENVI	T120	801
20061115	ENVI	T27	2799
20061122	ENVI	T120	801
20061220	ENVI	T27	2799
20061227	ENVI	T120	801

20070124	ENVI	T27	2799
20070228	ENVI	T27	2799
20070307	ENVI	T120	801
20070404	ENVI	T27	2799
20070509	ENVI	T27	2799
20070613	ENVI	T27	2799
20070718	ENVI	T27	2799
20070822	ENVI	T27	2799
20071003	ENVI	T120	801
20071031	ENVI	T27	2799
20071107	ENVI	T120	801
20071212	ENVI	T120	801
20080109	ENVI	T27	2799
20080116	ENVI	T120	801
20080213	ENVI	T27	2799
20080220	ENVI	T120	801
20080319	ENVI	T27	2799
20080326	ENVI	T120	801
20080423	ENVI	T27	2799
20080430	ENVI	T120	801
20080528	ENVI	T27	2799
20080604	ENVI	T120	801
20080702	ENVI	T27	2799
20080709	ENVI	T120	801
20080806	ENVI	T27	2799
20080813	ENVI	T120	801
20080910	ENVI	T27	2799
20080917	ENVI	T120	801
20081015	ENVI	T27	2799
20090304	ENVI	T27	2799
20090311	ENVI	T120	801
20090408	ENVI	T27	2799
20090415	ENVI	T120	801
20090513	ENVI	T27	2799
20090520	ENVI	T120	801
20090617	ENVI	T27	2799
20090624	ENVI	T120	801
20090722	ENVI	T27	2799
20090729	ENVI	T120	801
20090826	ENVI	T27	2799
20090902	ENVI	T120	801
20090930	ENVI	T27	2799
20091007	ENVI	T120	801

20091111	ENVI	T120	801
20091209	ENVI	T27	2799
20091216	ENVI	T120	801
20100113	ENVI	T27	2799
20100120	ENVI	T120	801
20100217	ENVI	T27	2799
20100224	ENVI	T120	801
20100324	ENVI	T27	2799
20100331	ENVI	T120	801
20100428	ENVI	T27	2799
20100505	ENVI	T120	801
20100609	ENVI	T120	801

Table 4.2: Distribution parameters for SQUEESAR (SQR) and MST stack gradients for each satellite track.

Data set	SQR mean [picostrain/s]	MST mean [picostrain/s]	SQR sample std. deviation [picostrain/s]	MST sample std. deviation [picostrain/s]
ERS T27	-0.8×10^{-3}	-0.5×10^{-4}	3.3×10^{-1}	0.3×10^{-1}
ENVI T27	2.4×10^{-3}	2.4×10^{-3}	2.8×10^{-1}	0.4×10^{-1}
ENVI T120	-1.7×10^{-3}	-0.8×10^{-3}	3.4×10^{-1}	0.3×10^{-1}

Table 4.3: Distribution parameters for differenced SQUEESAR and MST stack gradients for each satellite track.

Data set	sample mean [picostrain/s]	sample std. deviation [picostrain/s]
ENVI T27	-4.2×10^{-5}	0.28
ENVI T120	8.6×10^{-4}	0.34
ERS T27	6.8×10^{-4}	0.34

Table 4.4: Results of Student's T-test for equal means (e.g. Wackerly et al., 2007, p. 521).
H_0: means are equal
H_1: means are significantly different
p-value: probability of rejecting H_0 when it is true

Data set	p-value
ERS T27	0.86
ENVI T27	0.97
ENVI T120	0.82

Table 4.5: Best-fitting estimates of a single cuboidal sink model after simulated annealing on unwrapped range change rates from ENVI T27 SQUEESAR stack.

Parameter Name	Best-fitting Estimate	Uncertainty
Centroid Easting in m	296,109	375
Centroid Northing in m	4,472,750	380
Centroid Depth in m	500	75
Cuboid Length in m	2000	500
Cuboid Width in m	200	50
Cuboid Thickness in m	500	100
Volume Change Rate (m^3/yr)	-4.6×10^3	0.5×10^3

Table 4.6: Results of F-tests for model complexity (e.g. Wackerly et al., 2007, p. 627).
H_0: both fits are equally good
H_1: more complex parameterization provides a significantly improved fit to the data over the single-rate parameterization
df denotes degrees of freedom.

df_1	df_2	test value	critical value	result
108	107	-7.37	1.38	fail to reject H_0

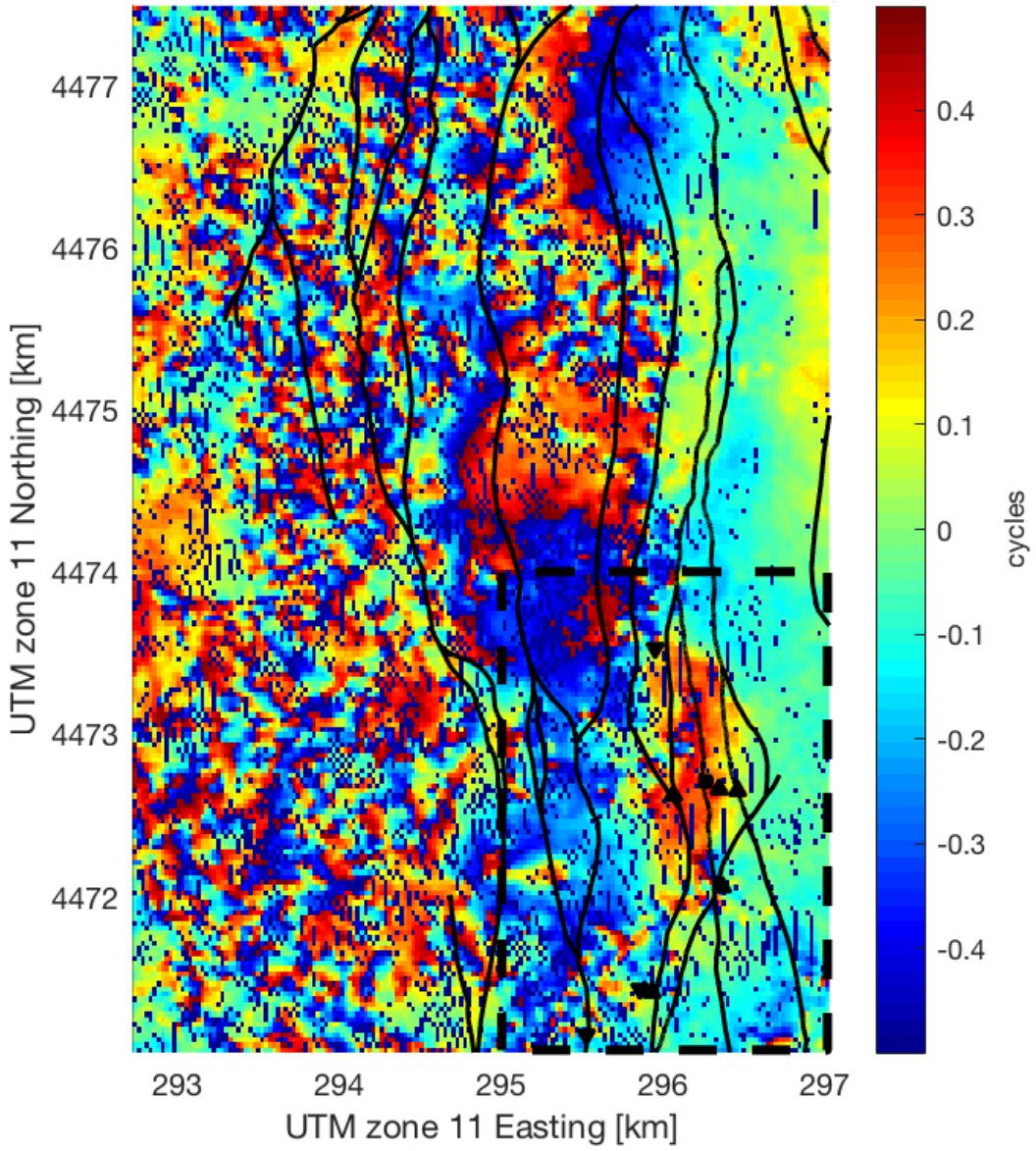

Figure 4.1: Deformation field at San Emidio in terms of wrapped range change [cycles] from an Envisat track 27 pair spanning 2004-Nov-10 to 2008-Sep-10. One cycle of wrapped phase corresponds to a range change of approximately 28 mm. The dashed rectangular region in the SE denotes the region used for deformation analysis in this study. Faults are denoted with black lines. Inverted triangles are injection wells and upright triangles are production wells. The power plant is denoted with a black square. Coordinates are easting and northing [km] in Universal Transverse Mercator (UTM) projection zone 11N, WGS84 (Snyder, 1987).

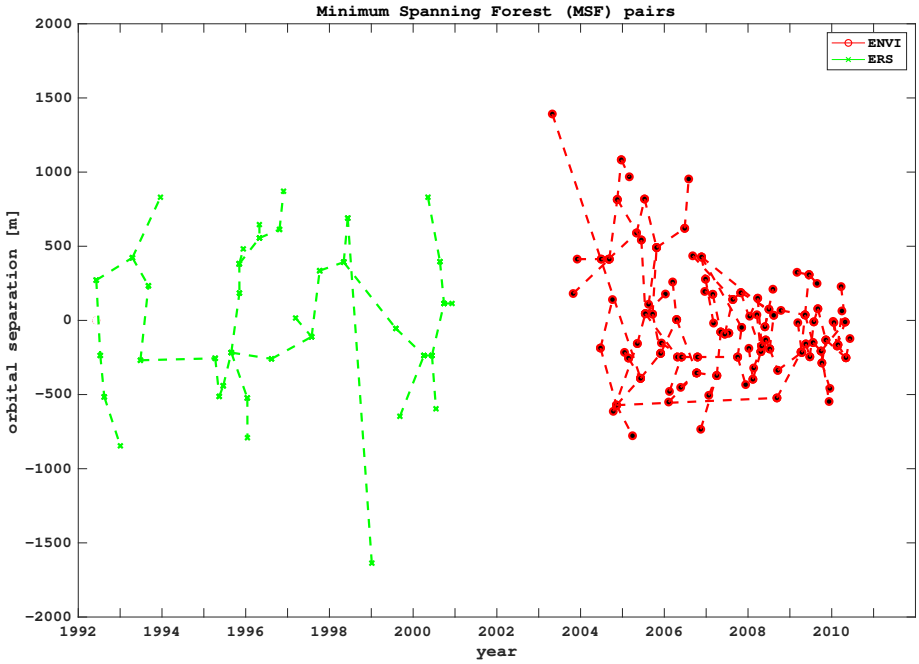

Figure 4.2: Graph showing pairs in the minimum spanning forest data set chosen by minimizing coherence. ERS-1/2 pairs are shown in green (track 27) and ENVI pairs are shown in red (tracks 27 and 120). Pairs are shown according to their orbital separation in m.

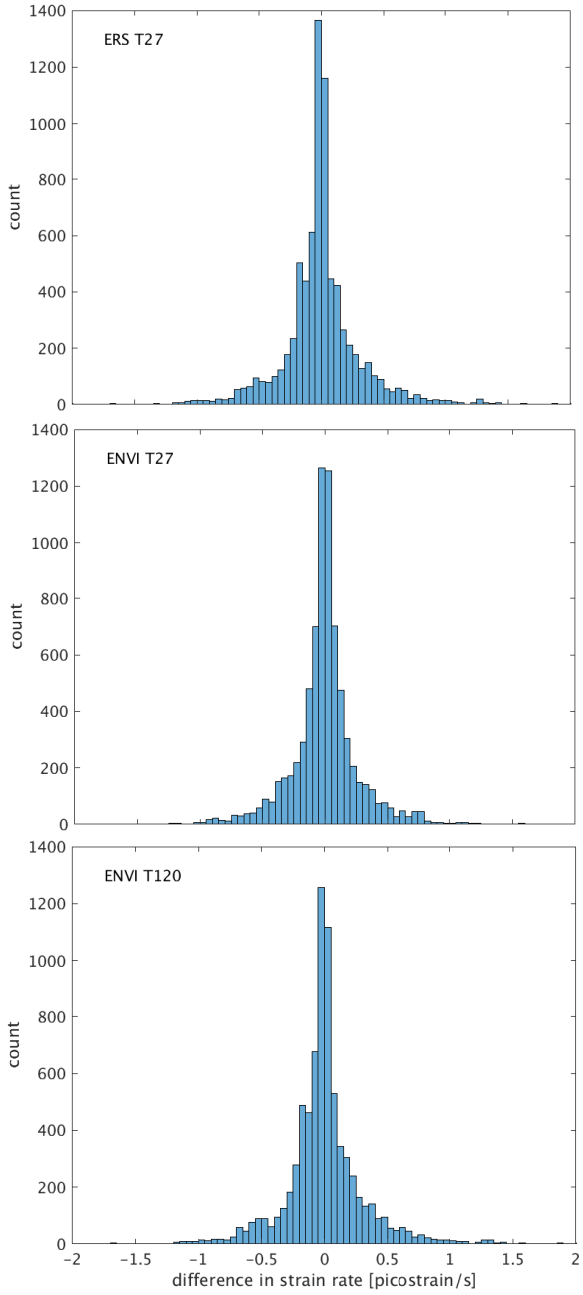

Figure 4.3: Histogram of differences between the SQUEESAR stack easting gradient field and the MST stack easting gradient field for all three InSAR data sets. Differences are shown in terms of strain rate (picostrain per second).

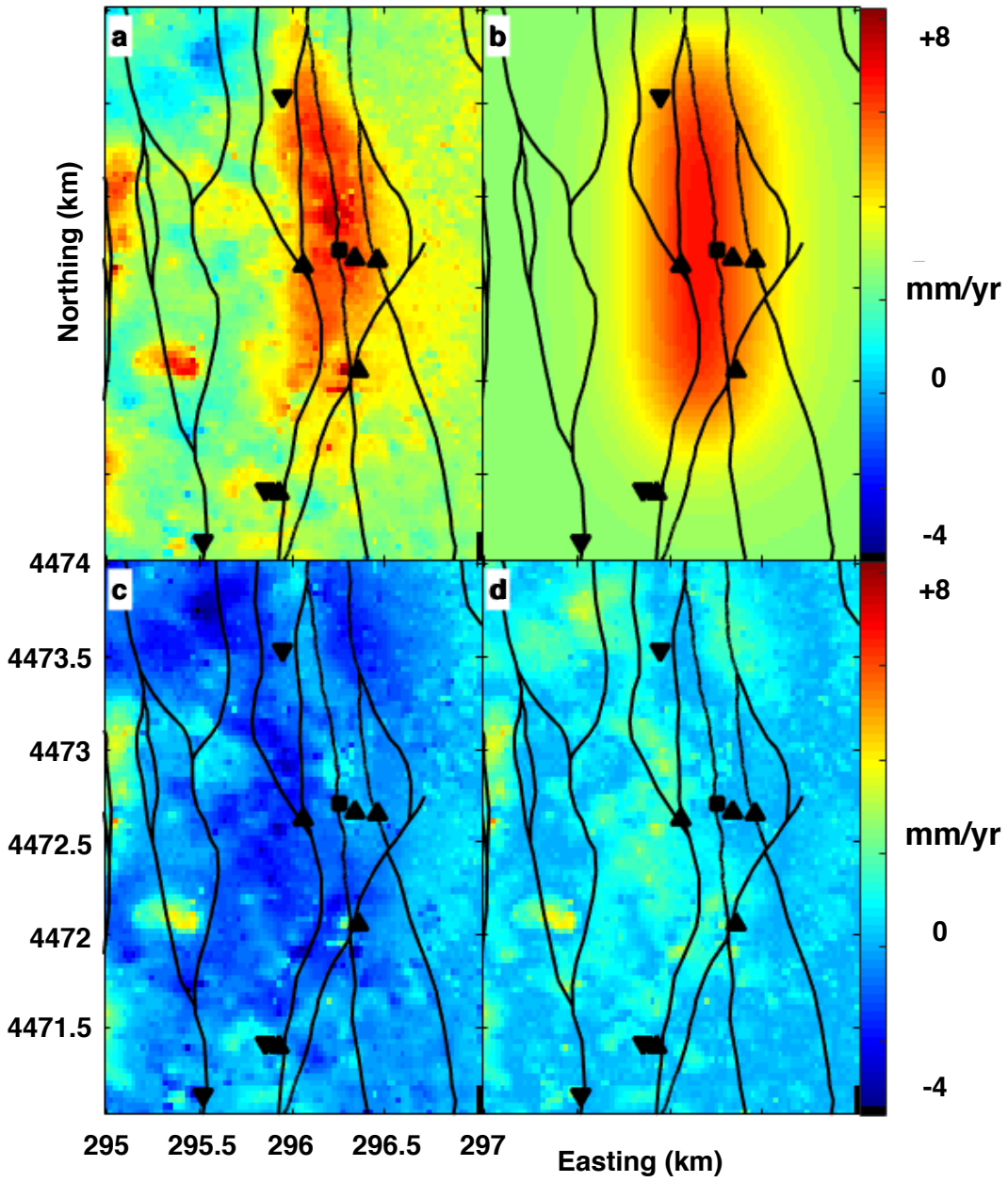

Figure 4.4: Deformation fields in terms of (unwrapped) range change rate from the SQUEESAR ENVI T27 stack spanning 2004-Jun-23 to 2010-Apr-28 analyzed using nonlinear inversion methods outlined in Feigl & Thurber (2009). Inversion was performed using unwrapped range change rates. Results are shown in terms of unwrapped range change rate: observed range change rate (a), modeled range change rate (b), residual between observed and modeled (c) and absolute value of residuals (d). Faults are denoted with black lines. Inverted triangles are injection wells and upright triangles are production wells. The power plant is denoted with a black square. Coordinates are easting and northing [km] in Universal Transverse Mercator (UTM) projection zone 11N, WGS84 (Snyder, 1987).

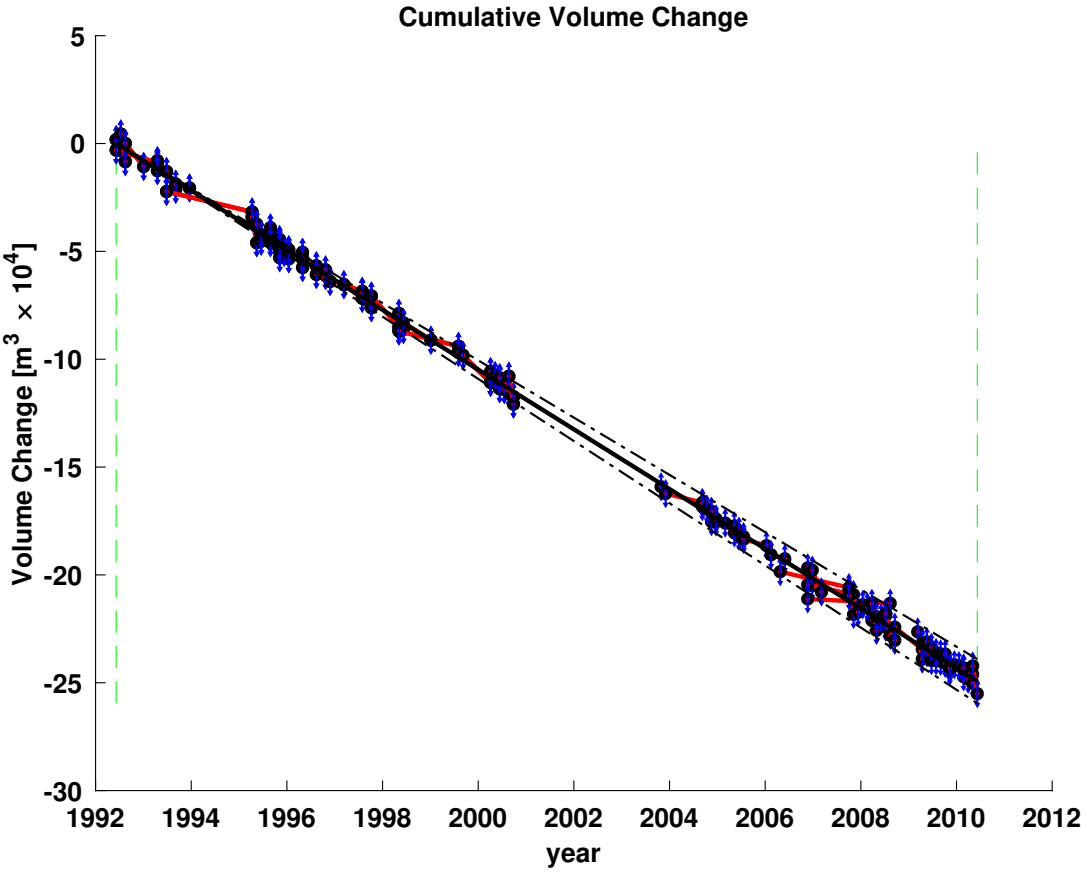

Figure 4.5: Time series at San Emidio, showing cumulative volume change from temporal adjustment of volume change rates estimated from InSAR data spanning 1992 to 2010. Black lines show the modeled volume change with 68% confidence intervals (dashed lines) as estimated by temporal adjustment with a single-rate temporal function (Reinisch et al., 2017). Red segments indicate measurements of observed volume change derived from individual interferometric pairs. For each pair, the volume change at the mid-point of each time interval is plotted to fall on the modeled curve and the vertical blue bars denote 1σ measurement uncertainty, after scaling by the square root of the variance scale factor (i.e., the dimensionless misfit χ).

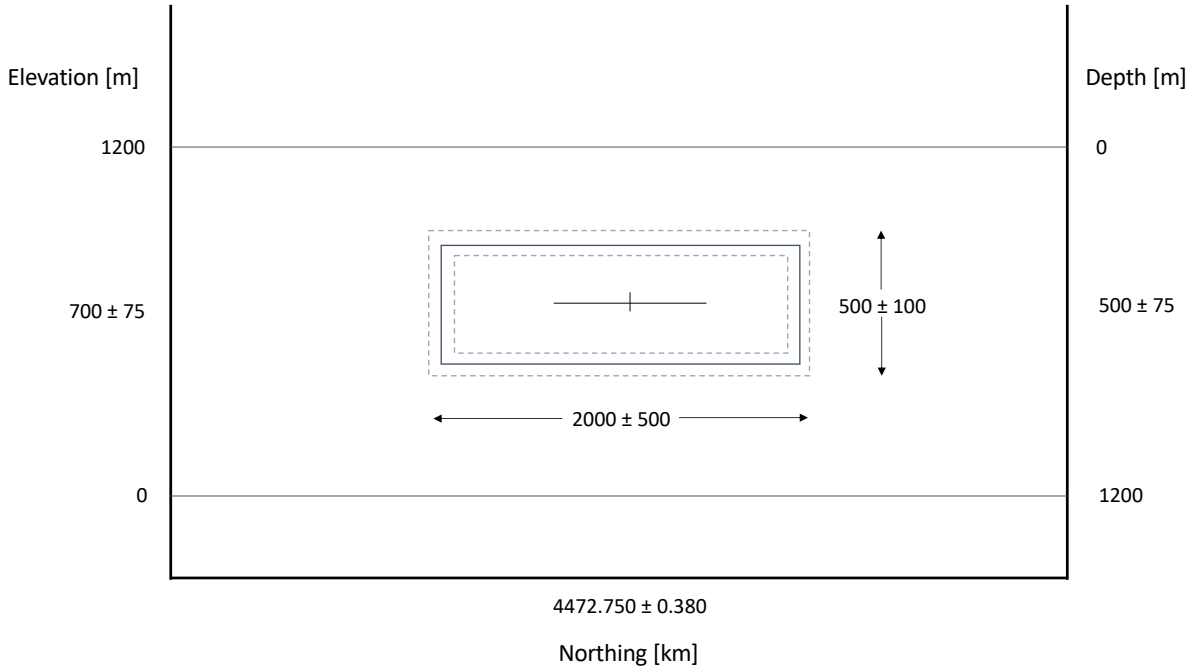

Figure 4.6: Schematic showing best-fitting cuboid model in cross-section (UTM northing vs. elevation/depth).

Conclusion

Throughout this dissertation, the application of analytical, numerical, and statistical techniques improves the characterization of InSAR-measured deformation both spatially and temporally at geothermal fields. For each of the three sites considered, deformation is described spatially by relating subsidence to subsurface reservoir volume change. At Brady Hot Springs, Nevada this relationship is described using a "multi-cube" parameterization. In contrast, a cuboidal reservoir model is used to characterize the deformation at Coso geothermal field, California and San Emidio geothermal field, Nevada.

At Brady and Coso, three hypotheses are tested to identify the most likely geophysical mechanism driving the observed subsidence at the sites: (1) thermal contraction of the rock matrix, (2) decreasing pore-fluid pressure, and (3) a linear combination of (1) and (2). At Brady, thermal contraction of the rock matrix is found to be the dominant mechanism driving the subsidence. This is validated when considering changes in deformation in response to changes in well operations at the site (Chapter 2). This is not the case at Coso, where decreasing pore-fluid pressure is identified as the most likely driving mechanism of subsidence.

All three sites show temporal relationships between pumping and deformation. The correlation between production and deformation is quantified at both Coso and San Emidio and found to be significant, suggesting that pumping affects the magnitude of subsidence at these sites.

At Coso, relationships between temporal trends in seismicity and pumping are also explored. Before sustainability efforts were implemented in 2010, seismicity rates at Coso were inversely related to production. This phenomena has been similarly observed at both Brady and San Emidio, where subsurface effective stress has adapted to long-term normal operations (Cardiff et al., 2017; Warren et al., 2018). However, after 2010, no there is no apparent relationship between seismicity rate and pumping at Coso. This finding, along with results from deformation modeling, suggest that the reservoir at Coso is getting deeper over time in response to the change in injection protocol in late 2009.

The results from modeling deformation at all three geothermal sites demonstrate that the capability of InSAR to detect deformation and its relationship to well operations is enhanced through improving spatio-temporal modeling techniques and emphasizes the benefits of using InSAR to monitor geothermal resources.

Bibliography

Agram, P. S. & Simons, M., 2015. A noise model for InSAR time series, *Journal of Geophysical Research: Solid Earth*.

Aki, K. & Richards, P. G., 1980. *Quantitative Seismology*, W. H. Freeman, New York.

Ali, S. & Feigl, K., 2012. A new strategy for estimating geophysical parameters from InSAR data: application to the Krafla central volcano in Iceland, *Geochemistry, Geophysics, Geosystems*, **13**(6).

Ali, S., Davatzes, N., Mellors, R., Foxall, W., Drakos, P., Zemach, E., Kreemer, C., Wang, H., & Feigl, K., 2014. InSAR measurements and numerical models of deformation at Brady Hot Springs geothermal field (Nevada), 1995-2012, in *Proceedings, Thirty-Ninth Workshop on Geothermal Reservoir Engineering*.

Ali, S., Akerley, J., Baluyut, E., Cardiff, M., Davatzes, N., Feigl, K., Foxall, W., Fratta, D., Mellors, R., Spielman, P., Wang, H., & Zemach, E., 2016a. Time-series analysis of surface deformation at Brady Hot Springs geothermal field (Nevada) using interferometric synthetic aperture radar, *Geothermics*, **61**, 114 – 120.

Ali, S. T., 2014. DEFMOD-Parallel multiphysics finite element code for modeling crustal deformation during the earthquake/rifting cycle, *arXiv preprint arXiv:1402.0429*.

Ali, S. T., Akerley, J., Baluyut, E. C., Davatzes, N. C., Lopeman, J., Moore, J., Plummer, M., Spielman, P., Warren, I., & Feigl, K. L., 2016b. Geodetic measurements and numerical models of deformation: Examples from geothermal fields in the western United States, in *Proceedings, Forty-First Workshop on Geothermal Reservoir Engineering*.

Aster, R. C., Borchers, B., & Thurber, C. H., 2013. *Parameter Estimation and Inverse Problems*, Academic Press, 360 pp., 2nd edn.

Austin, C. F. & Moore, J., 1987. Structural interpretation of the Coso geothermal field, Tech. rep., Naval Weapons Center, China Lake, CA.

Baran, I., Stewart, M. P., Kampes, B. M., Perski, Z., & Lilly, P., 2003. A modification to the Goldstein radar interferogram filter, *IEEE Transactions on Geoscience and Remote Sensing*,

41(9), 2114–2118.

Barbour, A. J., Evans, E. L., Hickman, S. H., & Eneva, M., 2016. Subsidence rates at the southern Salton Sea consistent with reservoir depletion, *Journal of Geophysical Research: Solid Earth*, **121**(7), 5308–5327.

Beauducel, F., 2014. Matlab/Octave tools for geophysical studies, http://www.ipgp.fr/∼beaudu/matlab.html.

Benoit, W. R., Hiner, J. E., & Forest, R. T., 1982. Discovery and geology of the Desert Peak geothermal field: a case history. Bulletin 97, Tech. rep., U. of Nevada Reno (USA).

Berardino, P., Fornaro, G., Lanari, R., & Sansosti, E., 2002. A new algorithm for surface deformation monitoring based on small baseline differential SAR interferograms, *Geoscience and Remote Sensing, IEEE Transactions on*, **40**(11), 2375–2383.

Bhattacharyya, J. & Lees, J. M., 2002. Seismicity and seismic stress in the Coso Range, Coso geothermal field, and Indian Wells Valley region, southeast-central California, *Mem. Geol. Soc. Am*, **195**, 243–257.

Blankenship, D., 2016. West Flank Coso, CA FORGE: Well 48-11TCH temperature, pressure, directional, well history, well bore schematic, Tech. rep., DOE Geothermal Data Repository; Sandia National Laboratories. https://dx.doi.org/10.15121/1261976.

Blewitt, G., 2018a. Nevada geodetic laboratory station ID: COSJ, Data set at: http://geodesy.unr.edu/NGLStationPages/stations/COSJ.sta.

Blewitt, G., 2018b. Nevada geodetic laboratory station ID: COSO, Data set at: http://geodesy.unr.edu/NGLStationPages/stations/COSO.sta.

Blewitt, G., Kreemer, C., Hammond, W. C., & Goldfarb, J. M., 2013. Terrestrial reference frame NA12 for crustal deformation studies in North America, *Journal of Geodynamics*, **72**, 11–24.

Blewitt, G., Hammond, W., & Kreemer, C., 2018. Harnessing the GPS data explosion for interdisciplinary science, *Eos*, **99**, https://doi.org/10.1029/2018EO104623.

BLM, 2014. California Trail Interpretive Center, https://www.californiatrailcenter.org.

Bonafede, M. & Ferrari, C., 2009. Analytical models of deformation and residual gravity changes due to a Mogi source in a viscoelastic medium, *Tectonophysics*, **471**(1), 4 – 13, Understanding stress and deformation in active volcanoes.

Brodsky, E. E. & Lajoie, L. J., 2013. Anthropogenic seismicity rates and operational parameters at the Salton Sea Geothermal Field, *Science*, **341**(6145), 543–546.

Cardiff, M., Lim, D. D., Akerley, J. R. P. J., Spielman, P., Lopeman, J., Walsh, P., Singh, A., Foxall, W., Wang, H. F., Lord, N. E., Thurber, C. H., Fratta, D., Mellors, R. J., Davatzes, N. C., & Feigl, K. L., 2017. Geothermal production and reduced seismicity: Correlation and proposed mechanism, *Earth and Planetary Science Letters*, **482**, 470–477.

Chen, C. W. & Zebker, H. A., 2000. Network approaches to two-dimensional phase unwrapping: intractability and two new algorithms, *JOSA A*, **17**(3), 401–414.

Coolbaugh, M. F., Sladek, C., Kratt, C., & Edmondo, G., 2004. Digital mapping of structurally controlled geothermal features with GPS units and pocket computers, *Geothermal Resources Council Transactions*, **28**, 321–325.

Cooper, H. & Simmons, G., 1977. The effect of cracks on the thermal expansion of rocks, *Earth and Planetary Science Letters*, **36**(3), 404 – 412.

Davatzes, N. C. & Hickman, S. H., 2010. The feedback between stress, faulting, and fluid flow: Lessons from the Coso Geothermal Field, CA, USA, in *Proceedings World Geothermal Congress 2010*, pp. 1–14.

Davatzes, N. C., Feigl, K. L., Mellors, R. J., Foxall, W., Wang, H. F., & Drakos, P., 2013. Preliminary investigation of reservoir dynamics monitored through combined surface deformation and micro-earthquake activity: Brady's geothermal field, Nevada, in *Proceedings of the Thirty-Eighth Workshop on Geothermal Reservoir Engineering, Stanford, California*, pp. 11–13.

Deng, K., Liu, Y., & Harrington, R. M., 2016. Poroelastic stress triggering of the December

2013 Crooked Lake, Alberta, induced seismicity sequence, *Geophysical Research Letters*, **43**(16), 8482–8491.

Division of Oil, Gas, and Geothermal Resources, 2016. Monthly records of production and injection for geothermal resources., ftp://ftp.consrv.ca.gov/pub/oil/geothermal/Coso.xls.

Ellsworth, W. L., 2013. Injection-induced earthquakes, *Science*, **341**(6142), 142.

Eneva, M., Falorni, G., Teplow, W., Morgan, J., Rhodes, G., & Adams, D., 2011. Surface deformation at the San Emidio geothermal field, Nevada, from satellite radar interferometry, *Geothermal Resources Council Transactions*, **35**, 1647–1653.

Eneva, M., Barbour, A., Adams, D., Hsiao, V., Blake, K., Falorni, G., & Locatelli, R., 2018. Satellite observations of surface deformation at the Coso geothermal field, California, in *GRC Transactions*, vol. 42, pp. 1383–1401.

Ettinger, T. & Brugman, J., 1992. Brady Hot Springs geothermal power plant, in *14th New Zealand geothermal workshop*.

Farr, T. G., Rosen, P. A., Caro, E., Crippen, R., Duren, R., Hensley, S., Kobrick, M., Paller, M., Rodriguez, E., Roth, L., Seal, D., Shaffer, S., Shimada, J., Umland, J., Werner, M., Oskin, M., Burbank, D., & Alsdorf, D., 2007. The shuttle radar topography mission, *Reviews of Geophysics*, **45**(2), RG2004.

Faulds, J., Moeck, I., Drakos, P., Zemach, E., et al., 2010a. Structural assessment and 3D geological modeling of the Brady's geothermal area, Churchill county (Nevada, USA): A preliminary report, in *35th Stanford Workshop on Geothermal Reservoir Engineering*.

Faulds, J. E., Garside, L. J., & Oppliger, G. L., 2003. Structural analysis of the Desert Peak-Brady geothermal field, Northwestern Nevada: implications for understanding linkages between Northeast-trending structures and geothermal reservoirs in the Humboldt structural zone, *Transactions-Geothermal Resources Council*, pp. 859–864.

Faulds, J. E., Coolbaugh, M. F., Benoit, D., Oppliger, G., Perkins, M., Moeck, I., & Drakos, P., 2010b. Structural controls of geothermal activity in the northern Hot Springs Mountains,

western Nevada: The tale of three geothermal systems (Brady's, Desert Peak, and Desert Queen), *Geothermal Resources Council Transactions*, **34**, 675–683.

Feighner, M. & Goldstein, N., 1990. A gravity model for the Coso geothermal area, California, in *Annual meeting of the Geothermal Resources Council and international symposium on geothermal energy*.

Feigl, K. L. & PoroTomo Team, 2017a. Overview and preliminary results from the porotomo project at Brady Hot Springs, Nevada: Poroelastic tomography by adjoint inverse modeling of data from seismology, geodesy, and hydrology, in *42nd Stanford Workshop on Geothermal Reservoir Engineering*.

Feigl, K. L. & PoroTomo Team, 2017b. Poroelastic tomography by adjoint inverse modeling of data from seismology, geodesy, and hydrology, in *Geothermal Technologies Office Peer Review 2017*.

Feigl, K. L. & Thurber, C. H., 2009. A method for modelling radar interferograms without phase unwrapping: application to the M 5 Fawnskin, California earthquake of 1992 December 4, *Geophysical Journal International*, **176**(2), 491–504.

Feigl, K. L., Reinisch, E. C., Ali, S. T., Thurber, C. H., Powell, L., Sobol, P., & Masters, A., 2019a. General inversion of phase technique (gipht) software repository, Tech. rep., GitHub.

Feigl, K. L., Reinisch, E. C., & Team, P., 2019b. PoroTomo software repository, Tech. rep., GitHub.

Ferretti, A., Fumagalli, A., Novali, F., Prati, C., Rocca, F., & Rucci, A., 2011. A New Algorithm for Processing Interferometric Data-Stacks: SqueeSAR, *Geoscience and Remote Sensing, IEEE Transactions on*, **49**(9), 3460–3470.

Fialko, Y. & Simons, M., 2000. Deformation and seismicity in the Coso geothermal area, Inyo County, California: Observations and modeling using satellite radar interferometry, *Journal of Geophysical Research: Solid Earth*, **105**(B9), 21781–21793.

Fletcher, K., 2013. *ERS Missions: 20 Years of Observing Earth (ESA SP-1326)*, ESA (Euro-

pean Space Agency).

Fournier, R., Thompson, J., & Austin, C., 1980. Interpretation of chemical analyses of waters collected from two geothermal wells at Coso, California, *Journal of Geophysical Research: Solid Earth*, **85**(B5), 2405–2410.

Foxall, W., 2014. Brady's Geothermal Field Seismic Network Metadata [data set], Tech. rep., DOE Geothermal Data Repository; The University of Wisconsin, https://dx.doi.org/10.15121/1166944.

Foxall, W., 2016. PoroTomo Subtask 3.1 Meq Relocations & 3D Velocity Models 30 June 2015 [data set], Tech. rep., DOE Geothermal Data Repository; The University of Wisconsin, https://doi.org/10.15121/1196282.

Francis, C., Graf, G., Edwards, P., McCraig, M., McCarthy, C., Lefebvre, A., Pieper, B., Pouvreau, P.-Y., Wall, R., & Weschler, F., 1995. The ERS-2 spacecraft and its payload, *ESA Bulletin*, **83**.

Gelman, A., Carlin, J., Stern, H., Dunson, D., Vehtari, A., & Rubin, D., 2013. *Bayesian Data Analysis, Third Edition*, Chapman & Hall/CRC Texts in Statistical Science, Taylor & Francis.

Geudtner, D., Torres, R., Snoeij, P., Davidson, M., & Rommen, B., 2014. Sentinel-1 system capabilities and applications, in *2014 IEEE Geoscience and Remote Sensing Symposium*, pp. 1457–1460, IEEE.

Goldstein, R. & Werner, C., 1997. Radar ice motion interferometry, in *3rd ERS Symposium on Space at the Service of Our Environment*, vol. 2, pp. 969–972.

Herring, T. A., Melbourne, T. I., Murray, M. H., Floyd, M. A., Szeliga, W. M., King, R. W., Phillips, D. A., Puskas, C. M., Santillan, M., & Wang, L., 2016. Plate Boundary Observatory and related networks: GPS data analysis methods and geodetic products, *Reviews of Geophysics*, **54**(4), 759–808.

Hohn, M., 1998. *Geostatistics and Petroleum Geology*, Computer Methods in the Geosciences,

Springer Netherlands.

Holzner, J., 2003. Performance of ENVISAT/ASAR Interferometric Products, in *ESA Special Publication*, vol. 531.

Hudnut, K., King, N., Aspiotes, A. G., Borsa, A. A., Determan, D. N., Galetzka, J. E., & Stark, K. F., 2006. SCIGN USGS GPS Network: COSO-China Lake P.S., *UNAVCO, GPS Data Set. https://doi.org/10.7283/T5V40SGR*.

Ingraham, M. D., Bauer, S. J., Issen, K. A., & Dewers, T. A., 2017. Evolution of permeability and Biot coefficient at high mean stresses in high porosity sandstone, *International Journal of Rock Mechanics and Mining Sciences*, **96**, 1 – 10.

Jennings, C., Saucedo, G., Dart, R., Machette, M., Burns, D., Faneros, G., Little, J., & Davis, J., 2000. Digital database of faults from the fault activity map of California and adjacent areas, *Calif. Div. Mines Geol., DMG CD*, **6**, 2000. https://searchworks.stanford.edu/view/4463334.

Jennings, P., 1975. Fault map of California with volcanoes, thermal springs and thermal wells at 1: 750,000 scale, *Geological Data Map*, **1**, https://searchworks.stanford.edu/view/510979.

Jolie, E., Moeck, I., & Faulds, J. E., 2015. Quantitative structural–geological exploration of fault-controlled geothermal systems—A case study from the Basin-and-Range Province, Nevada (USA), *Geothermics*, **54**, 54–67.

Kass, R. E. & Raftery, A. E., 1995. Bayes Factors, *Journal of the American Statistical Association*, **90**(430), 773–795.

Kaven, J. O., Hickman, S. H., & Davatzes, N. C., 2011. Micro-seismicity, fault structure and hydraulic compartmentalization within the Coso gethermal field, California, in *Proceedings, Thirty-Sixth Workshop on Geothermal Reservoir Engineering*.

Kaven, J. O., Hickman, S. H., & Davatzes, N. C., 2012. Using micro-seismicity and seismic velocities to map subsurface geologic and hydrologic structure within the Coso geothermal field, California, in *Proceedings, Thirty-Seventh Workshop on Geothermal Reservoir Engineering*.

Kaven, J. O., Hickman, S. H., & Davatzes, N. C., 2013. Micro-seismicity within the Coso geothermal field, California, from 1996-2012, in *Proceedings, Thirty-Eighth Workshop on Geothermal Reservoir Engineering*.

Kitanidis, P. K., 2007. On stochastic inverse modeling, *Subsurface Hydrology: Data Integration for Properties and Processes*, pp. 19–30.

Kreemer, C., 2018. BRAD BRDY and BRD1 GPS Station RINEX Files 01-19-2018 [data set], Tech. rep., DOE Geothermal Data Repository; University of Wisconsin, https://gdr.openei.org/submissions/999.

Krieger, G., Moreira, A., Fiedler, H., Hajnsek, I., Werner, M., Younis, M., & Zink, M., 2007. TanDEM-X: A satellite formation for high-resolution SAR interferometry, *IEEE Transactions on Geoscience and Remote Sensing*, **45**(11), 3317–3341.

Laboso, R. C. & Davatzes, N., 2016. Fault-controlled damage and permeability at the Brady geothermal system, Nevada, USA, in *41st Workshop on Geothermal Reservoir Engineering, Stanford University*.

Lindseth, R. O., 1979. Synthetic sonic logs—A process for stratigraphic interpretation, *Geophysics*, **44**(1), 3–26.

Majer, E. L., Baria, R., Stark, M., Oates, S., Bommer, J., Smith, B., & Asanuma, H., 2007. Induced seismicity associated with enhanced geothermal systems, *Geothermics*, **36**(3), 185–222.

Malvern, L. E., 1969. *Introduction to the Mechanics of a Continuous Medium*, no. Monograph, Prentice-Hall, Inc.

Massonnet, D. & Feigl, K. L., 1998. Radar interferometry and its application to changes in the Earth's surface, *Reviews of Geophysics*, **36**(4), 441–500.

Matlick, S., 1995. San Emidio geothermal system, in *GRC field trip*, Mesquite Group, Inc.

Matzel, E., Zeng, X., Thurber, C., Luo, Y., Morency, C., & team, P., 2017. Seismic interferometry using the dense array at the Brady geothermal field, in *42nd Stanford Workshop on*

Geothermal Reservoir Engineering, p. 4, Stanford University Stanford, CA.

McLeod, I. H., Cumming, I. G., & Seymour, M. S., 1998. ENVISAT ASAR data reduction: Impact on SAR interferometry, *IEEE Transactions on Geoscience and Remote Sensing*, **36**(2), 589–602.

Meng, C., 2017. Benchmarking DEFMOD, an open source FEM code for modeling episodic fault rupture, *Computers & Geosciences*, **100**, 10–26.

Mindlin, R. D. & Cheng, D. H., 1950. Thermoelastic stress in the semi-infinite solid, *Journal of Applied Physics*, **21**(9), 931–933.

Minster, J. & Jordan, T., 1987. Vector constraints on western U. S. deformation from space geodesy, neotectonics and plate motions, *Journal of Geophysical Research*, **92**, 4798–4804.

Mogi, K., 1958. Relations between the eruptions of various volcanoes and the deformations of the ground surfaces around them, *Bulletin of the Earthquake Research Institute*, **36**, 99–134.

Monastero, F., Katzenstein, A., Miller, J., Unruh, J., Adams, M., & Richards-Dinger, K., 2005. The Coso geothermal field: A nascent metamorphic core complex, *Geological Society of America Bulletin*, **117**(11-12), 1534–1553.

Moreira, A., Prats-Iraola, P., Younis, M., Krieger, G., Hajnsek, I., & Papathanassiou, K. P., 2013. A tutorial on synthetic aperture radar, *IEEE Geoscience and remote sensing magazine*, **1**(1), 6–43.

Mossop, A. & Segall, P., 1997. Subsidence at The Geysers geothermal field, N. California from a comparison of GPS and leveling surveys, *Geophysical Research Letters*, **24**(14), 1839–1842.

Mossop, A. & Segall, P., 1999. Volume strain within The Geysers geothermal field, *Journal of Geophysical Research: Solid Earth*, **104**(B12), 29113–29131.

Nathwani, J., Majer, E., Boyle, K., Rock, D., Peterson, J., & Jarpe, S., 2011. DOE real-time seismic monitoring at enhanced geothermal system sites, in *Thirty-sixth workshop on Geothermal Reservoir Engineering*.

Nur, A. & Byerlee, J. D., 1971. An exact effective stress law for elastic deformation of rock with fluids, *Journal of Geophysical Research*, **76**(26), 6414–6419.

Nygren, A. J., 2005. *Geomechanics Applied to Reservoir Development in the Coso Geothermal Field*, Ph.D. thesis, University of North Dakota.

Okada, Y., 1985. Surface deformation due to shear and tensile faults in a half-space, *Bulletin of the Seismological Society of America*, **75**(4), 1135–1154.

Okada, Y., 1992. Internal deformation due to shear and tensile faults in a half-space, *Bulletin of the Seismological Society of America*, **82**(2), 1018–1040.

OpenEI, 2015. Coso Geothermal Area, https://openei.org/wiki/Coso_Geothermal_Area.

Ormat Techmologies Inc., 2017. Bhs-g08-pt-dpdt, Dataset.

Patterson, J. R., 2018. *Understanding Constraints on Geothermal Sustainability Through Reservoir Characterization at Brady Geothermal Field, Nevada*, Master's thesis, University of Wisconsin - Madison, https://gdr.openei.org/submissions/1077.

Patterson, J. R., Cardiff, M., Coleman, T., Wang, H., Feigl, K. L., Akerley, J., & Spielman, P., 2017. Geothermal reservoir characterization using distributed temperature sensing at Brady Geothermal Field, Nevada, *The Leading Edge*, **36**(12), 1024a1–1024a7.

Perissin, D. & Wang, T., 2012. Repeat-pass SAR interferometry with partially coherent targets, *Geoscience and Remote Sensing, IEEE Transactions on*, **50**(1), 271–280.

Pérouse, E. & Wernicke, B. P., 2017. Spatiotemporal evolution of fault slip rates in deforming continents: The case of the Great Basin region, northern Basin and Range province, *Geosphere*, **13**(1), 112.

Pitz, W. & Miller, D., 2010. The TerraSAR-X satellite, *IEEE Transactions on Geoscience and Remote Sensing*, **48**(2), 615–622.

Refice, A., Bovenga, F., & Nutricato, R., 2006. Mst-based stepwise connection strategies for multipass radar data, with application to coregistration and equalization, *Geoscience and Remote Sensing, IEEE Transactions on*, **44**(8), 2029–2040.

Reinisch, E., Ali, S., Cardiff, M., Morency, C., Kreemer, C., Feigl, K., & Team, P., 2016. Analysis of Interferometric Synthetic Aperture Radar Phase Data at Brady Hot Springs, Nevada, USA Using Prior Information, in *AGU Fall Meeting Abstracts*.

Reinisch, E. C., 2017. PoroTomo: Brady Geothermal Field InSAR Data [data set], Tech. rep., DOE Geothermal Data Repository; University of Wisconsin, http://gdr.openei.org/submissions/941.

Reinisch, E. C., to be submitted upon acceptance of manuscript. Brady Geothermal Field InSAR and GPS Time-Series Data Products [data set], Tech. rep., DOE Geothermal Data Repository; University of Wisconsin, ftp://roftp.ssec.wisc.edu/porotomo/PoroTomo/DATA/InSARforGDR.

Reinisch, E. C. & Feigl, K. L., 2018. TerraSAR-X Track 53 pair spanning 2017-06-22 to 2018-08-22, ftp://roftp.ssec.wisc.edu/porotomo/PoroTomo/DATA/InSAR/TSX/T53/In20160722_20170822.tgz.

Reinisch, E. C., Cardiff, M., & Feigl, K. L., 2017. Graph theory for analyzing pair-wise data: application to geophysical model parameters estimated from interferometric synthetic aperture radar data at Okmok volcano, Alaska, *Journal of Geodesy*, **91**(1), 9–24. https://doi.org/10.1007/s00190--016--0934--5.

Reinisch, E. C., Cardiff, M., & Feigl, K. L., 2018. Characterizing volumetric strain at Brady Hot Springs, Nevada, USA using geodetic data, numerical models, and prior information, *Geophysical Journal International*, **215**(2), 1501–1513.

Rhodes, G. T., 2011. *Structural Controls of the San Emidio Geothermal System, Northwestern Nevada*, University of Nevada, Reno.

Rodriguez, E. & Martin, J., 1992. Theory and design of interferometric synthetic aperture radars, in *IEE Proceedings F (Radar and Signal Processing)*, vol. 139, pp. 147–159, IET.

Rose, P. E., 2013. Creation of an enhanced geothermal system through hydraulic and thermal stimulation, Tech. rep., Energy and Geoscience Institute at the University of Utah.

Rosenqvist, A., Shimada, M., Ito, N., & Watanabe, M., 2007. ALOS PALSAR: A pathfinder mission for global-scale monitoring of the environment, *IEEE Transactions on Geoscience and Remote Sensing*, **45**(11), 3307–3316.

Roy, R., Agrawal, D. K., & McKinstry, H. A., 1989. Very Low Thermal Expansion Coefficient Materials, *Annual Review of Materials Science*, **19**(1), 59–81.

Rutqvist, J., Wu, Y.-S., Tsang, C.-F., & Bodvarsson, G., 2002. A modeling approach for analysis of coupled multiphase fluid flow, heat transfer, and deformation in fractured porous rock, *International Journal of Rock Mechanics and Mining Sciences*, **39**(4), 429 – 442.

Rutqvist, J., Dobson, P. F., Garcia, J., Hartline, C., Jeanne, P., Oldenburg, C. M., Vasco, D. W., & Walters, M., 2015. The northwest Geysers EGS demonstration project, California: Pre-stimulation modeling and interpretation of the stimulation, *Mathematical Geosciences*, **47**(1), 3–29.

Sandwell, D., Mellors, R., Tong, X., Wei, M., & Wessel, P., 2011a. Open radar interferometry software for mapping surface deformation, *Eos, Transactions American Geophysical Union*, **92**(28), 234–234. http://dx.doi.org/10.1029/2011EO280002.

Sandwell, D., Mellors, R., Tong, X., Wei, M., & Wessel, P., 2011b. GMTSAR: An InSAR processing system based on Generic Mapping Tools, *UC San Diego: Scripps Institution of Oceanography. http://escholarship.org/uc/item/8zq2c02m*.

Sandwell, D. T. & Price, E. J., 1998. Phase gradient approach to stacking interferograms, *Journal of Geophysical Research: Solid Earth*, **103**(B12), 30183–30204.

Schoenball, M., Glen, J. M., & Davatzes, N. C., 2016. Analysis and interpretation of stress indicators in deviated wells of the Coso geothermal field, in *Proceedings, Forty-First Workshop on Geothermal Reservoir Engineering*, pp. 1169–1180.

Segall, P., 1985. Stress and subsidence resulting from subsurface fluid withdrawal in the epicentral region of the 1983 Coalinga earthquake, *Journal of Geophysical Research: Solid Earth*, **90**(B8), 6801–6816.

Segall, P., 2010. *Earthquake and Volcano Deformation*, Princeton University Press.

Segall, P. & Fitzgerald, S. D., 1998. A note on induced stress changes in hydrocarbon and geothermal reservoirs, *Tectonophysics*, **289**(1-3), 117–128.

Siler, D. L., Hinz, N. H., Faulds, J. E., & Queen, J., 2016. 3D analysis of geothermal fluid flow favorability; Bradys, Nevada, USA, in *Proceedings, forty-first workshop on geothermal reservoir engineering. Stanford: Stanford University*.

Snyder, J. P., 1987. *Map projections–A working manual*, vol. 1395, US Government Printing Office.

Spane Jr, F. A., 1978. Hydrogeologic investigation of Coso Hot Springs, Inyo County, California., Tech. rep., Hydro-Search Inc, Reno, NV.

Stall, S., e. a., 2018. Advancing FAIR Data in Earth, Space, and Environmental Science, *Eos*, **99**.

Stall, S., Robinson, E., Wyborn, L., Yarmey, L., Parsons, M., Lehnert, K., Cutcher-Gershenfeld, J., Nosek, B., & Hanson, B., 2017. Enabling FAIR data across the Earth and space sciences, *Eos*, **98**.

Stein, S. & Wysession, M., 2003. *An Introduction to Seismology, Earthquakes, and Earth Structure*, Blackwell Publishing.

Strang, G. & Borre, K., 1997. *Linear Algebra, Geodesy, and GPS*, SIAM, 624 pp.

TEAM Engineering & Management, Inc., 2018. Hay ranch project conditional use permit hydrologic monitoring report: fourth quarter 2017 inyo county, california., Tech. rep., TEAM. http://www.inyowater.org/wp-content/uploads/legacy/INDEX_DOCS/Coso%20Hay%20Ranch_FEIR_Dec_30_08.pdf.

Temple University, 2017. Pressure-Temperature Simulation at Brady Hot Springs [data set], https://gdr.openei.org/submissions/939. https://dx.doi.org/10.15121/1369075.

University of Wisconsin, 2016. Brady Geothermal Field Well Pumping Data During Deployment [data set], Retrieved from https://gdr.openei.org/submissions/845.

https://dx.doi.org/10.15121/1334283.

Unruh, J. R., Hauksson, E., Monastero, F. C., Twiss, R. J., & Lewis, J. C., 2002. Seismotectonics of the Coso Range–Indian Wells Valley region, California: Transtensional deformation along the southeastern margin of the Sierran microplate, *Geologic evolution of the Mojave Desert and southwestern Basin and Range: Geological Society of America Memoir*, **195**, 277–294.

Wackerly, D., Mendenhall, W., & Scheaffer, R., 2007. *Mathematical Statistics with Applications*, Cengage Learning, 944 pp.

Wang, H., 2000. *Theory of Linear Poroelasticity with Applications to Geomechanics and Hydrogeology*, Princeton series in geophysics, Princeton University Press.

Warren, I., Gasperikova, E., Pullammanappallil, S., & Grealy, M., 2018. Mapping geothermal permeability using passive seismic emission tomography constrained by cooperative inversion of active seismic and electromagnetic data, in *43rd Stanford Workshop on Geothermal Reservoir Engineering*.

Wessel, P., Smith, W. H., Scharroo, R., Luis, J., & Wobbe, F., 2013. Generic Mapping Tools: improved version released, *Eos, Transactions American Geophysical Union*, **94**(45), 409–410.

Witter, J. B., Siler, D. L., Faulds, J. E., & Hinz, N. H., 2016. 3D geophysical inversion modeling of gravity data to test the 3D geologic model of the Bradys geothermal area, Nevada, USA, *Geothermal Energy*, **4**(1), 14.

Zebker, H. A. & Goldstein, R. M., 1986. Topographic mapping from interferometric synthetic aperture radar observations, *Journal of Geophysical Research: Solid Earth*, **91**(B5), 4993–4999.

Zencher, F., Bonafede, M., & Stefansson, R., 2006. Near-lithostatic pore pressure at seismogenic depths: a thermoporoelastic model, *Geophysical Journal International*, **166**(3), 1318–1334.

Zheng, Y., Burridge, R., & Burns, D. R., 2003. Reservoir simulation with the finite element method using Biot poroelastic approach, Tech. rep., Massachusetts Institute of Technology. Earth Resources Laboratory.